ABSTRACT

YANG, ZHENYIN. Contact Material Optimization and Contact Physics in Metal-contact Microelectromechanical Systems (MEMS) Switches. (Under the direction of Dr. Angus I. Kingon).

Metal-contact MEMS switches hold great promise for implementing agile radio frequency (RF) systems because of their small size, low fabrication cost, low power consumption, wide operational band, excellent isolation and exceptionally low signal insertion loss. Gold is often utilized as a contact material for metal-contact MEMS switches due to its excellent electrical conductivity and corrosion resistance. However contact wear and stiction are the two major failure modes for these switches due to its material softness and high surface adhesion energy. To strengthen the contact material, pure gold was alloyed with other metal elements. We designed and constructed a new micro-contacting test facility that closely mimic the typical MEMS operation and utilized this facility to efficiently evaluate optimized contact materials. Au-Ni binary alloy system as the candidate contact material for MEMS switches was systematically investigated. A correlation between contact material properties (etc. microstructure, micro-hardness, electrical resistivity, topology, surface structures and composition) and micro-contacting performance was established. It was demonstrated nano-scale graded two-phase Au-Ni film could possibly yield an improved device performance.

Gold micro-contact degradation mechanisms were also systematically investigated by running the MEMS switching tests under a wide range of test conditions. According to our quantitative failure analysis, field evaporation could be the dominant failure mode for high-field (> critical threshold field) hot switching; transient thermal-assisted wear could be the dominant failure mode for low-field hot switching; on the other hand, pure mechanical wear

and steady current heating (1 mA) caused much less contact degradation in cold switching tests. Results from low-force (50 μN/ micro-contact), low current (0.1 mA) tests on real MEMS switches indicated that continuous adsorbed films from ambient air could degrade the switch contact resistance.

Our work also contributes to the field of general nano-science and technology by resolving the transfer directionality of field evaporation of gold in atomic force microscope (AFM) /scanning tunneling microscope (STM).

Contact Material Optimization and Contact Physics in Metal-contact Microelectromechanical Systems (MEMS) Switches

by
Zhenyin Yang

A dissertation submitted to the Graduate Faculty of
North Carolina State University
In partial fulfillment of the
Requirements for the degree of
Doctor of Philosophy

Material Science and Engineering

Raleigh, North Carolina

2008

APPROVED BY:

Dr. Angus I. Kingon Committee Chair	Dr. Ron O. Scattergood
Dr. Jackie Krim	Dr. Donald W. Brenner

BIOGRAPHY

Zhenyin Yang received the B. S. degree from Nanjing University, Nanjing, China in 2001, and the M. S. degree in applied science from the College of William & Mary, Williamsburg, VA in 2004. He joined the Department of Material Science & Engineering at North Carolina State University in 2004. His research interests lie in thin film processing, vacuum technology, micro-fabrication and micro-engineering. His work focuses on developing new contact materials and investigating switch failure mechanisms for metal-contact RF MEMS switches. He was awarded with Texas Instrument Fellowship in 2007 and membership from Alpha Sigma Mu (ΑΣΜ), the international Materials Science and Engineering honorary society in 2008.

ACKNOWLEDGMENTS

I gratefully acknowledge Dr. Angus I. Kingon for giving me the opportunity to pursue my Ph.D. under his guidance. I sincerely appreciate his time and support for my research on material issues in MEMS switches, as well as his help in improving this dissertation.

I would like to thank Dr. Ron O. Scattergood, Dr. Jackie Krim and Dr. Donald W. Brenner for being on my committee and giving me their valuable advice in my research.

I am very grateful to Dr. Daniel J. Lichtenwalner for constantly providing me with technical support, in-depth scientific advice and continuous encouragement, to all of the other members in the lab for their helps. I owed my thanks to Dr. Omid Rezvanian and Dr. Douglas Irving for their valuable feedback on my research, to Dong Wu for his assistance on AFM facilities, to Chris Brown for his device-side contribution to my research.

Finally, I would like to thank my family for their unconditional support, and I would especially like to thank my wife- Jia for her love and support.

TABLE OF CONTENTS

LIST OF TABLES

LIST OF FIGURES

CHAPTER 1 Introduction

1.1 Applications of Microelectromechanical (MEMS) Switches

Since the first MEMS switch was specially designed for microwave applications in the early 90s [1], this technology has developed to the point that the devices are currently in small-scale production. Typical MEMS switches are micron-scale switching devices. Because of their low fabrication cost, low power consumption, wide operational band and exceptional switching performance, MEMS switching technology holds great promise for implementing agile radio frequency (RF) systems [2-10].

RF MEMS switches are currently being shipped or are in development for a very wide spectrum of applications, from high-value niches such as satellites to mobile phones. Four major application fields have been identified: test equipment, telecom infrastructures, aerospace and defense and mobile phones. A projection for the growth of RF MEMS switch market is shown in Figure 1 [11]. As can be seen in the figure, automated test equipment (ATE) is the first, also the largest commercial application for RF switches. MEMS switches can replace conventional relays with changing the system configurations. Major ATE system suppliers such as Agilent are currently evaluating or have started implementation of MEMS in their systems.

With respected to the telecom infrastructure application, MEMS switches are projected to be implemented in wire-line telecom switching matrices early in 2008. The potential applications for defense have historically driven the development of MEMS switches in US. The volume application will be phased arrays antennas for communication and radars e.g. for missiles, helicopters, aircrafts, drones, ships and so forth. Power amplifier (PA) and antenna module are believed to be the two fields that MEMS switches (particularly capacitive-type switches) might beat CMOS switches for mobile phone applications in the future.

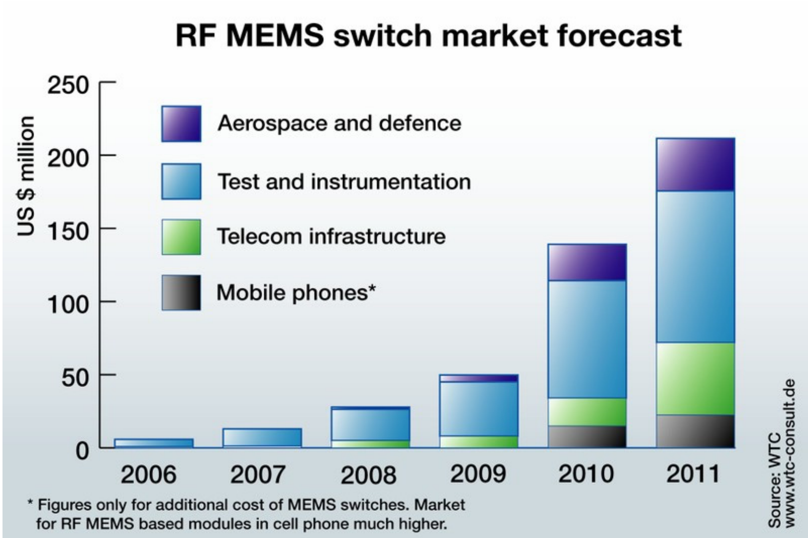

FIG. 1: RF MEMS switch market forecast [11]

1.2 Issues with Metal Contact MEMS Switches

This thesis focuses on the issues that related to the degradation of metal contacts during switch cycling operation since switch performance is directly tied to the reliability and quality of the metal-contacts. Gold is often utilized as a contact material for metal-contact MEMS switches due to its excellent electrical conductivity and corrosion resistance. Gold-contact switches have been shown to achieve $>10^9$ cycles under appropriate operating conditions (etc. low current, optimum contact force, dry nitrogen environment and 'cold switching') [7, 12]. 'Cold switching' refers to switch operation under conditions in which there is no field across the contacts as the switch opens or closes). However, there is a strong desire to significantly broaden the range of conditions under which a given switch would operate. For example, Manufacturers of RF instrumentation equipment, i.e. network analyzers, spectrum analyzers and oscilloscopes like Agilent, Rhode & Schwarz and Tektronix are evaluating MEMS switches and would implement them in their RF equipments. However, power handling issues must be solved prior to implementation in RF instruments since hot switching is required, contrary to ATE. Here, 'hot switching' is defined as switch cycling with a signal or potential difference across the electric contacts.

One approach to the problem is to investigate alternative contact materials, and a few have been investigated [13-14]. However, there are some serious impediments to the broad investigation of alternative contact materials. In general, convenient contact wear test facilities do not closely mimic real contact switches. In particular, the tests have difficulty duplicating the switch geometry, the contact geometry, and the contact force. Contact geometry has a strong influence on the heat distribution across the contacts, and thus the switch performance and failure mechanism [15-16].

One clear alternative is to test candidate materials on actual MEMS switches, and such studies have been reported by researchers from universities and industry [7,17, 18, 19]. But the approach has a serious difficulty: the switches are fabricated in Si foundries, and only a limited range of materials may enter the fabrication facility. Secondly, the fabrication process must be optimized for each material, and it may take many months to fabricate a set of switches to test a single candidate contact material. Materials compatibility and process integration issues must be addressed in advance for every material to be tested. These factors have severely limited the range of contact materials that have been investigated for MEMS switches. If progress is to occur, the testing and development of alternative contact materials must be more efficient while remaining representative of the typical device operation. In this manner the material comparison and failure analysis data can be collected consistently and efficiently.

Researchers have been investigating the degradation mechanisms of metal micro-contacts in MEMS switches (reviewed in Chapter 2). However these highly-scattered failure characterization results are contingent on different devices and test conditions therefore, are not yet able to provide a systematic and quantitative overview of different degradation modes in MEMS switches. A comprehensive understanding of the switch failure mechanisms has not been achieved due to the absence of a systematic study of micro-contact degradation modes and quantitative failure characterization, For example, failure analysis for hot switching failure is particularly difficult because the degradation process can be complicated by several possible modes such as arcing, transient current heating, static current heating and mechanical wear. Additionally, dramatic failure observed under a non-arc condition has not been clearly understood [20]. Research on contact degradation for MEMS switches has been driven by the urge of developing high-reliable MEMS switches.

1.3 Brief Summary of Our Work

In our study, we designed the micro-contacting test facility that closely mimics the typical MEMS operation and utilize this facility to efficiently evaluate different candidate contact materials for MEMS switches. Using this facility, a binary gold alloy system- AuNi was systematically studied (etc. chemical composition, micro-structure, surface conditions) for the MEMS contact material application. Micro-contact degradation under a set of different test conditions (etc. high-voltage hot-switching, low voltage hot-switching, DC switching, AC switching, mediate-force cold switching, low-force cold switching) has been also systematically studied. Through our work, a better correlation between material properties and micro-contacting performance is established and an improved understanding of micro-contact degradation is achieved.

This document is comprised of eight chapters. Chapter one briefly introduces the topic of RF MEMS metal contact switches and the focus of this thesis. Chapter two is a comprehensive review of metal contact micro-switches and the related material topics. Nano- and atomic scale material transfer theories are also reviewed because our work also directly contributes to this general nano-science field. Chapter three summaries the approaches we used to fabricate, characterize and test our candidate contact materials. The design and construction of our unique test facility is described in details. Chapter four, five present our work on gold and Au-Ni alloy system in format of research papers. Chapter six addresses micro-contact degradation in MEMS switches under non-arc hot-switching conditions. Chapter seven focuses on resolving the directionality of field evaporation for gold. Chapter eight presents our work of cold switching tests. An overview of failure mechanisms is also given in this chapter.

1.4 References

[1] L. E. Larson *et al*, "Micromachined microwave actuator (MIMAC) technology-a new tuning

approach for microwave integrated circuits," *Microwave and Millimeter-Wave Monolithic Circuits Symposium Digest*. (*Boston, MA*) pp 27-30

[2] C. Bowick, *RF Circuit Design.* USA: Newnes – Elsevier Science, 1982

[3] D. L. Santos and J. Hector, "Microwave and mechanical considerations in the design of MEM switches for aerospace applications, 1997

[4] E. R. Brown, "RF MEMS switches for reconfigurable integrated circuits," *IEEE Trans. on MTT,* 46 (11): 1868-1880, (November 1998)

[5] J. Chial. "MEMS for high-frequency applications," *Proc. 8th Annual Int. Symp. on Smart Mat.,* 1-10 (March 2001)

[6] H. S. Newman. "RF MEMS switches and applications," *Proc. 40th Annual Int. Rel. Phy. Symp.,* 111-115 (April 2002)

[7] G. M. Rebeiz, *RF MEMS theory, design and technology,* New Jersey: John Wiley & Sons, Inc., 2003

[8] G. M. Rebeiz and J. B. Muldavin, "RF MEMS switches and switch circuits," *IEEE Microwaves Magazine,* 59-71 (December 2001)

[9] J. H. Schaffner, A. E. Schmitz, T. Hsu, D. T. Chang, R. Y. Loo and D. F. Sievenpiper, "Metal contact RF MEMS switch elements for ultra wideband RF front-end systems," *Proc. Ultra Wideband Sys. Tech.,* 32-36 (November 2003)

[10] V. K. Varadan, K. J. Vinoy and K. A. Jose, *RF MEMS and their applications,* Egland: John Wiley & Sons, Ltd., 2003

[11] J. Bouchaud and B. Knoblich, "RF MEMS switches deliver on early promise," MEMS Investor Journal, Source: WTC, www.wtc-consult.de (October, 2007)

[12] A. S. Morris, S. Cunningham, D. Dereus and G. Schopfer, “High-performance integrated RF-MEMS: Part 1 – the process,” *Proceedings of 33rd European Microwave Conference*, 2003, pp. 21-24

[13] J. Schimkat, “ Contact materials for microrelays,” in *11th Proc. MEMS’ 98 Workshop,* 1998, pp. 190-194

[14] R. A. Coutu, Ph.D. Dissertation: *Electrostatic Radio Frequency (RF) MicroElectroMechnical Systems (MEMS) Switches with Metal Alloy Electric Contacts* Air Force Institute of Technology. 2004.

[15] L. Chen, “Contact evolution in micromechanical switches,” in *World Tribology Congress,* Washington D. C., U.S.A. 2005

[16] D. Hyman and M. Mehregany, “ Contact physics of gold microcontacts for MEMS switches,” *IEEE Trans. Comp. Packag. Tech.,* vol. 22, pp. 357-364, 1999

[17] K. Hiltmann, A. Schumacher, K. Guttmann, E. Lemp, H. Sandmaier, W. Lang, “New micro-machined membrane switches in silicon technology,” *47th IEEE Holm Conference on Electrical Contacts* pp. 190-194, 2001

[18] K. Hiltmann, W. Keller and W. Lang, ”Micromachined switches for low electric loads,” *Sensors and Actuators A* **74** 203-206, 1999

[19] S. Majumder *et al*, “MEMS switches,” *IEEE Intrumentation & Measurement Magazine* **6**(1) 12, 2003

[20] E. J. J. Kruglick and K. S. J. Pister, “Lateral MEMS microcontact consideration,”, *J. Microelectromechanical Syst.* vol. 8, pp. 264-271, 1999

CHAPTER 2 LITERATURE REVIEW

2.1 Desires for MEMS Switch Technology

In modern microelectronics, to switch between the electrical 'on' and 'off' states, solid state devices (etc. transistors and diodes) utilize voltage potential to modulate the carrier concentration in semiconductors. Conductivity modulation through the same channel (normally crystalline silicon material) poses some performance limitations on signal insertion loss, cut-off frequency and isolation for this technology. MEMS switch technology was developed with the intention to achieve improved device performance beyond these limitations by adding micro-mechanical movement into microelectronics. In MEMS devices, electrical 'on' and 'off' states are mechanically switched.

Among all the actuation modes, electrostatic actuation is the most prevalent technique because of the following reasons: there is no DC current involved in the actuation process, therefore virtually no DC power is consumed; the actuation electrodes are normally lithographically defined using standard micro-fabrication procedures, therefore they have small size and are compatible with IC fabrication; the switching speed ranges from 1 to 200 μs and is much higher than thermal or magneto-static actuation. Table 1.1 shows a performance comparison of FETs, PIN Diode and RF Electrostatic switches. MEMS switches outperform semiconductor switches in the areas of power consumption, serial resistance (on-state resistance), cut-off frequency, isolation and signal insertion loss. For metal-contact MEMS switches, a high-quality, reliable metal-metal contact is directly tied to low serial resistance, high cut-off frequency and low signal insertion loss.

Table 1: Performance comparison of FETs, PIN Diode and RF MEMS Electrostatic Switches [6]

Parameter	RF MEMS	PIN	FET
Actuation Voltage (V)	20-80	3-5	3-5
Current (mA)	0	3-20	0
Power consumption[a] (mW)	0.05-0.1	5-100	0.05-0.1
Switching time	1-200 μs	1-100 ns	1-100 ns
C_{up} (series) (fF)	1-6	40-80	70-140
R_s (Series) (Ω)	0.5-2	2-4	4-6
Cutoff frequency (THz)	20-80	1-4	0.5-2
Isolation (1-10 GHz)	Very high	High	Medium
Isolation (10-40 GHz)	Very high	Medium	Low
Isolation (60-100 GHz)	High	Medium	None
Loss (1-100 GHz) (dB)	0.05-0.2	0.3-1.2	0.4-2.5
Power handing (W)	< 1	< 10	< 10

[a] Includes voltage up-converter or drive circuitry

Comparing to macro-size electromechanical switches, MEMS switches share the same advantages of having a low-resistance metal contact and high open-contact isolation. But they can be more easily implemented with planar RF circuitry because of their planar fabrication processes. Another drawback of implementing macro-size switches is that they have relatively slow switching speeds (2- 15 ms), which is a few orders of magnitude higher than MEMS switches.

2.2 Categorization and fabrication of RF MEMS switches

There are two classes of RF MEMS switches: capacitive switches and metal-contact switches. Capacitive switches are typically used as shunt switches while metal-contact switches are used as series switches in RF circuits. Shunt switch refers to the switch placed between the signal line and the ground. Serial switch refers to the switch placed between two transmission lines to switch the signal path. For metal-contact switches, the signal is conducted through metal contacts and the applicable signal frequency ranges from DC to 60 GHz. For capacitive switches, the contact is made between the metal and dielectric material. This type of switch utilizes the capacitance modulation to vary signal impedance during switching operation. In the shunt configuration the switch-open state passes RF signal while the switch-close state shorts the signal to ground. Therefore, its applicable signal frequency ranges from 6 GHz to 120 GHz. Our work focuses on metal contact MEMS switches.

RF MEMS switches are typically fabricated using low-temperature processes and are therefore compatible with post-CMOS, SiGe and GaAs integration. Most of them are surface micro-machined and can even be integrated on glass, quartz and polished ceramic substrates. Motorola has demonstrated an integrated RF MEMS switch chip with high voltage charge pump and control logic CMOS in a single package. Extensive use of the this type of integration is expected to meet the future demand of high frequency wireless applications because it can provide the faster switching speed, 3 volt compatibility and reliability [1]. Integration of MEMS switches with GaAs FETs (amplifiers) has also been demonstrated by a few groups such as NTT DoCoMo Inc. and Rockwell scientific [2, 3]. A dual band amplifier net-work with such integration is shown in figure 1 [2]. Nowadays, the manufacture of RF MEMS switches has been mainly carried in highly specialized commercial foundries because of the high diversified fabrication processes. Figure 2 shows the top ten MEMS foundries and their revenues.

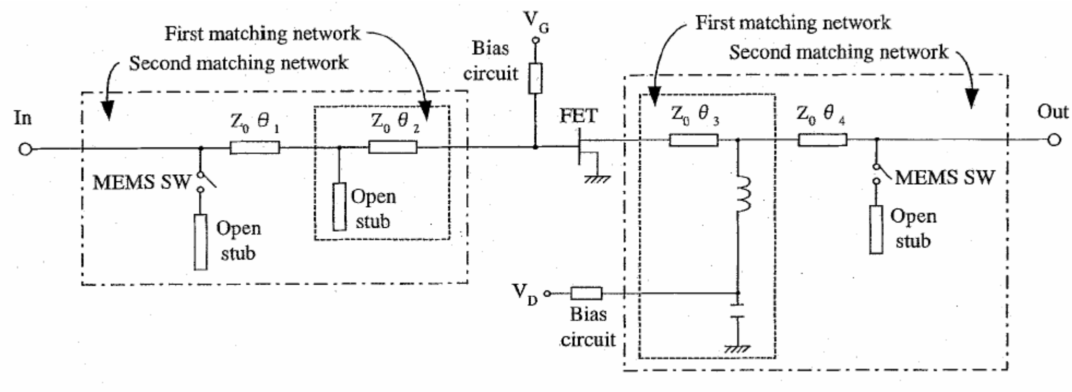

FIG. 1: Schematic of the dual-band amplifier [2].

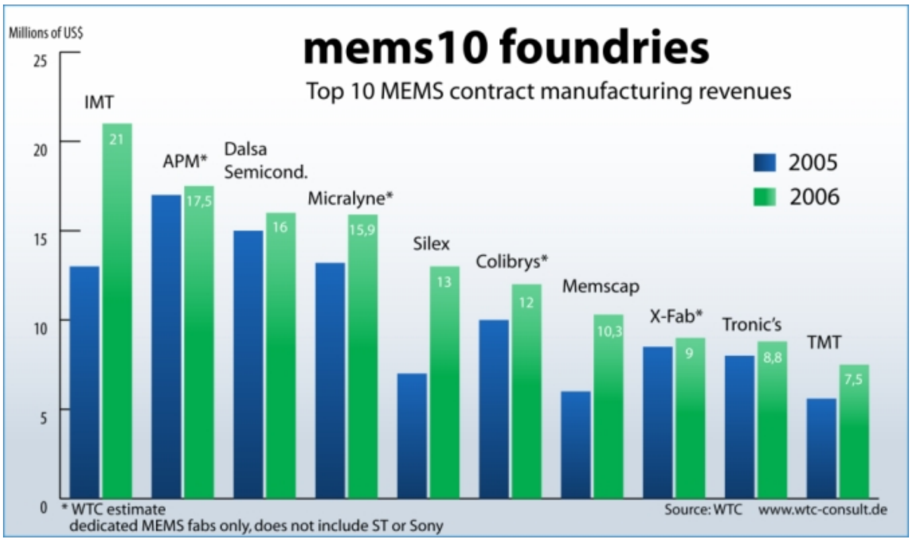

FIG. 2: MEMS top 10 foundries [92].

Figure 3 shows an example of electrostatic, metal-contact MEMS switch [4]. The switch is actuated by the electrostatic force between the two metal-pad electrodes. In order to generate a force for switch actuation, these two metal-pads need to be charged by a DC voltage, which is termed "actuation voltage". When actuation voltage exceeds the threshold value, the upper micro-contacts are lowered by the electrostatic force to contact with the bottom contacts, then signals can be transmitted through. When the metal-pad electrodes are discharged, the switch is opened and the two transmission lines are disconnected. Several important aspects of metal contact MEMS switches are review as following.

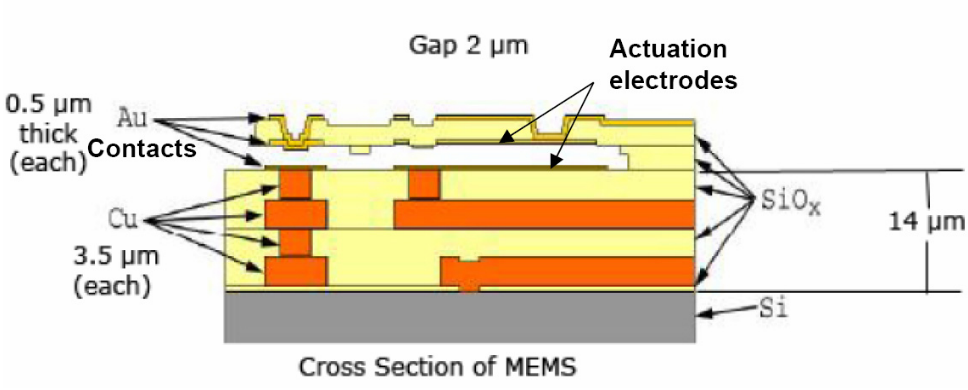

FIG. 3: A schematic of the wiSpry metal contact MEMS switch [4].

2.3 Actuation Mechanics (Electrostatic Switches)

Contact mechanics describe how switch is actuated. For electrostatic switches, the actuation process particularly includes the following steps.

Step 1: Charging of the metal electrode pads located on the upper MEMS cantilever and the bottom substrate

Step 2: Generated electrostatic force brings the upper MEMS cantilever down to a point that the upper micro-contacts make stable contact with the bottom contacts.

Step 3: The two metal electrode pads are discharged; without the electrostatic force, restoring force of the upper MEMS cantilever raises the micro-contacts again.

In order to quantitatively analyze this process, beam deflection models, parallel plate capacitor models and contact force calculations needs to be carefully reviewed.

2.3.1 Cantilever Beam

Since the actuation is mainly realized by the deflection of the upper MEMS cantilever, we assume that the cantilever behaves like a beam, as illustrated by Figure 4. The fixed end is at $x = 0$, a free end at $x = l$, and an intermediately placed external load (F_a) is located at $x = a$ as point source [5, 6].

According to Shigley et al. [5], the maximum beam tip deflection with the intermediately placed load is:

$$d = \frac{F_a a^2}{6EI_z}(3l - a) \tag{1}$$

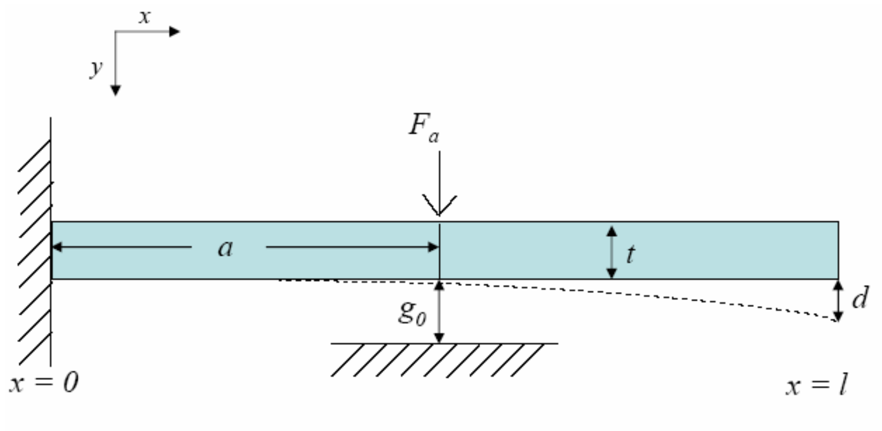

FIG. 4: Cantilever beam model with a fixed end at ($x=0$), a free end at ($x=l$), and an intermediately placed external load, F_a.

where, d is the maximum cantilever beam tip deflection, F_a is the externally applied load, a is the load position, l is the length of the beam, E is the elastic modulus, and I_z is the area moment of inertia about the z-axis, which can be defined as equation 2:

$$I_z = \frac{t^3 w}{12} \qquad (2)$$

where, t is the beam's thickness and w is the beam width.

In equation 1, all the inputs are determined by the beam properties except the external load (F_a) and the maximum cantilever beam tip deflection (d). Actually, if the defection is relatively small, the relation of the force and the defection obeys Hookes' law [5, 7].

$$F = kd \qquad (3)$$

The spring constant k for the beam shown in Figure 5 can be found by solving equation 1 for the applied force and substituting Equation 1 for area moment of inertia. It can be expressed as:

$$k = \frac{Et^3 w}{2a^2(3l - a)} \qquad (4)$$

In our work, this beam model is used to estimate the contact force for the MEMS dynamic switching tests (chapter 4). The calibrated contact force is about 150 µN /micro-contact (300 µN in total). An improved beam model that accounts for anchor can be found in elsewhere [8]. Parallel plate capacitor models are presented next to quantitatively address the question: "How much force can be generated by charging up the capacitor?"

2.3.2 Parallel Plate Capacitor Models

For electrostatic MEMS switches, the actuation force is generated by charging up the metal electrode pads on both the switch's upper cantilever and bottom part. The cantilever and the bottom electrode therefore can be modeled as a parallel plate capacitor. The charge on the parallel plate capacitor can be expressed by equation 5.

$$Q = CV \tag{5}$$

where, Q is the charge, C is the capacitance, and V is the voltage across the parallel plate capacitor. The capacitance of a parallel plate capacitor is given by

$$C = \frac{\varepsilon_0 A}{g} \tag{6}$$

where, ε_0 is the permittivity of free space, A is the surface area of the parallel plate, and g is the distance or gap between the plates. The work required to charge the capacitor from 0 to Q coulombs is give by:

$$W = \int_0^Q \frac{q}{C} dq = \frac{Q^2}{2C} \tag{7}$$

where, W is the work, and q is the integration variable that represents the charge on the capacitance [9]. Substituting in Equation 5 for charge and Equation 6 for capacitance into Equation 7 results in:

$$W = \frac{\varepsilon_0 A V^2}{2g} \tag{8}$$

Since this work is used to charge the capacitance, it finally converted to the potential energy (U) stored in the parallel plate capacitor. This potential energy causes the actuation, therefore, triggers the change of gap distance. The varying electrostatic force (F_e) in the actuation process can be derived from the potential energy (U) [9, 10].

$$F_e = \frac{-dU}{dg} \tag{9}$$

If we substitute Equation 8 into Equation 9, the electrostatic force can be expressed by the actuation voltage:

$$F_e = \frac{\varepsilon_0 A V^2}{2g^2} \tag{10}$$

First-order fringing field correction has been used to account for non-parallel electric fields developed outside of the confines of the parallel plate capacitor. With this correction, the electrostatic force is expressed by Equation 11.

$$F_e = \frac{\varepsilon_0 A V^2}{2g^2}[1 + 0.42\frac{g_0}{w}] \tag{11}$$

For an electrostatic MEMS switch, the electrostatic force F_e equals the cantilever restoring force F_s when the cantilever is in equilibrium. Therefore, Equation 3 can be substituted into Equation 10 resulting:

$$V = (g_0 - d)\sqrt{\frac{2kd}{\varepsilon_0 A}} \tag{12}$$

The pull-in deflection distance (d_{pi}) can be defined as the deflection when the electrostatic force overcomes the beam's mechanical restoring force and the upper micro-contacts are brought down into contact with the bottom contacts. Taking the derivative of the voltage V with respect to the deflection d yields the pull-in defection d_{pi}.

$$\frac{\partial V}{\partial d} = \frac{\partial (g_0 - d)\sqrt{\frac{2kd}{\varepsilon_0 A}}}{\partial d} = -\sqrt{\frac{2kd}{\varepsilon_0 A}} + (g_0 - d)\sqrt{\frac{2k}{\varepsilon_0 A}} \cdot (\frac{1}{2})\frac{1}{\sqrt{d}} = 0$$

$$\Rightarrow d_{pi} = \frac{g_0}{3} \tag{13}$$

Substituting Equation 13 back into Equation 12 yields pull-in voltage V_{pi}.

$$V_{pi} = (g_0 - d_{pi})\sqrt{\frac{2kd_{pi}}{\varepsilon_0 A}}$$

$$= \sqrt{\frac{8g_0^3 k}{27\varepsilon_0 A}} \tag{14}$$

If first-order fringing field correction is taken into consideration, the pull-in voltage can be expressed by Equation 15.

$$\sqrt{\frac{8g_0^3 k}{27\varepsilon_0 A(1+0.42\frac{g_0}{w})}} \tag{15}$$

Implementation of these first-order parallel plate capacitor model and simple beam deflection models have been justified by the MEMS design community [6, 11].

2.3.3 Contact Force

In order to achieve an acceptable low contact resistance, certain clean metal contact area is needed. This contact area forms as a result of contact material deformation. Contact force is used to induce this material deformation. If the actual contact force is un-necessarily large, it could cause excessive contact wear, thus fail the device in a short term. On the other hand, if the actual contact force is too small, the resulted contact material deformation may not be large enough to yield an acceptable electrical resistance. Therefore being able to understand

and accurately predict contact force in MEMS switch is of great important for the success of electrostatic MEMS switch design.

For electrostatic MEMS switches, the contact force is relatively low. The values range from tens of μN's up to a few mN's. This contact force is mainly determined by the mechanical switch design.

As has been mentioned in the section 2.3.2 that, the upper micro-contacts can brought down into contact with the bottom contacts by applying a pull-in voltage V_{pi}. However, in this case, the resulted contact material deformation usually is too small to generate a low contact resistance [6]. The solution is to increase the actuation voltage well above the pull-in voltage. Thus the upper cantilever begins to bend after pull-in so that additional force is supplied to the contact area. Friction between the contacts caused by cantilever bending may also help to mechanically wipe contaminant films from the contact area [11].

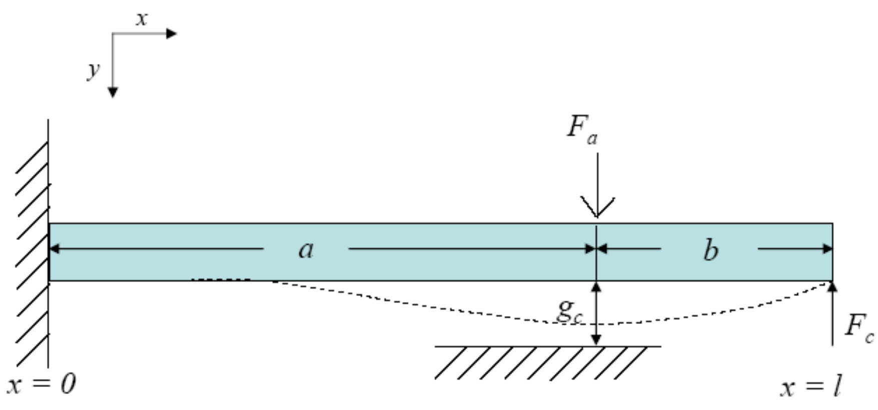

FIG. 5: The additional cantilever deflection after pull-in.

After pull-in, the upper MEMS cantilever can be modeled as a beam with a fixed end *at* $x = 0$, a supported end at $x = l$ (this point is assumed to be the location of upper metal micro-contacts), an intermediately-placed external load F_a (this is the electrostatic driving force) at

$x = a$, and a supporting force F_c at $x = l$ (this is the contact force). Detailed calculation and derivation can be found in the mechanical text book [5]. Only the final form of contact force is given here.

$$F_c = \frac{\varepsilon_0 A V^2 a^2}{4l^3 (g_0 - d)^2}(3l - a) \tag{16}$$

Obviously, this simple, static model does not account for beam tip deflection (no restoring force has been deducted in the calculation), nor material deformation in the contact area after switch closure. Nevertheless, this model has been proven to be valid until the over-driven cantilever collapses onto the bottom electrodes. It is used to analytically determine switch contact force. Recently, Coutu *et al.* have introduced a more detailed contact force model in which contact material deformation and beam deflection are considered [11, 12].

Beam collapse voltage also needs to be estimated to avoid device failure. This value can be calculated following the same procedure of calculating the beam's pull-in voltage (Equation 12). It should be noticed that the spring constant k has been changed to k' after pull-in. Also the new initial gap under the pulled-in beam is defined as g_1. The resulted collapse voltage is shown in Equation 17.

$$V_{cpi} = (g_1 - g_c)\sqrt{\frac{2k' d}{\varepsilon_0 A}} \tag{17}$$

When the driving voltage exceeds this value, a physical contact is established between the cantilever electrode and the bottom driving electrode and the device shorts out.

2.4 Contact Mechanics

Besides contact force, contact resistance is determined by material properties of the contact surfaces such as contact geometry, surface topology, electrical resistivity and micro-hardness. In this section, contact area models, material deformation models, contact resistance and electron transport models are reviewed so that reasonable estimations of contact resistance can be made for electrostatic MEMS switches.

It has been well know that surfaces are rough at microscopic scale. It makes calculation of contact area difficult. Early efforts have involved implementation of Hertzian theory of contact to simulate the contact deformation. Holm later introduced the idea that although the overall stresses are in the elastic regime the local stresses at contact spots may be much higher so that local plastic deformation could occur. This theory has been widely accepted by the research community of electric contact [13]. In 1966, Greenwood and Williamson published a new contact theory which is more closely related to real surfaces than the earlier ones. They showed how contact deformation depends on the topography of the surface, and established the criterion for distinguishing surfaces that deform elastically from those deform plastically. They found that contact between surfaces is frequently plastic, as usually assumed, but surfaces which deforms elastically are by no means uncommon in engineering practice. [14]. Their work forms the base for multiple asperity model. McCool's studies of anisotropic roughness surface with randomly distributed asperities showed good agreement with Greenwood and Williamson's model [16]. In practice, Hertz's model is used for classic elastic deformation while Abbott and Fireston's model is used for plastic deformation with the assumption that no material creep occurs during the deformation process [15]. For the case of elastic-plastic deformation, Chang, Etison & Bogy (CEB) model may be considered [17].

In a simplified single effective asperity model, multiple micro-contact sites are converted into one single effective contact site. The effective contact area is defined as the sum of all the individual contact areas [22]. Calculated resistances from this model are slightly higher than those from the multiple asperity model [23].

In MEMS switch fabrication, planar thin film deposition techniques have been used to minimize the roughness. However, those surfaces of metal micro-contacts are still quite rough when examined at the scale of nano-meters. Therefore, these earlier models should still be applicable. Particularly, much work has been done in the past twenty years with respect to modeling of micro-contact resistance. Majumder et al. modeled the actual micro-switches with a comprehensive consideration of ballistic and diffusive electron transport [18] and various types of contact material deformation [19]. Kogut and Komvopulos developed an electrical contact resistance (ECR) model for conductive rough surfaces with and without thin insulating film separation based on the real contact area [20, 21]. Recently, Coutu *et al.* have updated micro-contact resistance model to account for the surface asperity interaction that occurs in sputtered contact thin films [24]. Although these models, in some cases, has provided some fairly good prediction of the real contact resistance, exact match between simulation and experimental results has not been achieved due to several reasons: firstly, it is difficult to quarantine the pure single-pair contact resistance from resistance measurement of a MEMS switch chip. For example, resistances of other resistive components such as transmission line may be included in the measurement; secondly, slight difference in surface conditions (etc. adsorbed films) may cause measurement variation for each switch; thirdly, real surface topology of the devices normally was not input into the resistance simulation which makes the simulated results less accurate. In this study, our four-point probes *in-situ* contact resistance measurement set-up gets direct access to the micro-contact pairs because of our unique test design (details in chapter 3 and chapter 4). Efficient resistance measurement and good access to both contact surfaces enable us to get good repeatability on experimental results.

Next, different regions of contact material deformation are reviewed in detail because simple calculations based on these fundamental contact physics actually give good prediction of device contact resistance.

2.4.1 Elastic Deformation

Under elastic deformation, the contact area and contact force in single asperity model can be expressed by Equation 18 and Equation 19

$$A = \pi R \alpha \tag{18}$$

where A is contact area, R is asperity peak radius of curvature, and α is asperity vertical deformation.

$$F_c = \frac{4}{3} E^{'} \alpha \sqrt{R\alpha} \tag{19}$$

Where F_c is the normal contact force and E' is the Hertzian modulus which can be derived from Equation 20.

$$\frac{1}{E'} = \frac{1-\nu_1^2}{E_1} + \frac{1-\nu_2^2}{E_2} \tag{20}$$

where, E_1 is the elastic modulus for contact one, v_1 is Poisson's ratio for contact one, E_2 is the elastic modulus for contact two, and v_2 is Poisson's ratio for contact two.

Assume it is a circular area, the effective contact radius can be derived based on Equation 18 and Equation 19.

$$r = \sqrt[3]{\frac{3F_c R}{4E'}} \tag{21}$$

This effective radius is one of the important parameters that determine the switch contact resistance in the case of pure elastic deformation.

2.4.2 Plastic Deformation

Under plastic deformation, the contact area and contact force in single asperity model can be expressed by Equation 22 and Equation 23

$$A = 2\pi R\alpha \tag{22}$$

$$F_c = HA \tag{23}$$

where, H is the hardness and A is the contact area [25, *70*]. Therefore the effective contact radius can be derived as:

$$r = \sqrt{\frac{F_c}{H\pi}} \tag{24}$$

In MEMS community, this simple expression of effective contact resistance has been frequently used to calculate the device contact resistance.

2.4.3 Elastic-Plastic Deformation (The CEB Model)

Chang, Etison & Bogy (CEB) model accounts for the transition region between elastic deformation and plastic deformation. It is a description of a more complicated deformation when parts of the contact area are plastically deformed but encased by elastically deformed material [26].

Contact area is calculated based on conservation of volume of the deformed asperity and the resulted expression is shown by Equation 25, where R denotes the end radius of the curvature of the asperity, α_c is the critical vertical deformation, where plastic yielding is assumed to occur. This parameter is defined by Equation 26, where K_{H} is the hardness coefficient which is assumed to be equal to 0.6 at the onset of plastic deformation [17].

$$A = \pi R \alpha (2 - \frac{\alpha_c}{\alpha}) \tag{25}$$

$$\alpha_c = R(\frac{K_H H\pi}{2E'})^2 = R(0.3\frac{H\pi}{E'})^2 \tag{26}$$

The contact force on this asperity and the effective contact radius can be calculated respectively using Equation 27 and Equation 28:

$$F_c = K_H HA = 0.6HA \tag{27}$$

$$r = \sqrt{R\alpha(2 - \frac{\alpha_c}{\alpha})} \qquad \alpha > \alpha_c \tag{28}$$

Majumder et al. applied this model to simulate the multiple-asperity rough surface [43]. Later on, more efforts were made by Kogut *et al.* on improving the elastic-plastic modeling [27, 28].

2.5 Contact Resistance Modeling

With no contamination film presented in the contact area, contact resistance is generally equivalent to the constriction resistance of the connection between two conductors. It is called "restriction" because electrical current can only flow through metal-metal contact spots during switch closure. For micro-contacts in MEMS switches, real metal-metal contact sizes may affect the way electrons are transported through these constricted contact spots. And different electron transport mechanisms may result in different forms of constriction resistance.

There are three types of electron transport mechanisms that could occur in MEMS switches: diffusive transport, ballistic transport and quasi-ballistic transport [29]. The ballistic transport occurs when the electron mean free path l_e is larger than the effective contact radius r ($l_e > r$); the quasi-ballistic transport occurs when the electron mean free path is comparable to the effective contact radius ($l_e \sim r$); diffusion occurs when the electron mean free path is much smaller than the effective contact radius ($l_e \ll r$). The distinctively different physical transport processes for diffusive and ballistic transport are shown in FIG. 6.

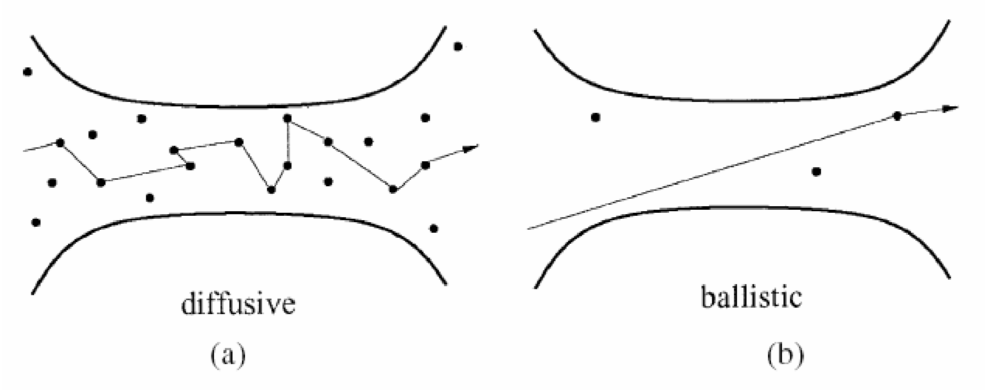

FIG. 6: Schematic illustration of (a) diffusive and (b) ballistic electron transport through a constricted conductor [2].

2.5.1 Diffusive Electron Transport

For diffusive transport, well-established Maxwell spreading resistance equation can be used to calculate the contact resistance [13].

$$R_c = \frac{\rho}{2r} \tag{29}$$

Where, ρ is electrical resistivity.

For elastic deformation, substitute Equation 21 into Equation 29, contact resistance R_{cDE} (DE denotes diffusive transport and elastic deformation) can be expressed in terms of asperity properties and contact force.

$$R_{cDE} = \frac{\rho}{2}\sqrt[3]{\frac{4E'}{3F_c R}} \tag{30}$$

Where, E' again is the Hertzian Modulus which is dependent on the elastic modulus of the upper and bottom contacts, and can be derived from Equation 20.

For plastic deformation, substitute Equation 24 into Equation 29, contact resistance R_{cDP} (DE denotes diffusive transport and plastic deformation) also can be expressed in terms of asperity properties and contact force.

$$R_{cDP} = \frac{\rho}{2}\sqrt{\frac{H\pi}{F_c}} \tag{31}$$

For metal contact MEMS switches with a contact force above 100 μN, it is generally believed that plastic deformation occurs during making contact [6]. Therefore this simple equation has been widely used to predict switch contact resistance.

2.5.2 Ballistic and Quasi-ballistic Electron Transport

For ballistic transport, Sharvin resistance is the major contributor to the contact resistance [19, 30]. The form of Sharvin resistance is given in Equation 32.

$$R_s = \frac{4\rho K}{3\pi r} \tag{32}$$

where, K is the Knudsen number that can be expressed by Equation 33.

$$K = \frac{l_e}{r} \tag{33}$$

An interpolation between the ballistic and diffusive electron transport regions can be made using the Gamma function Γ (K) [31]. A well behaved form of Gamma function is given in Equation 34 [32].

$$\Gamma(K) \approx \frac{2}{\pi}\int_0^\infty e^{-Kx} \sin c(x)dx \tag{34}$$

A plot of “Gamma function vs. Knudsen number” is shown in FIG. 7.

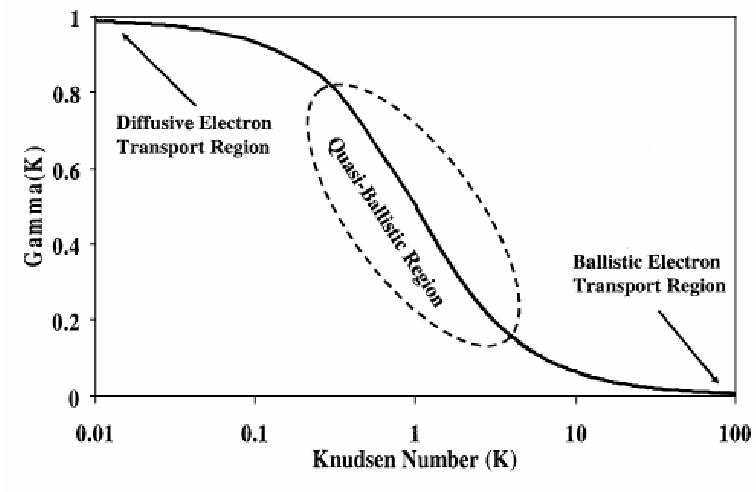

FIG. 7: Plot of Mikrajuddin *et al.*’s plot of ‘Gamma function vs. Knudsen Number [32].

A form complete form of contact resistance is derived by Wexler [31] and is shown in Equation 35.

$$R_w = R_s + \Gamma(K) R_c \tag{35}$$

In our work, contact resistance modeling approach is contingent on two assessments. One is to check whether the effective contact radius is much larger than the electron mean free path so that electron transport mechanism can be determined. In our test, the estimated effective contact radius is more than 100 nm and the mean free path of electrons in gold is only ~ 36 nm. Therefore, diffusive transport model was used for the resistance calculation. The second is to check whether the plastic yielding point is reached so that deformation model can be properly assessed. In our case, plastic deformation is assumed based on the contact force and critical yielding estimation. It turns out that calculation based on these proper assessments gives a fairly good prediction of our experimental contact resistance.

2.6 Contact Metal Alloys

2.6.1 Actuation Voltage Issue.

As for electrostatic MEMS switches, the actuation voltage is normally in range of tens of volts which is an order of magnitude than typical RF circuit voltage. The solution is to convert low voltage to the required actuation voltage using a voltage charge pump and integrate it with MEMS switches. For example, Motorola adopted this configuration for its RF MEMS chips [1]. Discrete voltage charge pump has also been commercialized [33]. Innovative electrostatic mechanical switch designs have also been studied extensively to lower the actuation voltage [6, 34-41]. A trade-off between beam spring constant and switch actuation voltage is discovered in the work: the actuation voltage decreases with a decreasing beam spring constant. The problem is that by lowering the beam spring constant, the switch restoring force is also lowered assuming the deflection of the beam is the same (which is normally the case). As a result, it increases the risk of stiction failure. Up to now, only limited success has been achieved using mechanical design solution with respect to this problem [42]. This failure mode is also directly related to the high adhesion energy between two pure gold surfaces and will be discussed later.

2.6.2 Material Approach

Another approach to minimize the stiction and enhance the wear resistance is to use different metals or alloys as the switch contact materials. Schimkat used rivets made of pure Au, Au-Ni (5 %) alloy and Rh to test their potentials as the contact materials for micro-switches. [43] Technically, the samples are still macro-size although the contact force has been lowered to micro-Newton range. After the “Schaltreinigung” cleaning (Initial run of 40 hot switching cycles with 50 VDC and 50 mA to clean the contamination layer on the metal surfaces), contact resistance of ~ 10 mΩ was achieved under a force load of ~100 μN. However, much higher contact resistances have been reported for actual micro-switches [44-48]. Schimkat also found that much less surface adhesion was generated if harder metals (Au-Ni (5 %) and Rh) were used although a larger contact force was needed (to achieve a low, stable resistance).

Coutu have investigated using different gold alloys (Au, AuPt, AuPd, AuAg, AuPtCu etc.) as the contact materials of the actual MEMS switches [48]. The alloy system selection was based on the rule of avoiding two-phase micro-structure although the reason of using this rule has not been well established. Cotu's work focuses on characterization of the basic material properties such as hardness, electrical resistivity and element composition. His predicted contact resistances (based on the material properties and contact force) fall in the range of between 0.20 ~ 0.6 Ohm. Mostly likely due to the contamination films, his measured contact resistance was normally much higher than the predicted values with the only exception of the AuPtCu alloy (simulated value: 0.2 Ohm, measured value: 0.33) [48]. Obviously, in order to understand the material-related micro-contact performance, surface conditions and material micro-structures needs be carefully addressed.

Majumder *et al.* and Duffy *et al.* have utilized "platinum group" and platinum contact metals respectively to reduce the stiction, thus to extend the switch lifetime [49, 50] In Duffy's case, contact resistance below 1 Ohm can be achieved using an actuation voltage 45 V higher than the actuation threshold voltage (~ 35 V). In Majumder's case, the single contact resistance is around 3 Ohm. More than four parallel contacts are needed to bring contact resistance below 1 Ohm. So generally there is a trade-off between contact resistance and wear resistance / low adhesion. To minimize the contact resistance while dramatically increasing the wear resistance is always the goal of the material scientists in this field.

McGruer *et al.* utilized a MEMS switching test simulator to examine the candidate contact materials [51]. It was found that Pt, Ru, Rh and Au-Ru alloys not only yield much higher contact resistance, but also fail earlier due to a quick rise of contact resistance during the test in ambient air. Material-dependent adsorption of contaminations from air was considered as an issue for Pt, Ru and Rh.

As a summary of the above work, we can see that hardened gold alloys have been used alternative contact materials for MEMS switches hoping to reduce contact surface adhesion and enhance the wear resistance. These materials have demonstrated some different micro-contacting performance in terms of contact resistance and switch cycling lifetime. For example, Coutu et al. pointed out that binary / ternary gold alloys may increase the switch lifetime at some cost of contact resistance. However, in general, material scientists haven't been able to address the micro-contacting performance based on the specific material properties such as surface topology, crystallographic features (micro-structure), micro-hardness and electrical resistivity. The correction between material properties and contacting performance has not been established. In addition, no binary or ternary gold-based alloy system has been systematically investigated regarding its potential use as MEMS contact materials. It is the author's opinion that by systematically studying one gold-based alloy system, one can more easily differentiate the effects from different material properties on contacting performance because of the limited variables. In order to select a promising material system for this purpose, one needs to understand how material selection and preparation could affect those critical material properties (etc. micro-hardness, surface topology, electrical resistivity). Material strengthening theory in the following sections serves as the background knowledge for our purpose.

2.6.3 Solid Solution Hardening

Material can be hardened by the addition of small quantities of an alloying element. For solid solution hardening, the increase of the hardness is not due to any change in microstructure of the alloy. The microstructure remains the same. It is the lattice strains that cause the strengthening and hardening of the alloy. The lattice strains are introduced into the material by those added solute atoms [52]. The solute may incorporate into the solvent crystal lattice substitutionally, by replacing a solvent particle in the lattice or, interstitially, by fitting into the space between solvent particles. Both of these types of solid solution affect the properties of the material by distorting the crystal lattice and disrupting the physical and electrical homogeneity of the solvent material.

2.6.4 Second Phase Hardening

Second phase hardening (also called dispersion hardening, precipitation hardening or age hardening) is achieved by introducing precipitations into the host atom matrix. A heating treatment technique is normally used induce the precipitations depending on the changes in solid solubility with temperature of specific material systems. Fine precipitated second-phase particles impede the movement of dislocations or defects in the crystal's lattice. Since dislocations are often the dominant carriers of plasticity, by impeding the dislocations, one can increase material hardness (which means that it is harder to deform the material) [53].

During the heating treatment, the micro-structure is changed which may cause changes of local chemical composition, hardness and electrical properties. Next, Au-Ni material system is investigated as a possible choice of the metal contact material for MEMS switch application.

2.6.5 An Example: Au-Ni System

Figure 8 shows the equilibrium binary alloy phase diagram for gold-nickel alloy [54]. Our interested region is located in low-nickel composition side (≤ 20 Ni at. %). The intention is to minimize the electrical resistivity while still achieving some hardening effect. As can be observed in Figure 5, both metals are FCC structures, and exist as a two phase mixture at relatively low temperature under equilibrium conditions. However, a metastable single phase alloy may also be produced under the low processing temperatures utilized for the film deposition. Thus, a comparison of the metastable solid-solutions and the two-phase mixtures of the same overall composition can be undertaken, so that both microstructure effects and composition effects can be examined. Schimkat tested gold-nickel (Au- (5%) Ni) macro-switch electric contact under low contact force (100 – 600 μN) conditions [43]. He found that Au-Ni alloy contacts yield much lower adhesion than pure gold contacts. Relatively low force stable contact and reliable re-opening were also achieved in this report. However, in his study, only samples with one composition (5 % Ni) were investigated, using bulky samples (rivets) as test components. Therefore, to systematically explore this interesting material system, we feel compelled to undertaken a study of a wider range of alloy compositions, tested under a configuration typical of MEMS switches.

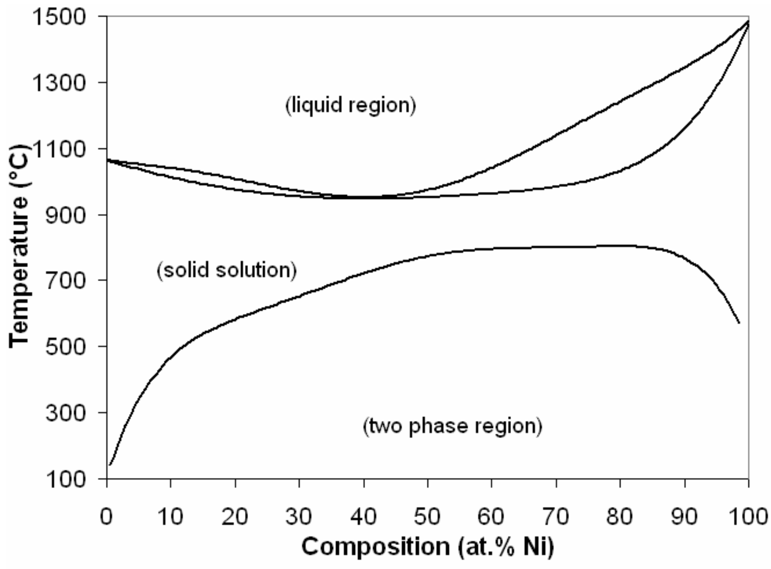

FIG.8: Au-Ni phase diagram, after Okamoto and Massalski [54].

2.7 Contact Degradation Mechanisms

2.7.1 Contact Wear

A recent industrial survey has shown that stiction and wear are the top two failure modes for MEMS actuators [55]. Wear is the erosion of material from a solid surface by the action of another solid. For low-power cold switched micro-switches, mechanical wear such as pitting and hardening of the metal contact area is considered as the dominant failure mechanisms [6]. Pitting and hardening occur as a result of the repeat impaction between two metal contacts. And this may reduce the contact area and therefore increase the contact resistance of the switch. At a high-power level, the switch lifetime is dramatically reduced. For example, many metal contact MEMS switches have achieved multi-billion cycles under low power conditions (0.5-5 mW) but when running at high power conditions (10-100 mW), the switch lifetime is shortened to millions of cycles. Therefore current-induced wear is considered as the major failing factor in this situation. Since electrostatic micro-switches normally generate small forces ranging from 10s μN to ~1 mN, the resulted effective contact radius is only on the order of ~ 100 nm. Under such circumstances, even a small current (ex. ~ 100 mA) flowing through this constricted area could yield high current density and rapidly heat up the micro-contacts causing progressive, non-recoverable material deformation and even melting.

Stiction failure in metal contact switches is a result of the surface adhesion between two metal micro-contacts. It occurs when the adhesive bonding force is greater than the mechanical separation force. High surface adhesion could also induce surface damage and material transfer which can be defined as adhesive wear [56, 57].

2.7.2 Arcing

Metal phase arc has been considered as a possible failure mechanism for hot-switched metal contact MEMS switches [6, 58]. However, this statement has not been justified by the non-arc test conditions [58]. And up to now, no experimental evidence of electric arc (ex. *in-situ* record of I-V transients) in MEMS switches has been reported. One purpose of our work is to investigate the non-arc hot-switching failure mechanisms for metal contact MEMS switches. A review of related previous work is presented below.

Research of arcing can be traced back to the development of electric relays and switches in the early 20th century. Most commonly, it relates to an 'electric arc' between the electrical contacts in the devices. In medium- and high- power electrical circuits, contact metal can be vaporized by an arc at high current (thousands of amperes). In addition to the vaporization, the violently produced vapor 'blows' out drops of liquid metal from the contact. Material transfer, in this case, is typically dominated by excessive field- induced current heating, and thus does not have significant directionality. At lower power level, directional arc transfer normally can be observed. The arc process can be divided into two phases, termed metal phase arc and gas phase arc, due to the difference in material transfer mechanism. Contact material typically transfers from anode to cathode in the early stage of a metal phase arc while reverses the direction in a gas phase arc [59, 60]. For the case of MEMS switches, only low-power, metal phase arc is possible due to the small device size and micron-scale metal contact separation.

Low-power, directional material transfer has been investigated at low DC electric power level with seperation length (gap between two electrode planes) down to 0.1 um [61]; current down to mA range [62] and voltage down to the ionization energies [63-65]. Much of these macro-contact work shows that there is no detectable directional material transfer when the open circuit voltage is lowered below the ionization voltage (non-inductive circuit) or the current is lowered below certain threshold value. Metal phase arc theory has been developed based on these experiments. According to this theory, the material transfer process in the early stage of contact separation is as following: the contact area is decreased as the contacts separates. Consequently, the constriction resistance, contact voltage and temperature in the constriction area increase rapidly up to boiling point (the contact voltage and boiling temperature of gold are 0.97 V and 3080.15K). Part of the molten bridge material gets evaporated. Across the hot and dense metal vapor, there is a strong electrical field within the small separation gap. It causes field emission of electrons from the cathode. These electrons excite and stepwise ionize the metal atoms (evidences of high excited metal ions have been reported [66-69]). Thereafter these metals are transferred following the field toward the cathode. This arc process is sustained by cathodic electron emission. It is commonly believed that below the ionization voltage, electrons can not have enough energy to ionize the metal ions and below certain threshold current, this process can not be sustained. Up to now, the reported minimum arc voltage and minimum arc current for gold are 12.42 volt and 0.35 A respectively.

Material transfer below the threshold voltage and threshold current first was named “fine transfer” (bridge transfer) by Holm in 1950s. This kind of material transfer was claimed to be caused by asymmetric rupture of the bridge of molten contact material appearing between opening contacts. And the asymmetric rupture was ascribed to the shift of the hottest point from the middle due to DC current heating. However, this theory seems to be contradictory with the experimental facts [70-71] and received rare acceptance.

2.7.3 Field Induced Material Transfer

In this dissertation, field evaporation, for the first time, is explored as a contact degradation mechanism for metal contact MEMS switches**.** Our work suggests that high-temperature field evaporation could be responsible the dramatic micro-contact degradation process under the non-arc test conditions (which is the normal case for hot-switched MEMS switches).

The research of field evaporation is originally tied to the invention of Field Ion Microscopy (FIM) which gives atomic resolution image of surfaces [72, 73]. In these instruments, extremely high field (multi-mega volts per centimeter) is used to force surface atoms off the tip sample and project them onto a flat screen. With the great advances in

Scanning Probe Microscope (SPM) techniques, low-voltage (normally below the material ionization voltage) field induced material transfer phenomenon has been studied at atomic scale using scanning tunneling microscope (STM) since the late 80s. *Becker et al.* was the first to show that an atom might be purposefully transferred between the tip and surface of the STM due to the atomic-scale field perturbation [74]. Thereafter, claims of reliable metal nano-dot deposition followed [75-77]. Atomic scale manipulation of silicon atoms was also reported by Lyo and Avouris [78].

Up to now, most of the nano-dot transfer research work only focuses on the nano- and atomic scale. However, we should notice that these experiments only involve one-time transfer (applies one voltage pulse per location). If the transfer is directional, accumulation of the volume during thousands of cycles (like the operation of MEMS switches) could yield considerable, micrometer-scale material transfer. Actually the test conditions in these STM/ AFM experiments are quite similar to those in the MEMS switching tests. The similar aspects can be summarized as following:

1. The AFM/ STM tips can be similar to the metal upper micro-contacts of MEMS switches. Normally, the radius of the AFM / STM tips ranges from tens of nanometers to micrometers. For the micro-contacts in electrostatic MEMS switches, real contact radius are on the order of ~ 100 nm (it is only a small fraction of the micro-contact top surface area) [6].
2. The test conditions are similar: for AFM/ STM nano-transfer experiments, the magnitude of the voltage pulse during the transfer ranges from 2 volts to 9 volts (typically below the material ionization voltage). And there is a strong electrical field across the tip-sample

gap during the transfer. Hot-switched MEMS switches are operated under very similar conditions. Solid evidence has been provided by Pascual *et al.* [79] showing that mechanical contact is highly possible during these AFM/ STM nano-transfer experiments although many researchers tend to neglect this fact.

Therefore, previous research work of nano-transfer could be potentially beneficial to our current research of non-arc failure of MEMS switches. A brief review of the related theories and important results are given in the following sections.

The field evaporation nano-transfer theory (between tip-sample) was first proposed by Tsong [80]. He found that the critical transfer field can be lowered by adding the tip-sample interaction term to the classic field evaporation models [81, 82]. Figure 9 shows the potential-energy diagram for field evaporation of metals in anisolated tip geometry of FIM.

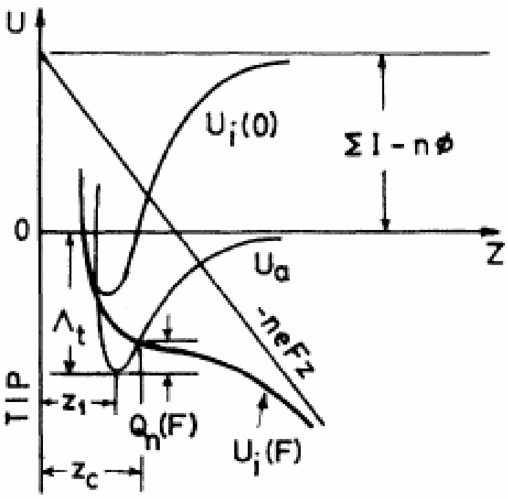

FIG.9: A potential-energy diagram for field evaporation of metals in an isolated tip geometry of the FIM [80]. U_a is the potential curve for the metal atom; U_i (0) is the potential curve for the metal ion in absence of applied electrical field; U_i (F) is the potential curve for the metal ion with an applied field.

According to this diagram, the ionization energy barrier is lowered to $Q_n(F)$ in the presence of a strong electrical field. And **field evaporation rate** can be defined by Equation 36.

$$\kappa = \nu \cdot \exp(-\frac{Q_0}{kT}) \tag{36}$$

where, k is the transfer rate, ν is the atom vibration frequency ($\sim 10^{13}$ s^{-1}), Q_0 is the ionization energy barrier. The **Critical evaporation field** can be defined as the field required for one ionization event per second at room temperature. The critical evaporation field for gold (Au^+) is ~ 35 V/ nm in a FIM configuration [83]. This critical field can be further lowered using a STM (tip-sample) configuration. Figure 10 shows the potential-energy diagram for field evaporation of metals in a STM configuration when a positive field is applied to the tip.

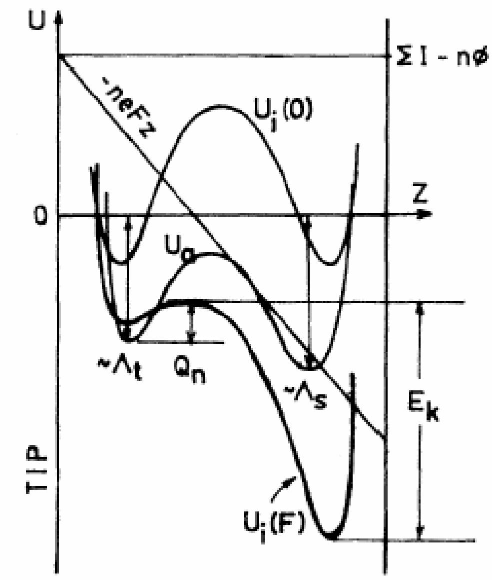

FIG.10: A potential-energy diagram for field evaporation of metals in a STM configuration when a positive field is applied to the tip [80].

Tsong calculated the critical evaporation field of a variety of metals with a tip-sample distance of 6 Å. Critical field evaporation of gold (Au^+) under this circumstance is only slightly reduced to 32.3 V/ nm. His calculation also indicates that negative gold ions (Au^-) have the lowest critical field (17.1 V/ nm), thus would be more likely created and transferred. However, this negative gold ion has never been observed (etc. by FIM).

On the other hand, inconsistency in a number of experimental results has caused confusion about nano-scale field induced material transfer. In 1990, Mamin *et al.* demonstrated gold nano-dot can be reliably deposited on flat gold samples by applying negative voltage pulses to the gold STM tip [75]. The experimental critical field was only 4 V/nm, which is much lower than Tsong's predicted values even if negative gold ions did exist in the process. His multiple-negative-pulse experiment over the same location showed a stepwise removal of material from the bottom sample (shown in Figure 11) while single-negative-pulse creates mounds on the bottom sample (shown in Figure 12) [77].

The transfer directionality was further complicated by Chang *et al.*'s gold nano-dot transfer experiment. Their set-up is quite similar to that of Mamin *et al*'s but the results are quite different. In these experiments, mounds of gold atoms and pits can be produced on a gold surface with nearly equal probabilities when voltage pulses are applied to the gold tip Figure 10 shows the STM images of the generation of mounds and pits in the experiments. It can seen that, in many cases, atoms are transferred both from the tip to the sample and from the sample to the tip, thus creating both a mound and a pit at nearly the same location. A mound can be either on the right- or the left-hand side of a pit and sometimes they are at the same spot (looks just like a material build-up). It was in inferred by Chang based on these facts that the critical fields for evaporating in negative and positive fields are nearly identical [84]. With a dissimilar PtIr tip/Au substrate system, Bessho *et al.* found a polarity-dependence for mound fabrication: the material transfer seems to follow the electrical field [85].

Even with nearly two decades of research efforts on nano- to atomic-scale field evaporation of gold, the basic mechanism hasn't been unraveled. As a major issue, the pulse polarity dependence of the transfer hasn't been clearly resolved. And we believe that achieving a good understanding of nano-scale field-induced gold nano-dot transfer should be beneficial to the design and processing of future MEMS devices as well as the research of basic nano-science.

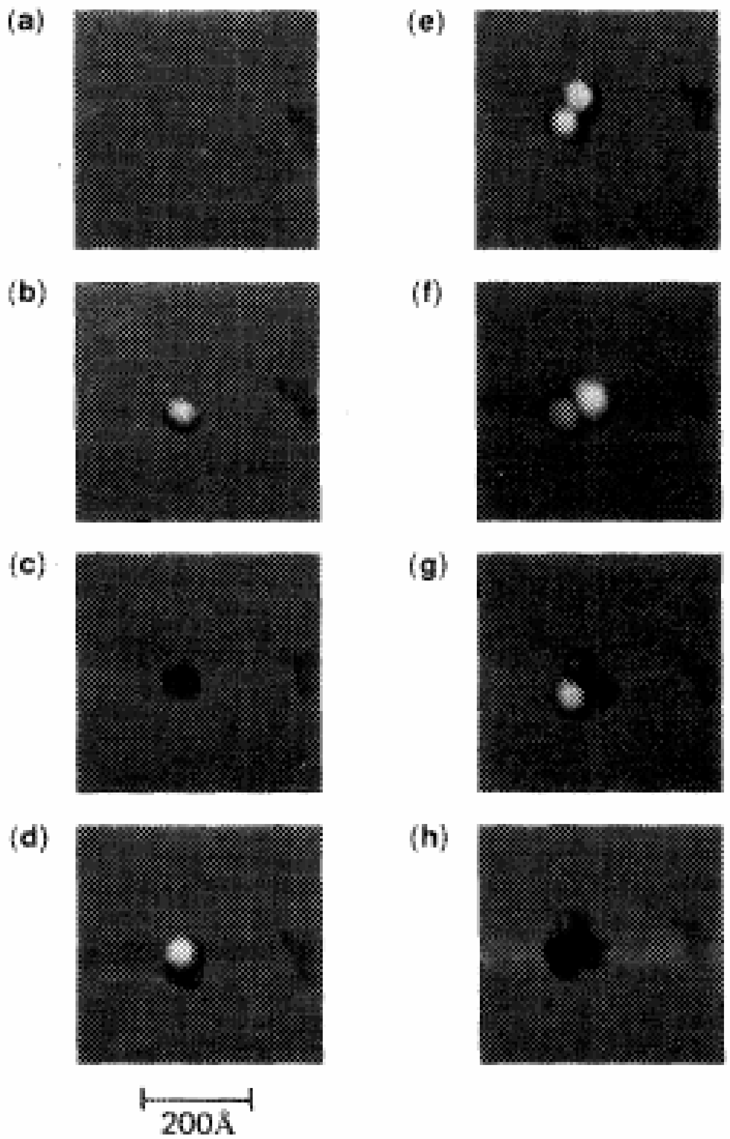

FIG. 11: Effect of multiple pulses over a single spot. All pulses were -4.0 V, 300 ns. (a) Flat spot on surface. (b) Bump created with single pulse. (c) Pit left after subsequent pulse. (d) Pit partly filled by another pulse. (e) and (f) Pulse applied with tip centered over deepest part of pit. (g) and (h) pulse applied with tip centered over highest surface feature [77].

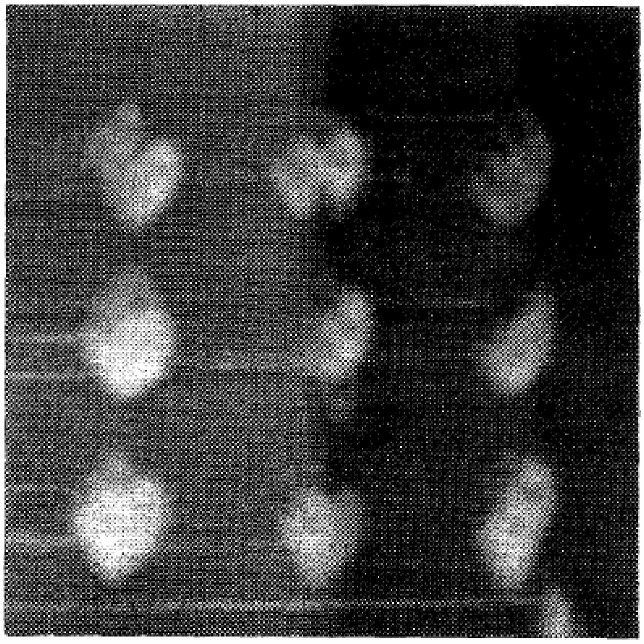

FIG. 12: Array of mounds created on Au (1 1 1) single crystal with -4.7 V, 20 ns pulses applied to the tip. Scanned area is 3000 × 3000 Å [77].

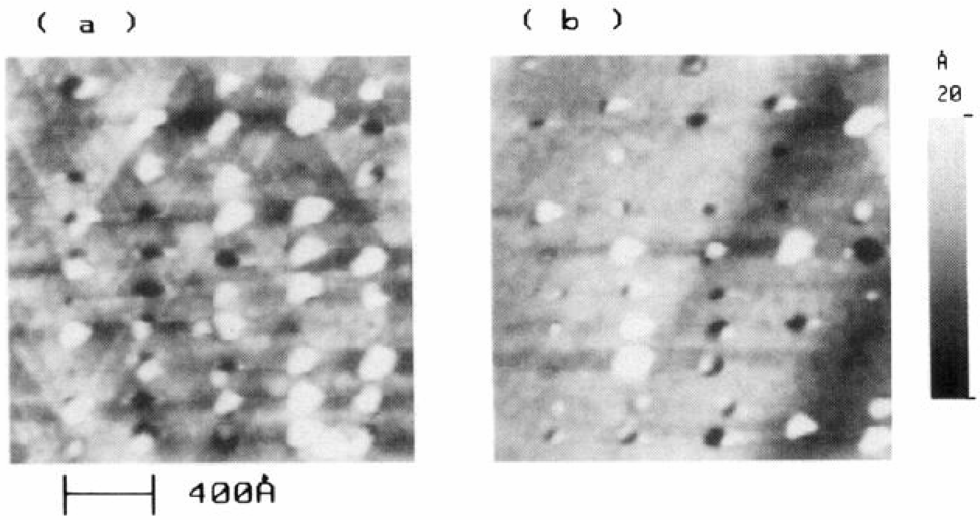

FIG. 13: Generation of mounds and pits by applying the same pulse at 48 pre-selected positions in a frame for two different pulse voltages at a constant tip-sample distance. (a)-3.9 V and (b) -3.5 V [84].

2.7.4 Contaminant Film Issue in MEMS Switches

In MEMS switches, contaminant film issue needs be more carefully addressed because the small contact force may not be able to penetrate these films. The composition and thickness of these contaminant films vary depending on the specific type of contact metal.

Common contact metals for macro-switches (etc. iron, copper and silver) are not used as contact materials in MEMS switches because they are prone to oxidation and corrosion [86]. Instead, gold is chosen for its high resistance to corrosion. Nevertheless, gold still absorbs mono-layers of hydrocarbons and water film when exposed to ambient air. These adsorbed films, typically 20- 40 Å thick, can be mechanically removed / penetrated with a contact force of hundreds of μNs [43, 13, 87]. Temperature-dependent behavior of contaminant films on gold contact surface was also investigated by [88, 89]. Figure 14 shows the comparison of contact resistance for contacts operated at two different temperatures. This result suggests that elevated temperature resulting from contact heating is responsible for removing the insulating films from the contact area. It also should be noted that the contact force in this particular experiment is only 48 μN.

Micro-contacts can also be "cleaned" by hot-switching operation which can be thought as an internal electrical heating method [90, 91]. Unfortunately, most hot-switching cleaning experiments have resulted in contact degradation due to material transfer.

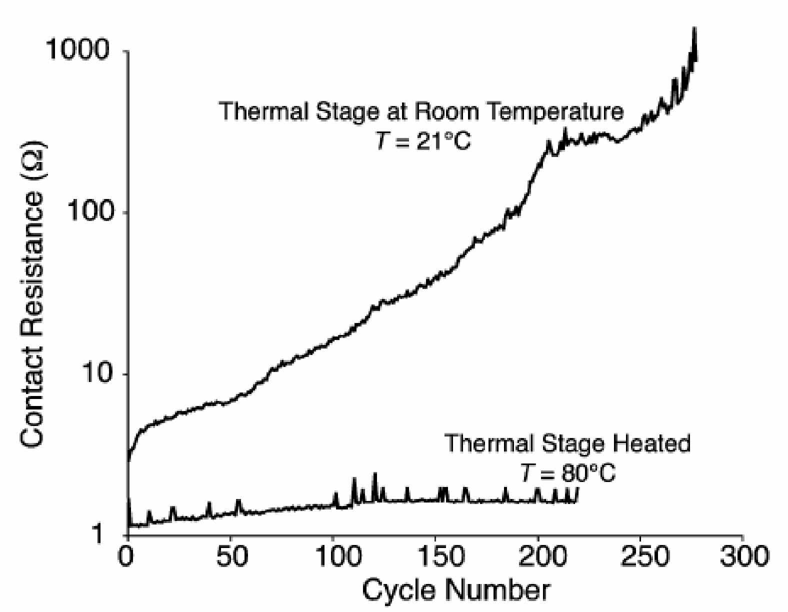

FIG. 14: Comparison of contact resistance for contacts operated at room-temperature and heated to 80 ^{o}C [88].

2.8 The Focus of Our Work

In the above review, a few specific subjects are clearly in need of more investigation and have become the focus of our work. These subjects are briefly presented in the following sections.

1. From the above review of previously reported work on material selection for metal contact MEMS switches, we can see a correlation between material properties, microstructures and micro-contacting performance has not been well established. No alloy material system has ever been systematically studied. On the aspect of experiments, it is quite difficult to achieve efficient micro-contact degradation tests that mimic the MEMS switch operation.

2. From the above review of previously reported work on failure analysis of metal contact MEMS switches, we can see that the failure analysis is relatively limited and, up to now, only some qualitative characterization is available. It could be due to the following reasons: firstly it is quite difficult to characterize failed MEMS switches because of their tiny, fragile device structure; secondly, the design of MEMS switches is highly diversified and no comprehensive failure investigation has been reported on a single type of switches.
3. From the review of previously proposed failure mechanisms for hot switching MEMS switches, we can see that the claim of metal phase arc as the major contact degradation mode for switches under non-arc conditions is not solid. And no supportive evidence has been reported. And more investigation is needed to achieve a clear understanding of this subject.

In the following chapters, our work is presented in details in order to address the above research topics of our interest.

2.9 References

[1] A. P. De Silva et al, "Motorola MEMS switch technology for high frequency applications," Microelectromechanical Systems Conference, 24-26 (Aug. 2001)

[2] A. Fukuda, H. Okazaki, T. Hirota, Y. Yamao, "Novel 900 MHz/ 1.9 GHz dual-mode power amplifier employing MEMS switches for optimum matching," IEEE Microwave and Wireless Components Letters, 14(3), pp. 121-123, 2004

[3] M. Kim, J. B. Hacker, R. E. Mihailovich, and J. F. DeNatale, " A monolithic MEMS switched dual-path power amplifier, IEEE Microwave Wireless Components Letters, 11(7): pp. 285-286, 2001

[4] A. S. Morris, S. Cunningham, D. Dereus and G. Schopfer, "High-performance integrated RF-MEMS: Part 1 – the process," *Proceedings of 33rd European Microwave Conference*, 2003, pp. 21-24

[5] J. Shigley, C. R. Mischke and R. G. Budynas, *Mechanical Engineering Design* (5th Eidtion). New York: McGraw-Hill, Inc. 1990

[6] G. M. Rebeiz, RF MEMS Theory, design, and technology, New Jersey: John Wiley & Sons, Inc. 2003

[7] M. R. Lindegurn, *Engineer-in-Training Reference Manual* (8th Edition), CA: Professional Publications, Inc., 1992

[8] Meng, M. Mehregany and R. L. Mullen, "Theoretical modeling of micro-fabricated beam with elastically restrained supports," *IEEE/ASME J. MEMS,* 2 (3): pp. 128-137, 1993.

[9] R. A. Serway, *Physics for Scientists and Engineers*. New York: Saunders College

Publishing, 1986

[10] R. B. Yarborough et al., *Electrical Engineer Reference Manual* (5^{th} Edition), CA: Professional Publications, Inc. 1990

[11] R. A. Coutu, Ph.D. Dissertation: *Electrostatic radio frequency (RF) microelectromechanical systems (MEMS) switches with metal alloy electric contacts*, Air Force Institute of Technology, September 2004

[12] R. A. Coutu, P. E. Kladitis, "Contact force models, including electric contact deformation, for electrostatically actuated, cantilever-style RF MEMS switches," *Proc. NSTI 2004 Nanotechnology Conference and Trade Show,* 2, 219-223 (March 2004)

[13] R. Holm, *Electric Contacts: Theory and Applications*. Berlin, Germany: Springer, = 1969

[14] J. A. Greenwood and J. B. P. Williamson, "Contact of nominally flat surfaces," *Proc. Royal Soc.* A., 295: 257-263 (1966)

[15] E. Abbot and F. Firestone, "Specifying surface quantity – a method based on the accurate measurement and comparison, " *ASME Mech. Eng.,* 55, p. 569, 1933

[16] J. I. McCool, "Predicting microfracture in ceramics via a microcontact model," *ASME Journal of Tribology,* 108: 380-386 (1986)

[17] W. Chang, I. Etison and D. Bogy, "An elastic-plastic model for the contact of rough surfaces," *ASME J. Tribol.,* 109, pp. 257-263, 1987

[18] G. Wexler, "The size effect and the nonlocal Boltzmann transport equation in orifice and disk geometry," in *Proc. Phys. Soc.* 89, pp. 927-941, 1966

[19] S. Majumder *et al.,* "Study of contacts in an electrostatically actuated microswitch,"

Sens. Act. A., 93 (1): pp. 19-26, 2001

[20] L. Kogut and K. Komvopolous, "Electrical contact resistance theory for conductive rough surfaces*," Amer. Inst. Phys.*, 94 (5): pp. 3153-3162, 2003

[21] L. Kogut *et al.,* "Electrical contact resistance theory for conductive rough surfaces separated by a thin insulating film," *Amer. Inst. Phys.,* 94 (2): pp. 576-585, 2003

[22] B. Bhushan, "Contact mechanics of rough surfaces in tribology: single asperity contact," *Tribology Letter,* 4: pp. 1-35 (1998)

[23] S. Majumder, N. E. McGruer, G. G. Adams, P. M. Zavracky, R. H. Morrison and J. Krim, "Measurement and Modeling of surface micromachined, electrostatically actuated microswitches" 1997 international conference on solid state sensors and actuators, chicago, p 1145 (1997)

[24] R. A. Coutu, P. E. Kladitis, K. D. Leedy and R. L. Crane, " Selecting metal alloy electric contact materials for MEMS switches," *J. Micromech. Microeng.* vol.14, pp. 1157-1164, 2004

[25] W. R. Chang, "An elastic-plastic model for a rough surface with an ion-plated soft metallic coating," *Wear,* 212: pp. 229-237 (1997)

[26] W. J. Stronge*, Impact Mechanics,* United Kingdom: Cambridge University Press, 2000

[27] L. Kogut and I. Etison, "Elastic-plastic contact analysis of a sphere and a rigid flat," *J. App. Mech.,* 69: pp. 657-662, 2002

[28] L. Kogut and I. Etison, "A finite element based elastic-plastic model for the contact of rough surfaces," *Tribology Transactions*, 46 (3): pp. 383-390, 2003

[29] N. Agrait, A. L. Yehati and J. M. V. Ruitenbeek, “Quantum properties of atomic-sized conductors,” *Physics Reports,* 377: pp. 81-279, 2003

[30] Y. V. Sharvin *Sov. Phys. JETP*, 21: p. 655 (1965)

[31] G. Wexler, “The size effect and the non-local Boltzmann transport equation in orifice and disk geometry,” Proc. Phys. Soc., 89: p. 927, 1966

[32] A. Mikrajuddin, F. G. Shi, H. K. Kim, and K. Okuyama, “Size dependent electrical constriction resistance for contacts of arbitrary size: from Sharvin to Holm limits,” *Mat. Sci. in Semi. Proc.*, 2: pp. 321-327, 1999

[33] TeraVicta website: http://www.teravicta.com/site/pumps.html

[34] P. Attia, G. Tremblay, P. Laval and P. Hesto, “ Characteristics of a low-voltage actuated gold microswitch,” Mat. Sci. and Eng., B31: pp. 263-266 (1998)

[35] D. Becher, R. Chan, M. Hattendorf and M. Feng, “Reliability study of low-voltage RF MEMS switches,” Proc. GaAs MANTECH Conf. 03e (April 2002)

[36] R. Chan, R. Lesnick, D. Becher and M. Feng, “Low actuation voltage RF MEMS shunt switch with cold switching lifetime of seven billion cycles,” J. of MEMS 12(5): pp. 713-719 ,2003

[37] C. Chang and P. Chang, “Innovative micro-machined microwave switch with very low insertion loss,” Sensors and Actuators A.. 79: pp. 71-75, 2000

[38] J. Oberhammer and G. Stemme, “Low-voltage high-isolation DC-to-RF MEMS switch based on an S-shaped film actuator,” IEEE Trans. on Elec. Dev. 51(1): pp. 149-154, 2004

[39] D. Peroulis, S. P. Pacheco, K. Sarabandi and L. P. B. Katehi, “Electromechanical

considerations in developing low-voltage RF MEMS switches," IEEE Trans. on MTT, 51(1): pp. 259-270 (2003)

[40] I. Schiele, J. Huber, B. Hillerich and F. Kozlowski, "Surface micromachined electrostatic microrelay," Sensors and Actuators A. 66: pp. 345-354, 1998

[41] C. H. Chu, W. P. Shih, S. Y. Chung, et al., " A low actuation voltage electrostatic actuator for RF MEMS switch applications,", Journal of Micromechanics and Microengineering 17 (8): pp. 1649-1656, 2007

[42] S. D. Lee, B. Jun, S. D. Kim and K. Mizuno, "An RF-MEMS switch with low actuation voltage and high reliability," J. MEMS, 15 (6): pp. 1605-1611, 2006

[43] J. Schimkat, "Contact materials for microrelays," in 11th Proc. MEMS' 98 Workshop, 1998, pp. 190-194

[44] S. Majumder, N. E. McGruer, G. G. Adams, P. M. Zavracky, R. H. Morrison and J. Krim, "Study of contacts in an electrostatically actuated microswitch," Sensors & Actuators A, 93 (1), pp. 19-26, 2001

[45] S. Hannoe and H. Hosaka,"Characteristics of electrical contacts used for microrelays," Proc. IEEE Int. Symp. Microsyst., Intell. Mater., Robots, in 1995, pp. 173-176

[46] D. Hyman and M. Mehregany "Contact physics of gold microncontacts for MEMS switches", IEEE transactions on components and packaging technology, 22 p. 357, 1999

[47] S. C. Bromley and B. J. Nelson, Electrical Contacts, "Performance of microcontacts tested with a novel MEMS device," Proceedings of the Annual Holm Conference

on Electrical Contacts, 2001, p 122-127.

[48] R. A Coutu, J.R. Reid, R.Cortez, R. E. Strawser and P. E. Kladitis, "Microswitches with sputtered Au, AuPd, Au-on-AuPt, and AuPtCu alloy electric contacts," *IEEE Trans. Comp. Packag. Tech.,* vol. 29, pp. 341-349, 2006

[49] S. Majumder, J. Lampen, R. Morrison and J. Maciel, "MEMS switches," *IEEE Instrumentation & Measurement Magazine,* pp. 12-15 (March 2003)

[50] S. Duffy, C. Bozler, S. Rabe, J. Knecht, L. Travis, P. Wyatt, C. Keast and M. Couker, "MEMS microswitches for reconfigurable microwaves circuitry," *IEEE Microwave and Wireless Components Letters,* 11 (3): pp. 106-108, 2001

[51] N. E. McGruer, G. G. Adams, L. Chen, Z. J. Guo and Y. Du, " Mechanical, thermal, and material influences on ohmic-contact-type MEMS switch operation," in *19th Proc MEMS* '06 Istanbul, Turkey, 2006, pp. 230-233

[52] M. H. Richman, *An introduction to the science of metals,* USA: Blaisdell Publishing Company, 1967

[53] Wikipedia website, 2008 : http://en.wikipedia.org/wiki/Precipitation_hardening

[54] H. Okamoto and T. B. Massalski, *Phase diagrams of binary gold alloys,* Ohio: ASM international, p. 196, 1987

[55] C. Fung, "Industry study on issues of MEMS reliability and acccelerated lifetime testing", *2005 IEEE Int. Reliability Phys. Symp. Proc. 43rd Annu.*, pp 312-16.

[56] G. G. Adams and M. Nosonovshy, "Contact modeling – forces," *Tribology International,* 33: pp. 431-442 (2000).

[57] Y. Ando and J. Ino, “Friction and pull-off forces on submicron-size asperities,” *Wear,* 216: pp. 115-122 (1998).

[58] E. J. J. Kruglick and K. S. J. Pister, “Lateral MEMS microcontact consideration,”, *J. Microelectromechanical Syst.* vol. 8, pp. 264-271, 1999

[59] Z.-K. Chen and K. Sawa, “Effect of arc behavior on materials transfer: A review,” *IEEE Trans. Comp., Packag., Manufact. Technol. A*, vol. 21, pp. 310–322, 1998.

[60] Z. Chen and G. Witter, “Electrical erosion comparison of materials for automotive loads,” in *Proc. 19th ICEC, Addendum (Paper 14)*, p.7, 1998

[61] L. Morin, N. Ben Jemaa, D. Jeannot and H. Sone, “Transition from the anodic arc phase to the cathodic metallic arc phase in vacuum at low DC electrical level,” *IEEE Transactions on Components and Packaging Technologies*, vol. 25, no. 4 p. 651, 2002

[62] H. Mizukoshi, K. Sawa, M. Hasegawa, and K. Niizuma, “An experimental study on material transfer and arc erosion characteristic of Ag contacts under switching lower currents,” *IEICE Trans. Electron.* Vo. E77-C, pp. 1655-1661, 1994

[63] I. Dietrich, “Untersuchungen zum kurzen AbreisBbogen an schwach belasteten elektrischen Kontakten,” *Ann. Phys.*, vol. 7, no. 4, pp. 167-177, 1959

[64] L. H. Germer and W. S. Boyle, “Two distinct types of short arcs,” *J. Appl. Phys.,* vol. 27, pp. 32-39, 1956

[65] J. A. Riddlestone, “Short duration discharges between separating contacts in a 6V circuit,” *Bri. J. Appl. Phys.,* vol. 8, pp. 105-108, 1957

[66] F. Lewellyn-Jones and M. C. Cowburn, “Time-resolved spectroscopy of contact

micro-plasma," in *Proc. 8th ICECP,* 1976, pp. 263-268

[67] A. Kleinle, "Der Mechanismus de kurzen Lichtogen in elektrischen Kontakten," Ph.D. Dissertation, Univ. Frankfurt/ Main, Frankfut, Germany, 1963

[68] M. C. Cowburn and F. Lewellyn-Jones, "Spectroscopic investigation of the radiation emitted from contact micro-arcs," in *Proc. 5th ICECP, 1970,* pp. 281-284.

[69] J. A. Augis and L. L. Hines, "Arc duration in the anodic case," *IEEE Trans. Parts, Hybrids, Packag.* Vol. PHP-11, pp. 11-14, 1975

[70] R. Holm, Electric Contacts Handbook, Springer-Verlag: Berlin/Gottingen/Heidelberg,1958, p. 379

[71] W. F. Rieder, "Low current arc modes of short length and time: A Review", *IEEE Trans. Comp. Packag. Technol.,* vol. 23, no. 2, 2000, pp. 286-292

[72] E. W. Muller, "Field ion microscopy," *Science,* 149 (3684): pp. 591-601, 1965

[73] D. Blavette, A. Bostel, J. M. Sarrau, B. Deconihout and A. Menand, "An atom probe for three-dimensional tomography," *Nature* 363, pp. 432-435, 1993

[74] R. S. Becker, J. A. Golovchenko, B. S. Swartzentmber, "Atomic-scale surface modifications using a tunneling microscope" *Nature* 325**,** p. 419, 1987

[75] H. J. Mamin, P. H. Guethner, D. Rugar, "Atomic emission from a gold scanning tunneling microscope tip," *Phys. Rev. Lett.* 65**,** p. 2418, 1990

[76] D. M. Kolb, R. Ullmann and T. Will, "Nanofabrication of small copper clusters on gold (111) electrodes by a scanning tunneling microscope", *Science* 275, pp. 1097-1099, 1997

[77] H. J. Mamin, S. Chiang, H. Birk, P. H. Guethner and D. Rugar, "Gold deposition

from a scanning tunneling microscope tip," *J. Vac. Sci. Tech. B,* 9 pp. 1398-1402, 1991

[78] I.-W. Lyo and P. Avouris, " Field-induced Nanometer to Atomic-Scale Manipulation of Silicon Surfaces with STM", *Science* 253, p. 173 1991.

[79] J. I. Pascual *et al*., "Quantum contact in gold nanostructures by scanning tunneling microscope," *Phys. Rev. Lett.* 71 (12)**,** pp. 1852-1855, 1993

[80] T. T. Tsong, "Effects of an electric field in atomic manipulations", *Phys. Rev. B* 44, pp. 13703-13710, 1991

[81] R. Gomer and L. W. Swanson, "Theory of field desorption," *J. Chem. Phys.* 38, p. 1613, 1963

[82] E. W. Muller, "Field desorption," *Phys. Rev.* 102, p. 618, 1956

[83] T. T. Tsong, "Field-ion image-formation," *Surf. Sci.* 70, p. 211, 1978

[84] C. S. Chang, W. B. Su and T. T. Tsong, "Field evaporation between a gold tip and a gold surface in the scanning tunneling microscope configuration," Phys. Rev. Lett. 72 (4): p. 574, 1994

[85] K. Bessho and S. Hashimoto "Fabricating nanoscale structures on Au surface with scanning tunneling microscope, " *Appl. Phys. Lett.* 65, p 2142, 1994

[86] Handbook, Committee. Metals Handbook, volume 2 (Tenth Edition), USA: ASM International, 1990

[87] V. V. Konchits and C. K. Kim, "Electric current passage and interface heating," *Wear,* 232: pp. 31-40, 1999

[88] B. D. Jensen, L, L.-W. Chow, K. Huang, K. Saitou, J. L. Volakis and K.

Kurabayashi, “Effect of nanoscale heating on electrical transport in RF MEMS switch contacts,” *J. Microelectromechanical System,* vol 14, n. 5, pp.435-946, 2005.

[89] C. Brown, A. Morris, A. Kingon and J. Krim, “Cryogenic performance of RF MEMS switch contacts,” Submitted to *J. Microelectromechanical System*

[90] D. Hyman and M. Mehregany, “Contact physics of gold microcontacts for MEMS switches*,” IEEE Trans. on CPMT,* 22 (3): pp. 357-364, 1999

[91] J. W. Tringe, T. A. Uhlman, A. C. Oliver and J. E. Houston, “A single asperity study of Au/ Au electrical contacts,” *J. of Appl. Phys.*, 93 (8): pp. 4461-4669, 2003

[92] J. Bouchaud, “Ranking of top MEMS companies,” *MEMS Investor Journal*, 2007 at website: http://www.memsinvestorjournal.com/industry_trends/index.html

CHAPTER 3 Experimental Approaches

3.1 Thin Film Deposition

Techniques of sputtering or evaporation have been widely used to deposit metal and alloy thin films. However, controlling the alloy composition using evaporation deposition is difficult because the vapor pressure for different metals is fixed (so is the evaporation rate) when a single alloyed material container is used. Even if a separate co-evaporation system is used, it would be hard to control the composition uniformity across the substrate because of the straight line atom transport patterns during evaporation process [1]. In this study, precise composition control and high composition uniformity are both required. Therefore, instead of evaporation, co-sputtering technique is chosen to achieve these goals.

Pure Au and Au-Ni alloy (with up to 20 at. % Ni) bottom contacts samples were prepared using ion-beam sputter-deposition. Xenon gas was used in the ion source due to its relatively large mass, reducing energetic bombardment of the growing film. The base pressure was $< 3 \times 10^{-7}$ torr and the deposition pressure was 2×10^{-4} torr. The accelerating voltage for the beam is 600 V and beam current is 20 mA. The substrate is a silicon wafer coated with a 1000 Å thick thermal oxide. A 5 nm Chromium (Cr) layer and a 10 nm molybdenum (Mo) layer were deposited as an adhesion layer and a diffusion barrier layer, respectively. A 250 nm film of pure Au or Au-Ni (with various nickel composition) was then deposited.

The Au-Ni alloy was prepared by co-sputtering from a rotating gold target partially covered with a piece of the alloying metal (Ni). The atomic percentage then was determined by the fractional target area the nickel occupies (in percent area, or equivalently, the angle θ in comparison to 360^o) and its sputtering yield (Y) compared to that of gold. The required angle θ was calculated as follows:

$$At.\%\ A = \frac{Y_A \cdot \theta_A}{Y_A \cdot \theta_A + Y_B \cdot \theta_B}$$

$$\Rightarrow \quad \theta = \frac{360^\circ}{1 + \dfrac{1 - at.\% A}{at.\% A} \cdot \dfrac{Y_A}{Y_B}} \tag{1}$$

where A and B are the different materials. The sputtering yields of Au and Ni under Xe ion bombardment were taken from Ohring [2]. The *in-situ* rotation of the target ensures the uniformity of the film composition.

3.2 Contact Pattern Design and Processing

The deposited candidate alloy films are to be used as bottom contacts in our MEMS switching tests. In order to facilitate the in-situ contact resistance measurement, these alloy films need to be patterned on an insulating substrate. Figure 1 shows the four point probe measurement set-up. The basic test pattern includes two electrically-isolated symmetric metal-film pieces. Each metal film piece has two contact pads: one for a current-supply probe and the other for a voltage-sensing probe. Current is supplied from one probe to one metal-film piece, then flow up through one of gold micro-contacts to the upper MEMS cantilever (across the insulating gap by conducting through the cantilever), then, go down through the other gold micro-contact, back to the other metal-film piece. Finally, the current is collected by the other current-supply probe. As can be illustrated in figure 1, the two voltage-sensing probes sense the voltage drop between the two micro-contact sites. Thus, the resistance it measures includes the two contact resistances for the two pairs of micro-contacts and the bridge resistance of the MEMS cantilever.

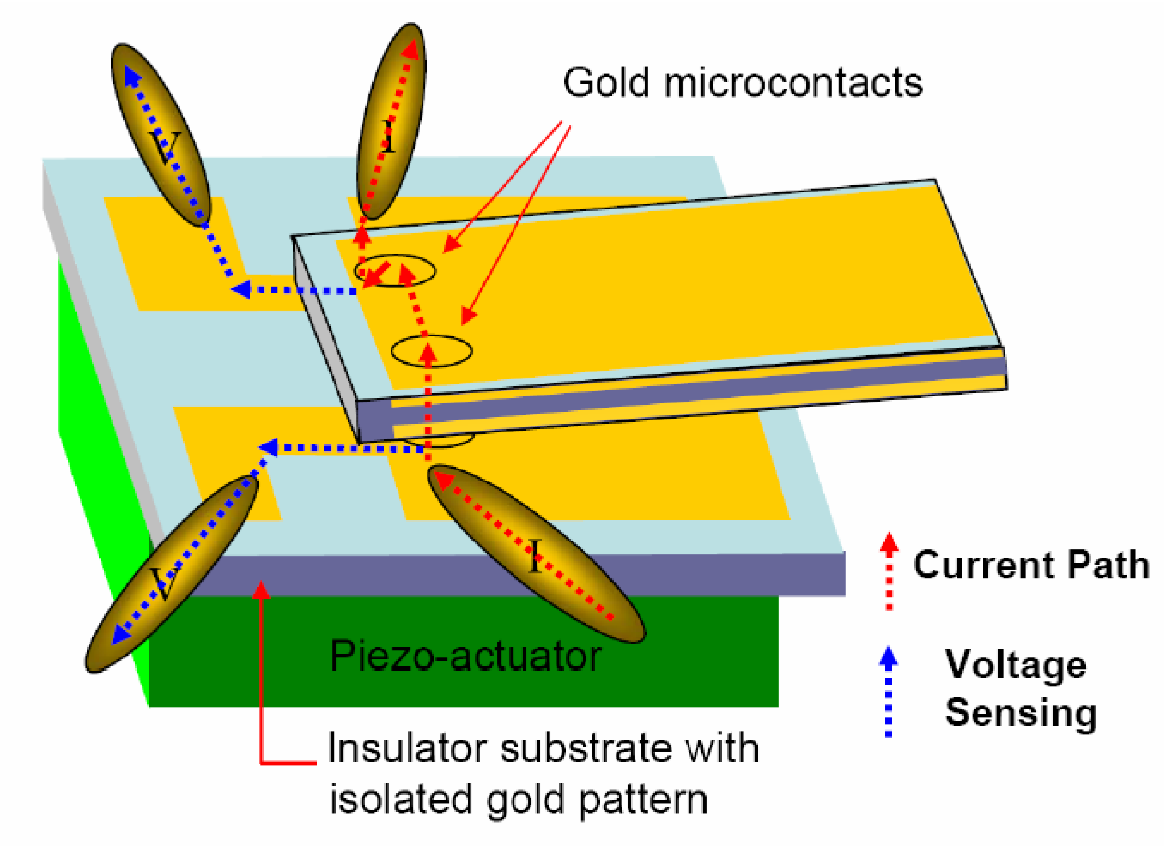

FIG. 1: Four-point probe set-up for *in-situ* contact resistance measurement

Only one mask is needed for this single metal layer patterning. Mask pattern is designed using AutoCAD software package. The films were patterned using standard photolithography tools. The operation procedures include spin-coating of photo-resistance (PR) film (spin speed at 4,000 rounds per minute; duration of 40 seconds), soft-baking of PR film (temperature of 115 ºC, duration of 60 seconds), UV exposure (duration of 10 seconds), Dissolution of exposed PR film using FM 319 (duration of 45 seconds), water rinsing and final hard-baking of PR film (temperature of 115 ºC, duration of 5 minutes).

Ion beam etching thereafter was used to remove metal films off the uncovered area. The etching species is Argon and background pressure was around ~ 5.5×10^{-4} torr. The beam voltage and current are kept around 800 volts and 10 mA respectively. It typically takes 20-25 minutes to etch through all the metal layers. Before starting an etching process, Argon gas flow was run through the vacuum system for at least 30 minutes to minimize the oxygen concentration in the chamber. Without this procedure, the Cr layer and Mo layer may be oxidized during the etching process and thus dramatically reduce the etch rate. The completion of etching is signaled by color change of the surface (shining yellow to shining silver to dark blue). And the electrical isolation between the two metal film pieces needs to be verified thereafter. Finally, N-methyl pyrrolidinone (NMP) solution and de-ionized water was used in sequence to dissolve the photo-resist layer and clean the sample, respectively.

The final patterns are checked by optical micro-scope to make sure that the contact areas are free of pin-holes and other deficiencies.

3.3 Characterization of Candidate Alloy Films

3.3.1 X-Ray Diffraction (XRD)

X-ray diffraction technique was extensively used to study the lattice parameters and microstructures of candidate alloy films. Based on the well-established data source, a detailed crystallography and compositional verification was also performed. A brief discussion of these measurements is presented below.

Crystals are regular arrays of atoms and the lattice parameters are usually a good identity of the material types. XRD technique allows the mean spacing distance between two atomic planes to be determined within a few thousandths of an Angstrom by Bragg's law:

$$2\mathrm{d}\sin\theta = \mathrm{n}\lambda \tag{2}$$

where d is the spacing distance between two parallel planes of atoms, θ is the X-ray incident angle with respected to the atomic planes and λ is wavelength of the X-ray. Knowing the unit cell structures, lattice parameters can then be derived from the distance between atomic planes d. For example, gold has a FCC structure. Then the lattice parameter a can be defined by Equation 3 in terms of the distance between atomic plans d and the related miller index (*h, k, l)*.

$$\mathrm{a} = \sqrt{\mathrm{h}^2 + \mathrm{k}^2 + \mathrm{l}^2} \cdot \mathrm{d} = \sqrt{3}\mathrm{d} \tag{3}$$

Therefore, presence of individual peaks of reflected x-ray intensity reveals information about element species and micro-structures of the examined samples. For example, only one set of peaks related to the single-phase solid solution structure should be observed in the XRD spectrum of an Au-Ni solid solution sample while two sets of peaks respectively related to gold-rich phase and nickel-rich phase should be identified in the spectrum of a two-phase Au-Ni sample. It should be noticed that the measured lattice parameters in an alloy material deviates from the single-element crystal due the lattice distortion caused by incorporation of foreign atoms. Fortunately, this type of data (composition vs. lattice parameters) has been widely studied and recorded for most binary or ternary alloy systems [3, 4]. By comparing our measured data with these well-calibrated data, chemical composition of the candidate alloy films can be verified.

3.3.2 Atomic Force Microscopy (AFM)

Previous studies have indicated that surface roughness should have an impact on the contact resistance of metal contact MEMS switches [5, 6, 7]. Additionally, Majumder *et al.* predicted a low contact resistance bound when using the multi-asperity model and an upper contact resistance bound when using the single effective a-spot model [8]. It indicates that rough surface may increase the contact resistance. Therefore, assessment of the contact surface roughness is necessary. In our study, surface roughness was characterized by an AFM (Thermo-microscope, Autoprobe VP2).

In our test, the size of the micro-contact is around 5 μm and the effective contact radius is estimated to be on the order of 100 nm. A scan size of 1 μm is chosen so that roughness can be accurately determined at the proper size scale. After a scan, RMS roughness data is directly determined using IP 2.0 data analysis software.

After each switching test, the contact area is also characterized by an AFM (Park Scientific Instruments, M5). AFM has the advantage of high z-axis resolution (a few angstroms) which helps to detect the smallest traces of surface modifications in the contact area. Combined with the use of scanning electron microscope (SEM), contact degradation features can be truly recorded. Additionally, by using advanced data-processing software package (etc. Gwyddion), material transfer /wear can be analyzed quantitatively.

3.3.3 Nano-indentation (Miro-hardness Measurement)

As has been discussed in section 2.4, micro-hardness of the contact surface is one of the important material properties that determine the contact resistance. In this study, micro-hardness data was obtained using a Hysitron Triboscope nano-indentor (Berkovich indenter tip-142.5° included angle). One hardness measurement is shown in Figure 2. Five indents were measured on each of the test specimens and the averaged value was then used in the contact resistance calculation.

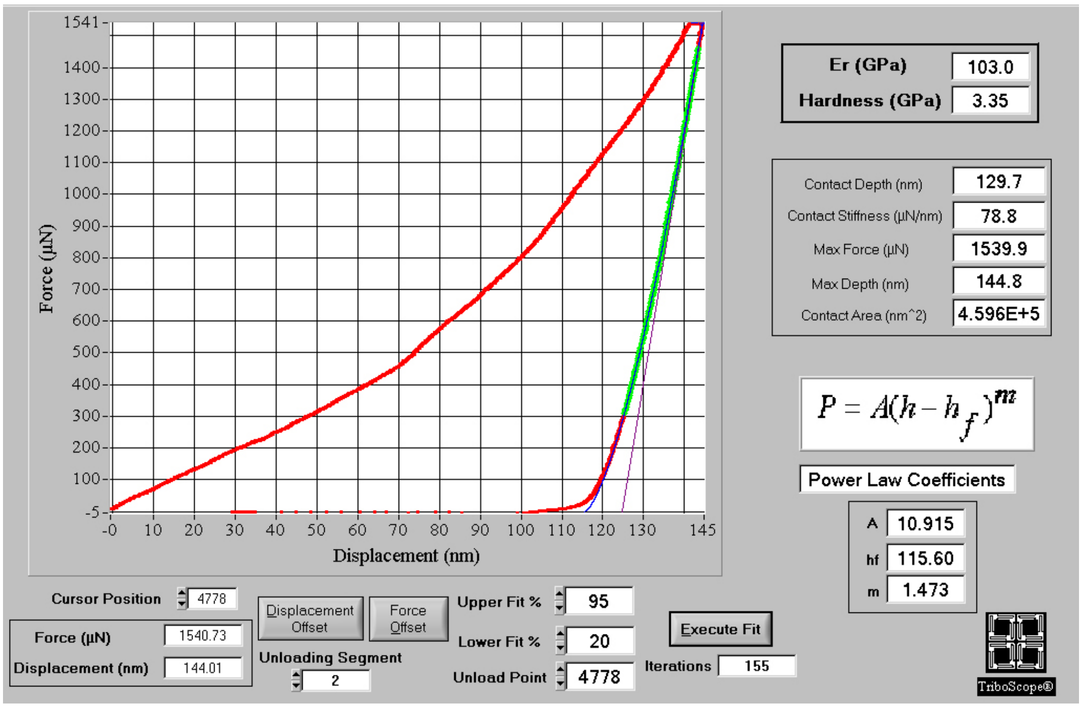

FIG. 2: An example of one micro-hardness measurement

3.4 Cantilever Transfer from wiSpry's MEMS Chips

Some convenient contact wear test facilities have been used to research the characteristics of microswitches. Notably, Hyman used a modified X-Y-Z micrometer station to investigate the contact physics and test current carrying capability of MEMS switches [9]. Schimkat used an accurate loading system to survey materials for micro-relay actuators [10]. A modified nano-indentor was also used to study hot-switching degradation of MEMS contacts [11]. One concern about these tests is that they do not closely mimic real microswitches. In particular, the tests have difficulty duplicating the switch geometry (mechanical moving parts are typically micro-scale cantilever structures with metal films being patterned on the surfaces) and the contact geometry (micro-contacts); these are important issues because the contact geometry has a strong influence on the stress and heat distribution across the contacts, and thus on the switch performance and failure mechanism [12, 13].

In our work, these issues were addressed by utilizing a newly developed switching degradation test facility closely mimicking actual MEMS switch operation. This new test facility is described in chapter IV. In the test, cantilevers with gold micro-contacts from commercial MEMS chips (from wiSpry Inc.) are used as the upper contacts; the patterned alloy thin films are used as the bottom contact. Both are incorporated into an AFM where dynamic MEMS switching tests are conducted. One of the difficult tasks is to make a usable upper contact. The procedures of cantilever transferring and gluing techniques are described in details in the following paragraphs. The whole process was first developed by Christian Nauenheim [14], and then modified by Zhenyin Yang (this author) to improve the transfer accuracy and the success rate.

Figure 3 shows a microscopic picture of the MEMS switch chip which has an array of ten switches mounted on the surface. The switches are made of a cantilever beam mounted on the chip which carries the bottom electrodes. The width of each cantilever is 75 μm and the length varies from 75 μm to 300 μm. The cantilever consists of three layers made of a 0.5 μm thick gold layer on a 2 μm thick SiO_2 layer which carries another 0.5 um thick gold layer on its underside. This structure gives the cantilever a temperature stable feature (prevents curvature). The dimension of the chip is about 1.2 mm · 1.2 mm · 0.5 mm.

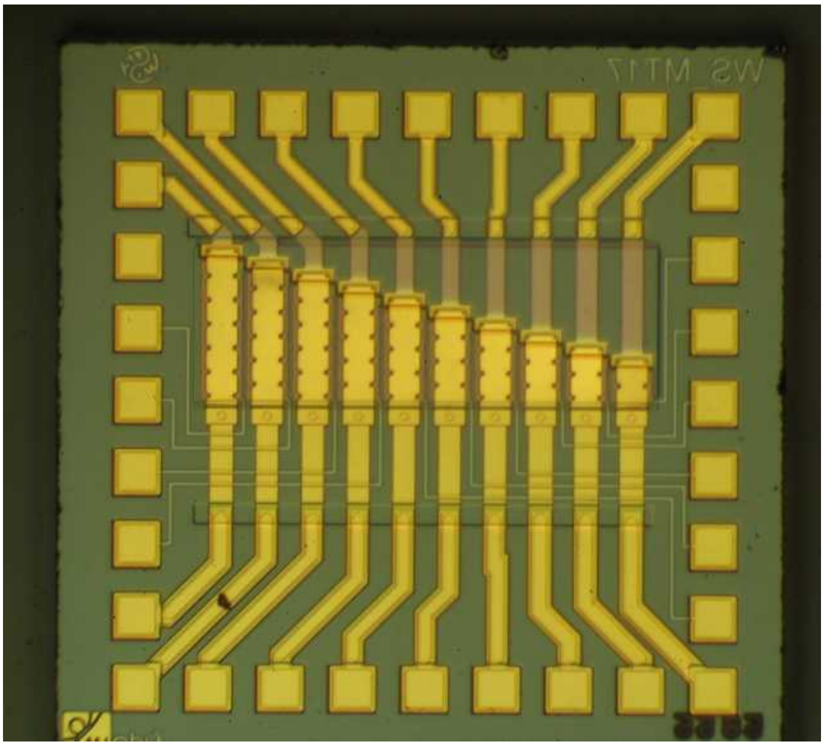

FIG. 3: A microscopic picture of the MEMS switch chip

To do the transfer, it is necessary to disassemble the top and the bottom electrode of the switch. This provides free access to the part of the device under investigation of failure. It also allows us to perform tests and detailed analyses of the contact area by advanced characterizations such as SEM and AFM. It also enables the test of our candidate alloys as contact materials.

Since the switching tests are designed to be conducted within an AFM, an AFM-tip is an ideal, rigid carrier for the MEMS cantilever. The dimension of an AFM-tip is about 1.2 mm · 1.2 mm · 0.5 mm. And the bottom surface of AFM-tips is perfectly flat. Therefore, MEMS cantilevers can be mounted without any vertical titling. In our experiments, used AFM-tips were cleaned and checked under microscope to make sure that all the cantilever probes have been broken off before they can be used as the carrier for MEMS cantilevers.

The transfer of the cantilever from the MEMS chip to the AFM carrier was performed at a Rucker & Kolls 260 probe station. This facility provides two movable XYZ 500 TRS micromanipulators from Quarter R&D on a magnetic stage and an optical microscope Leica StereoZoom 6 with a magnification of 30 × with zoom adjustment range of 0.67 × to 4.0 ×.

A two-component epoxy (with the set-time of 60 minutes) was used as the adhesive during the transfer. A form of stamp technology was adapted and used to apply and to structure the micro-meter scale adhesive layer [15]. Following procedures are used in order to achieve a micro-meter scale drop of epoxy: firstly, a regular sharp iron probe is handled using the micromanipulator to deposit a few dots of glue that should range from a large size to a small size. Then a tungsten probe with a tip radius of 25 μm was used to pick up a micro-drop on the tip through touching with the smallest glue drop. Because of the cohesion and adhesion, most epoxy micro-drops are not formed at the probe tip. Thus, it is difficult to transfer the drop to the cantilever with the probe tip. It has been experimentally determined that bending the probe could ease the drop-transfer.

In preparation of the transfer, the chip is fixed on a glass slide with double sided tape (shown in figure 4). A second chip of the same size is aligned behind the MEMS chip. It serves as a supporter for the far end of the AFM and holds it in a horizontal position because the carrier is much longer than the chip.

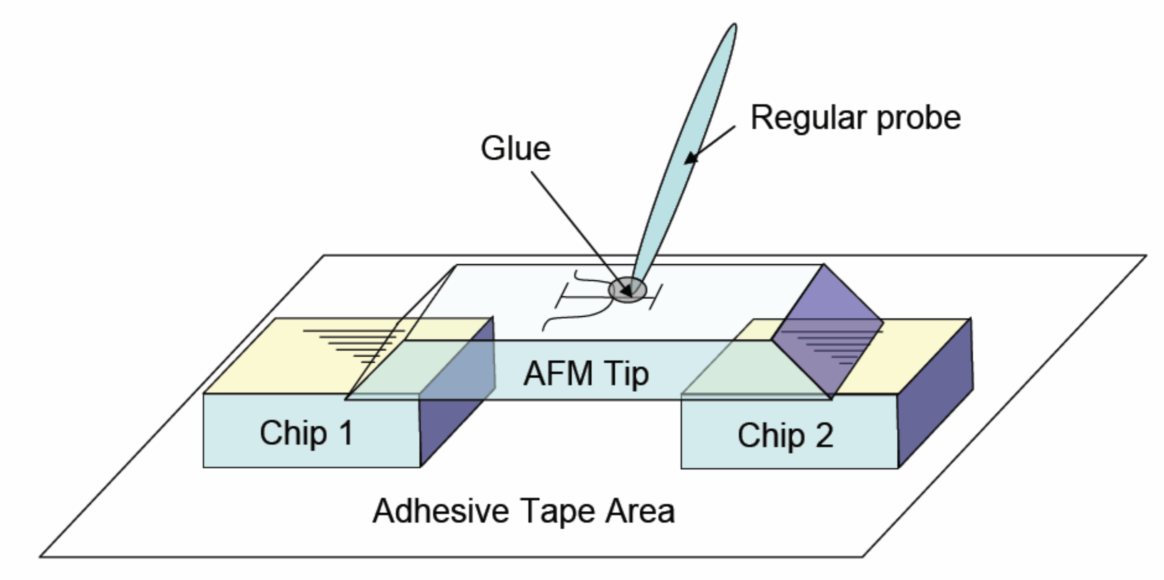

FIG. 4: Arrangement for lifting the AFM tip using a regular iron probe; the target switch chip on the left side of the picture.

The first step is the alignment of the AFM carrier. It is laid flat down using a pair of tweezers (shown in figure 4, the longer side is at the bottom). The regular probe, controlled by the micromanipulator now can help bring the carrier into the exact position by pushing the latter at the sides. This can be controlled visually through the microscope. Cares need to be taken to avoid laying the AFM tip directly on the MEMS cantilevers.

After that, a drop of glue is mixed on the glass slide. By dipping the regular probe into the adhesive, a small drop is formed at the tip which is then carefully brought on the carrier. The probe must be lowered carefully without tilting the aligned AFM tip carrier left or right. The position of the gluing area is also shown in figure 4.

After waiting for 30 minutes, the adhesive is strong enough to move the probe with the carrier which is now in the right position for the transfer. If the glue is not fully set, there is a risk of tilting the AFM tip during lift-up. Then, the carrier is lifted with the probe carefully and the micromanipulator then is shifted away from the operation area. Now, we can get free access to the cantilever surface to apply the glue.

Thereafter, another drop of epoxy is deposited on the glass slide by hand and a blunt probe probe. The diameter of it usually is on the order of millimeters. Then, a second micromanipulator is controlled to dip a second regular probe into the epoxy drop, so that much smaller drops can be produced on the glass slide. After that, this regular probe needs to be replaced by the special curved 25 μm tungsten probe. The tungsten probe then is dipped into the smallest epoxy drop. With slight disturbance, it should be able to easily pick up a micro-drop. After that, this tungsten probe is carefully placed on the surface of one MEMS cantilever and with a gentle touch of the surface an oval area of glue is applied with a dimension of about tens of μm in length (adjustable) and 40-60 μm in width. To cover the intended area, a couple of prints may be produced next to each other. If necessary, it is also possible to use the probe to spread the epoxy a little. This process is illustrated in figure 5. By adjusting the position of epoxy area, the free length of the MEMS cantilever is determined. In all our tests, the free length is fixed to be 150 μm to supply a contact force of ~ 150 μN/ contact (described in chapter IV). Now the tungsten probe has to be cleaned by acetone to avoid growth of tip radius. A small piece of tissue is soaked in acetone. Then the soft tungsten probe is rubbed against the soaked tissue all around the tip.

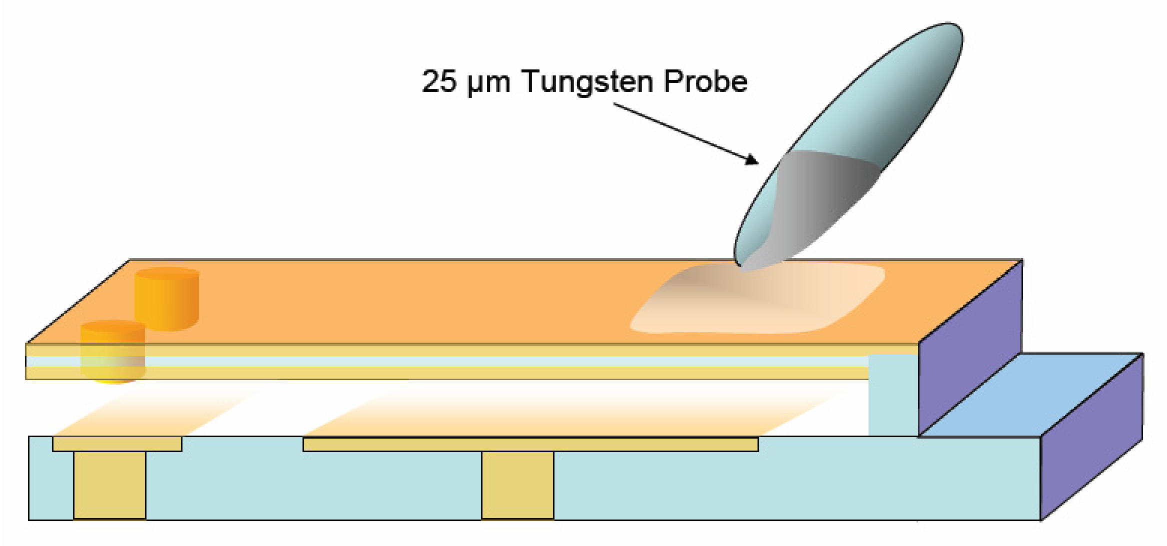

FIG. 5: Applying micro-drop of epoxy to the surface of MEMS cantilever.

Afterward, the 25 µm tungsten probe is replaced a regular probe again. This time, the sharp end of the probe is pointing down. It is lowered and positioned near the anchor of the MEMS switch. Make sure that further slight lowering of the probe forces the probe tip move from right side toward the anchor of the switch. It has been experimentally proved that poking in this way can reliably destroy the anchor without damaging the MEMS cantilever (shown in figure 6). As a result, the cantilever now is freely sitting on the substrate. But, this may cause some misalignment of the cantilever, which can be possibly adjusted by the push from the probe.

Next, the previously suspended AFM tip is positioned over the target cantilever. The front edge of the AFM tip should be aligned perpendicular to the MEMS cantilever and it also should just cover the epoxy area. Then carefully lower the AFM tip and keep adjusting its position so that the relative positions of these components still remain unchanged. The best focus and a slight spread of epoxy area could be observed when the bottom surface of the AFM tip gets in contact with the surface of the MEMS switches. After that, the AFM tip

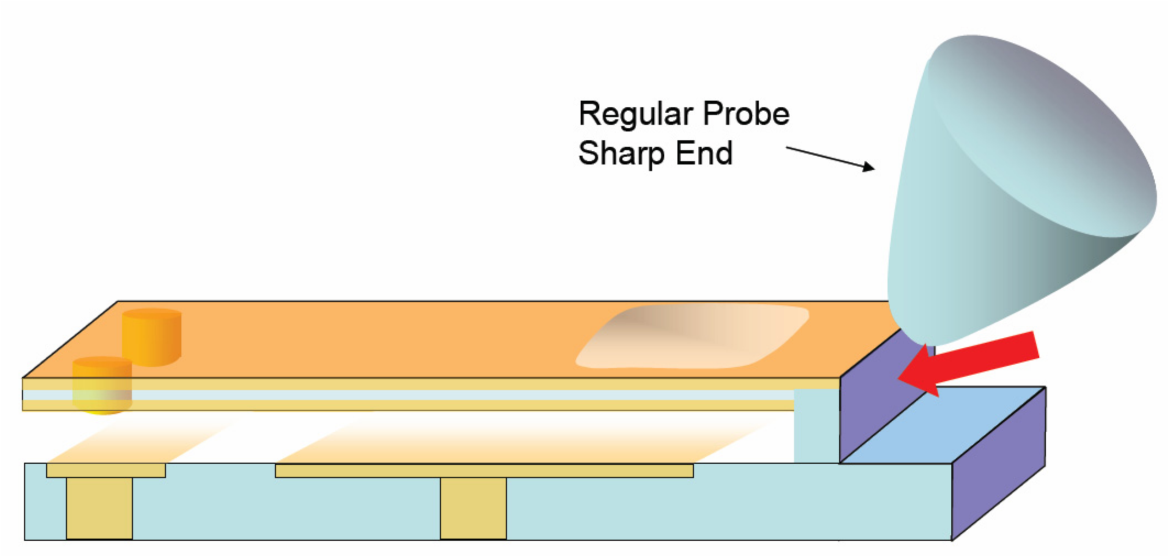

FIG. 6: Destroy the anchor of the MEMS switch using the sharp end of a regular probe.

can be slowly lifted up and the MEMS cantilever should already be attached with it. A pair of tweezers is used to release the AFM tip from the regular probe. After that, secure the AFM tip on a double-side tap and let the cantilever-side hanging over the edge. Then, a razor is used to clean the residual epoxy off the AFM tip.

Finally after turning it over, the cantilever should be in the same plane with the bottom surface of the AFM tip. This can be checked by reflection of light on both surfaces. The micro-size epoxy should be fully set after 24 hours. The whole transfer process is developed in our lab and still not a standard, highly reliable process. But according to the author's experience, the successful rate could be around 50 % with a good practice of several months. A transferred MEMS cantilever on an AFM tip is shown in figure 7. This AFM tip with the MEM cantilever can be easily incorporated into an AFM and serves as the upper micro-contacts in our switching tests.

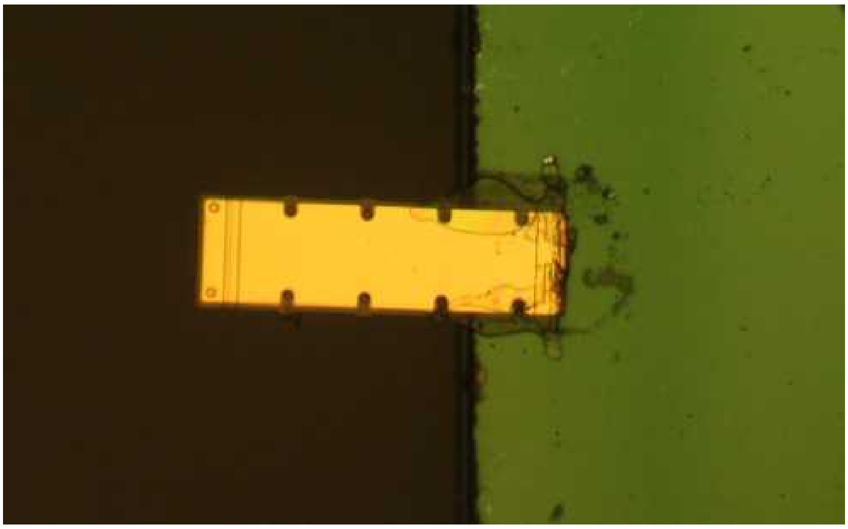

FIG. 7: A transferred MEMS cantilever on an AFM tip.

3.5 MEMS Switching Test Set-up

Since the switching set-up has been covered in chapter IV in details, only instructions on equipments and experimental procedures are presented in this section. The whole test system is composed of several functional sub-systems which include: the AFM and related control modules (Park Scientific Instruments, M5), *In-situ* micro-scale visual monitoring system, MEMS switching stage, piezo-actuator (PI, P-802.00) and its driving signal (Agilent function generator 33120A) & amplifier system (High voltage amplifier, MATSUADA, Precision, Inc), PC controlled *in-situ* four-point probe resistance-measurement system (Agilent 34401A Multi-meter and software pakages) and Oscilloscope for transient measurement. To assembly and operate the system correctly, a set of procedures needs to be followed in sequences.

Firstly, the patterned alloy sample needs to be installed onto the MEMS switching stage and secured by the four metal probes. Each probe should be pressed on specific contact pad on the sample to facilitate the four-point probe measurement (shown in figure 1). Then this stage needs to be tested by the multi-meter to make sure the two pieces of ally patterns are electrically isolated (resistance needs to be at least larger than a few hundred KΩ).

Secondly, this switching stage needs to be screwed into the XY-movable sample stage of the AFM. The switching stage is well aligned with the AFM head when screwed tight. Then according to specific experimental circuit configuration, a serial resistance (for transient current measurement) or a parallel resistance (to limit the open circuit voltage) could be connected. At the same time, electrical connections for the four-point probe needs to made. Oscilloscope should be connected if necessary. Basically, the whole test circuit should be completed at this point. Also, two wires of the piezo-actuator need to be secured on the AFM stage.

Thirdly, a new MEMS cantilever (on an AFM tip) is inserted into the AFM head, which then is installed onto the AFM. Then, the AFM sample stage is moved under the head. Now, the driving signal & amplifier system for the piezo-actuator need to be tested and connected but the amplifier still needs to be power-off. After that, *in-situ* contact resistance monitoring software (Excel Intuilink for Multimeters) needs to be started with a sampling interval of 2 seconds.

Fourthly, the MEMS cantilever is lowered by bringing down the AFM head. Cares needs to taken to avoid crashing the cantilever (close visual monitor of the focus change of the bottom pattern should be helpful). Fine adjustment of the AFM sample stage is usually necessary in order to accurately position the two micro-contacts onto the intended contact areas. Preferred contact areas are located on the two corners of each individual metal pattern. Edge touch point can be identified when slight deflection of the MEMS cantilever is observed. The corresponded z-axis value needs to be recorded. Further lowering the cantilever could bring the two upper gold micro-contacts into contact with the two bottom pads. And this is signaled by the sudden drop of the contact resistance shown in Excel Intuilink software.

Finally, switch the cantilever up and down a few times and make sure the switching position does not deviate with cycles. Then choose the middle position point as the dynamic switching point. Then, switch on the amplifier and ramp up the actuation voltage to 30 volts. The sampling frequency needs to be changed to 0.4 second if the switching frequency is 1 Hz. Now the contact resistance evolution should be observed. The number cycles before failure for each test is normally taken out from the first a few good runs in the whole evolution spectrum.

These procedures also apply to our field evaporation experiments and cold switching tests although small modification may be necessary in those cases.

3.6 References

[1] R. F. Bunshah *et al*. *Deposition Technologies for films and coatings: developments and applications*, New Jersey: Noyes Publications, 1982

[2] M. Ohring, *Material sciences of thin films*, Academic Press, 2002, p. 176

[3] H. Okamoto and T. B. Massalski, *Phase diagrams of binary gold alloys,* Ohio: ASM international, 1987, p. 196.

[4] W. B. Pearson, *A handbook of lattice spacings and structures of metals and alloys,* New York: Pergamon Press, 1964

[5] J. A. Greenwood and J. B. P. William, "Contact of nominally flat surfaces," *Proc. R. Soc. London A,* 295: pp. 300-319, 1966

[6] J. Larsson, S. Biwa and B. Storakers, "Inelastic flattening of rough surfaces," *Mech. Matter.*, 31: pp. 29-41, 1999

[7] O. Rezvanian, M. A. Zikry, C. Brown and J. Krim, "Surface roughness, asperity contact and gold RF MEMS switch behavior," *J. Micromech. Microeng.* 17: pp. 2006-2015, 2007

[8] S. Majumder et al. "Study of contacts in an electrostatically actuated microswitch," Sens. Act. A., 93 (1): pp. 19-26, 2001

[9] D. Hyman and M. Mehregany, " Contact physics of gold microcontacts for MEMS switches," *IEEE Trans. Comp. Packag. Tech.,* vol. 22, pp 357-364, 1999.

[10] J. Schimkat, " Contact materials for microrelays," in *11th Proc. MEMS' 98 Workshop,* 1998, pp. 190-194.

[11] D. J. Dickel and M. T. Dugger, "The effect of surface contamination on

resistance degradation of hot-switched low-force MEMS electrical contacts," in *Proc. 51st IEEE Holm Conf. Electric Contacts,* 2005, pp 255-258.

[12] L. Chen, "Contact evolution in micromechanical switches," in *World Tribology Congress,* Washington D. C., U.S.A. 2005.

[13] X. Yan, N. E. McGruer, G. G. Adams and S. Majumder, " Finite element analysis of the thermal characteristics of MEMS switches," in *12th Int. Conf. Transducers, Solid-State Sensors, Actuator and Microsystems,* 1, pp 412-415, 2003

[14] C. Nauenheim, Internship Report: *Design and construction of a test facility for RF-MEMS switches*, wiSpry Inc., 2004

[15] F. Sarvar, D. A. Hutt, D. C. Whalley, "Application of adhesives in MEMS and MOEMS assembly: a review, polymers and adhesives in microelectronics and photonics," *Polytronic 2002, 2nd International IEEE Conference,* pp. 22-28, 2002

CHAPTER 4

A New Test Facility for Efficient Evaluation of MEMS Contact Materials

(This chapter has been published on Journal of Micromechanics and Microengineering)

4.1 Abstract

A novel test facility for the efficient evaluation of microelectromechanical system (MEMS) switches and the development of alternative contact materials is described. The facility utilizes the upper cantilever from commercial MEMS contact switches, and tests these against alternative bottom contact materials within a modified AFM. The test closely approximates the real switch, but can accommodate a wider range of test conditions and contact materials. The facility allows alternative contact materials to be easily and quickly incorporated, and therefore evaluated by measuring the number of cycles to failure. The evolution of the wear surfaces of the switch contact materials under test can also be easily examined. In order to demonstrate the facility, the evolution of the contact resistance and wear of a commercial RF MEMS cantilever with Au contacts was monitored under accelerated test conditions, comparing the behavior of Au bottom contacts to an alternative Au-Ni alloy contact material. The Au-Ni (20 at. %) alloy displayed reduced wear rates and improved switch cycle lifetimes compared to pure Au, while retaining acceptable values of contact resistance.

4.2 Introduction

Since the first MEMS switch, which was specially designed for microwave applications in the early 1990's [1], this technology has developed to the point that the devices are currently in small-scale production. Typical MEMS switches are micron-scale switching devices. Because of their low fabrication cost, low power consumption, wide operational band and exceptional switching performance, MEMS switching technology holds great promise for implementing agile radio frequency (RF) systems. Generally, MEMS switches can be categorized into non-contact type (capacitive) and contact type (metal contacts). Figure 1 shows the cross-section of a metal contact-type MEMS switch [2]. The switch is driven to closure with an electrostatic force by applying a voltage across parallel electrodes located on the cantilever and bottom electrode. This study utilizes this type of MEMS cantilever.

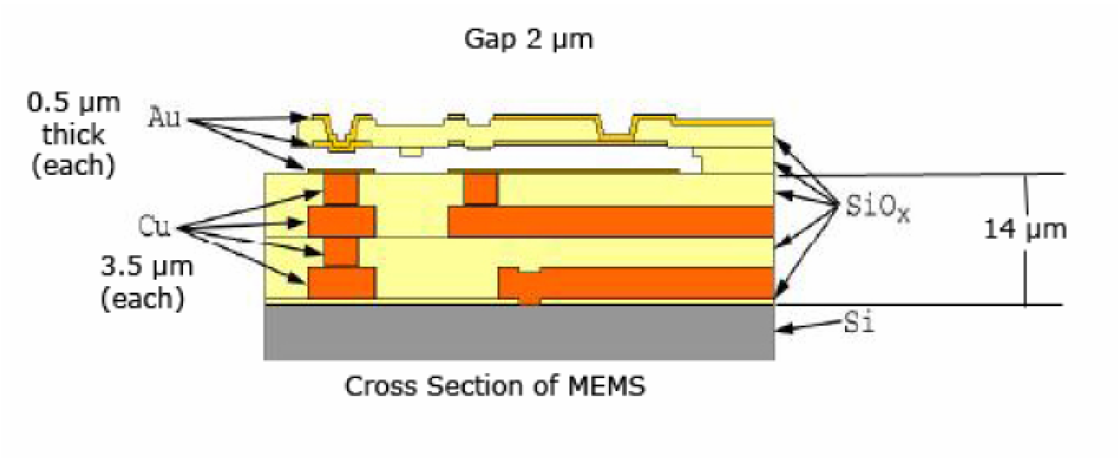

FIG. 1: Schematic of the cross-section of a contact-type MEMS switch [2].

Gold is often utilized as a contact material for metal-contact MEMS switches due to its excellent electrical conductivity and corrosion resistance. Gold-contact switches have been shown to achieve $>10^9$ switching cycles under favorable operating conditions (e.g. low current, optimum contact force, dry nitrogen environment, and 'cold switching') [2, 3]. 'Cold switching' refers to switch operation under conditions in which there is no field across the contacts as the switch opens or closes. However, there is a strong desire to significantly broaden the range of conditions under which a given switch would operate, including the range of currents (i.e. power handling). However, as operational conditions become more severe in mechanical force or electrical power handling, Au contact degradation increases, drastically shortening the MEMS switch lifetime. One approach towards increasing MEMS switch robustness is to investigate alternative contact materials, and a few have been investigated [4-7]. However, there are some serious impediments to the broad investigation of alternative contact materials. In general, convenient contact wear test facilities do not closely mimic real contact switches. In particular, the tests have difficulty duplicating the switch geometry, the contact geometry, and the contact force. Contact geometry has a strong influence on the heat distribution across the contacts, and thus the switch performance and failure mechanism [8, 9]. One clear alternative is to test candidate materials on actual MEMS switches, and such studies have been reported by researchers from universities and industry [3, 5, 6, 10]. However, the approach has a serious difficulty: the switches are fabricated in Si foundries, and only a limited range of materials may enter the fabrication facility. Secondly, the fabrication process must be optimized for each material, and it may take many months to fabricate a set of switches to test a single candidate contact material. Materials compatibility and process integration issues must be addressed in advance for every material to be tested. These factors have severely limited the range of contact materials that have been investigated for MEMS switches.

If progress is to occur, the testing and development of alternative contact materials must be more efficient while remaining representative of the typical device operation. In this manner the material comparison and failure analysis data can be collected consistently and efficiently. In our experimental set-up, to address these two issues, the switching lifetime test is performed with an actual cantilever (including upper contacts) extracted from a commercial RF MEMS switch (as shown in figure 1) that is contacted against a vibrating thin film bottom electrode containing the bottom contacts. This design enables the dynamic switching test to be performed under realistic conditions (e.g. contact force, contact geometry and switch geometry) comparable to those in actual devices. The bottom electrodes are separately fabricated from candidate contact materials and can be easily loaded into, and un-loaded from, the test system. In this way, the test and development efficiency is dramatically improved.

In this initial paper we have selected one material for comparison with gold in order to demonstrate the new facility. Given that the 'softness' of gold under both normal and aggressive operating conditions is considered to be a limitation to the contact lifetime, we have selected a set of Au-Ni alloys for study. The results for the Au-Ni (20 at. % Ni) alloy will be reported here. The full results for the alloy system are reported elsewhere [17].

4.3 Experiments

We have designed a unique setup for monitoring MEMS switching behavior by integrating a MEMS cantilever with separate thin film bottom contact materials into an atomic force microscope (AFM). The test configuration is shown in figure 2. The cantilever is first dismounted from an array of the RF MEMS switches chip, then transferred to a clean AFM tip carrier.

The transfer of the cantilever from the MEMS chip to the AFM carrier is performed at a Rucker & Rolls 260 probe station. In preparation for the transfer, two identical MEMS chips are fixed on a glass slide next to each other. A clean AFM tip carrier is then mounted and evenly supported by the two MEMS chips. An xyz-axis movable XYZ 500 TRS micromanipulator with a probe is first used to apply glue to the surface of the AFM tip carrier, with the probe temporarily attached to the AFM tip carrier to facilitate its positioning. Thereafter, another micromanipulator with a micro-probe (tip diameter = 25 μm) is used to apply an extremely small portion of glue to the MEMS cantilever's surface. The AFM tip carrier is then aligned and lowered to make contact with the MEMS cantilever on the glue area. The transfer is achieved when the AFM tip carrier is lifted again after a 24 hour cure. A typical AFM carrier with a MEMS cantilever attached is shown in figure 3.

The tip carrier is next inserted into the carrier-hold of the AFM and lowered by means of the z-direction positioning motor. The initial contact occurs between a slight insulating lip at the edge of the cantilever, and the bottom sample (the lower electrode structure). The initial contact is monitored with an optical microscope, and the position of the carrier then is recorded. The carrier is further lowered until the two gold upper micro-contacts make electrical contact with the patterned bottom contacts, as monitored through the electrical circuit across the bottom contacts. When the upper and lower electrodes are properly in contact, the deflection of the cantilever ensures that these are the only contact points (the lift of the insulating lip can be observed through the *in-situ* optical microscope). The position of the cantilever is again recorded. From the two positions of the carrier, the total deflection of the cantilever is known (~ 20 μm), and the contact force can be approximated using the known geometry and the material properties.

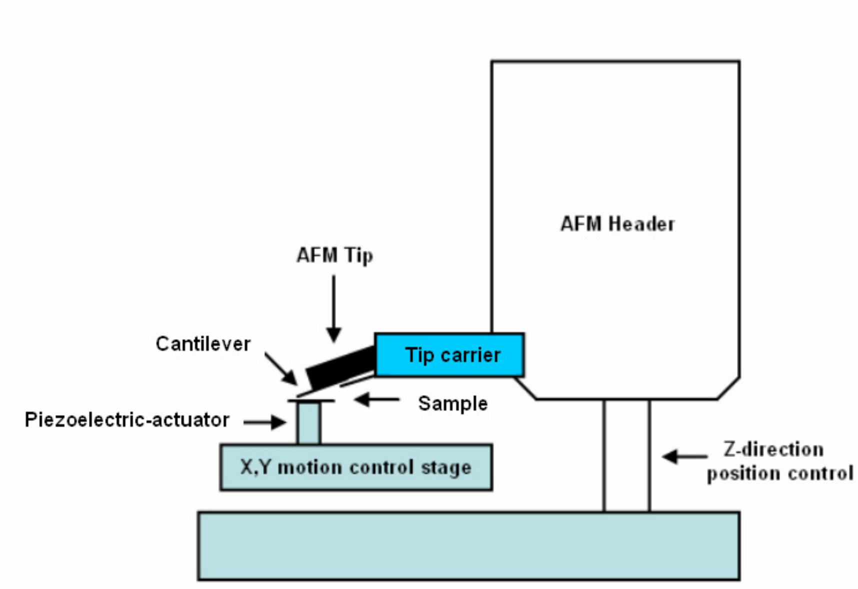

FIG. 2: Configuration for the switching tests.

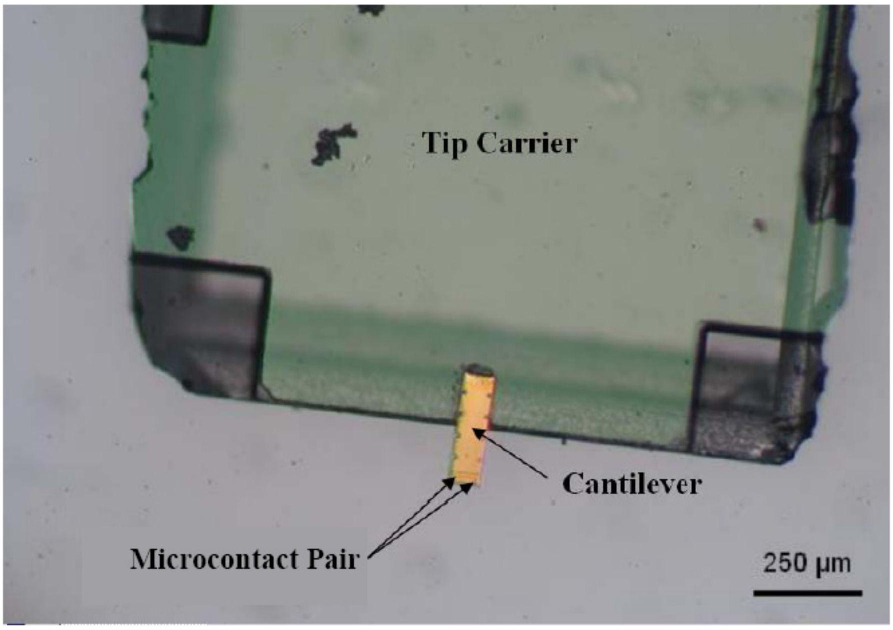

FIG. 3: Optical microscope image showing the MEMS cantilever attached to an AFM tip carrier. The normal AFM tip has been removed. The two micro-contacts are at the end of the cantilever.

A detailed view of the contact configuration is shown in figure 4. As is shown in figure 4(a), the cantilever is composed of 3 layers: a 2 µm SiO_2 layer with 0.5 µm gold layers on both sides. The width of the cantilever is 75 µm. The effective length of the cantilever can be adjusted while attaching it to the cantilever carrier. For the tests reported here, the effective length was fixed at 150 µm. There are two electrically connected micro-contact bumps on each cantilever (top contacts). The diameter of each contact is 5 µm. The bottom contact is patterned with the thin films of candidate materials deposited on oxidized Si (001), with the pattern shown schematically in figure 4(b). Details of the fabrication of the bottom electrode structure are discussed later in this experimental section.

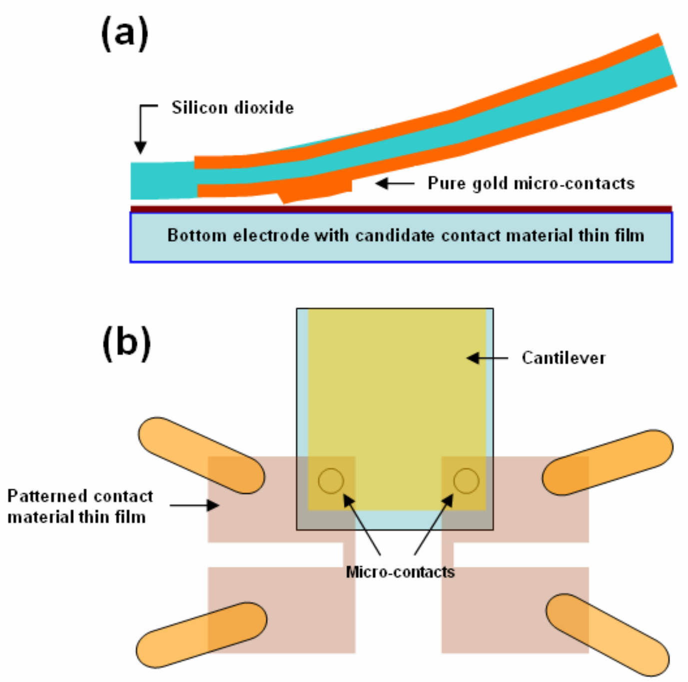

FIG. 4: Schematic view of the contact configuration. *(a)* Cross sectional view of the upper cantilever and bottom electrode. *(b)* Top view of the top and bottom contact configuration and the four point probe set up.

While the upper micro-contacts make electric contact with the bottom sample contact pad area, the contact resistance is measured by a four point probe set-up (figure 4(b)). From the figure, the top two probes supply 1 mA current, while the bottom two probes sense the voltage. The resistance from the four point probe measurement consists of the contact resistance of the two pairs of micro-contacts and the resistance of the metal connection on the cantilever. To obtain contact resistance for a single pair of micro-contacts, we deduct the metal connection resistance (~0.2 Ω) and divide the remaining resistance by 2. A piezoelectric actuator (Physik Instrumente, P-802.00) is used to vibrate the patterned bottom contacts vertically an amplitude of 1.8 μm, which is sufficient to bring the upper micro-contacts and bottom contact pads into and out of contact. This vertical vibration does not change the cantilever's deflection status (~ 20 μm deflection) significantly. It only switches the contacting points of the top cantilever between the insulating SiO_2 tip and the two upper micro-contacts. It also results in the upper micro-contacts being slightly tilted with respect to the plane of the bottom electrodes when contact is first initiated (in the test device, this angle is about ~ 2.5° and it is constant for every test). When contact is made between the upper micro-contacts and the bottom sample, 1 mA current flows through the two contacts, and the contact resistance is measured by the four point probe set-up. When contact is made between the insulating tip and the bottom sample, no current flows through the upper micro-contacts. The insulating tip assures a clear "off" state where the electrical contact is broken between the micro-contacts and the bottom electrode.

The drive signal for the actuator and the voltage drop across the micro-contacts are both input into an oscilloscope so that the dynamic contact process is monitored *in-situ*. The sample is cycled until a contact resistance failure occurs. The failure criterion that is utilized is a factor 2 increase in the measured contact resistance, although a rapid increase to a much higher resistance is normally observed. Thereafter, the worn contacts are examined by AFM and SEM. Typical resistance switching data is shown in figure 5 for low frequency switching (0.5 Hz) with the open state resistance (~1150 Ohms) set by a test system parallel resistor. This resistor also determines the open circuit voltage. With sufficiently high open circuit voltage, additional material damage may be induced by possible arc energy dissipation or transient current heating other than mechanical wear. In order to address this acceleration factor, both hot switching and cold switching test conditions were investigated in the switching test for pure gold. Quantitative volume change analysis (using Gwyddion software) was conducted to evaluate this effect.

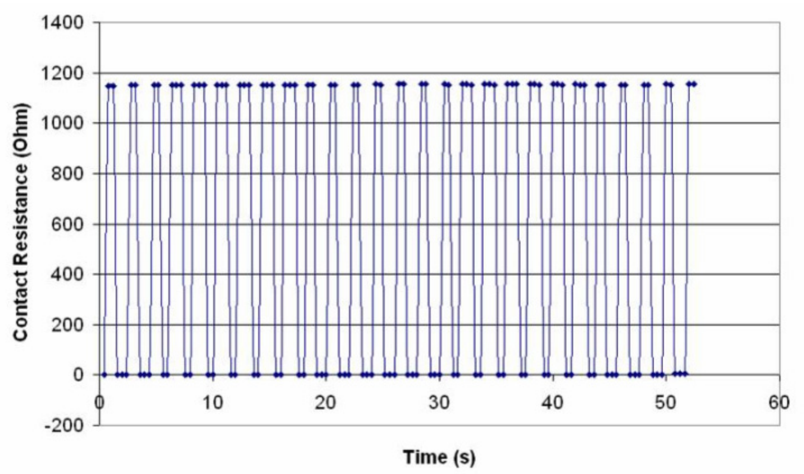

FIG. 5: An example of low frequency dynamic switching resistance response.

Pure Au and Au-Ni (20 at.% Ni) bottom contact samples were prepared using ion-beam sputter-deposition. The substrate utilized was typically a Si(001) wafer coated with 1000 Å silicon dioxide (thermal oxide). Xenon was used as the working gas due to its relatively large mass number, thus lower reflective ion energy bombarding the film during growth. The base pressure was 3 x 10^{-7} torr, and the deposition pressure was 4 x 10^{-4} torr. A 5 nm Cr layer and 10 nm Mo layer were deposited as adhesion and diffusion barrier layers, respectively. 250 nm Au or Au-20% Ni thin films then were deposited. The acceleration voltage for the ion beam was 600 V. The chamber was designed to allow the three metal layers to be deposited *in-situ.* Rotation of the target throughout the deposition ensured uniformity of the composition for gold alloy depositions. The as-deposited thin film samples were patterned using photolithography and ion etching, to facilitate *in-situ* four point probe measurement of the contact resistance in the lifetime tests.

Electrical resistivity data were obtained on as-deposited thin films (before patterning) using a four point probe technique (MAGNE-TRON Model-700). A four-point sheet resistance correction [16] was applied. Micro-hardness data was obtained using a Hysitron Triboscope nano-indentor (Berkovich indenter tip with 142.5° included angle).

4.4 Effect of material properties on contact resistance

Pure Au as a contact material has the advantage of achieving very low resistance in the closed state, due to its low resistivity and softness. With the use of alternate contact materials, closed-state resistance is expected to increase, depending on the material's resistivity and hardness. This section compares the measured material-dependent closed-state resistance to that expected from a simple theoretical model.

Knowing the dimensions of the MEMS cantilever, its Young's modulus (93.3 GPa) [11], and the deflection distance, the total contact force can be approximated using a cantilever beam model [12]. The model is described by:

$$F = [\frac{E \cdot w \cdot t^3}{4 \cdot l^3}] \cdot d \tag{1}$$

where E is the cantilever's Young's modulus, w is the width, t is the thickness, l is the length and d is the deflection distance of the cantilever beam. For a 150 μm long cantilever, the deflection distance is close to 20 μm in our case. The total contact force then is calculated to be ~ 300 μN, which is 2-3 times higher than the contact force of typical MEMS switches.

A simple model has been tested to predict the contact resistance for the two contact materials. The relationship correlating contact resistance to the contact force has been developed by previous researchers for gold-contact MEMS switches [9, 13, 14]. For a contact radius greater than the electron mean free path, the Maxwell spreading resistance model can be used to calculate the contact resistance. In our test, the nominal contact radius is much larger than the mean free path in gold (~ 36 nm). The contact resistance R_c is described by:

$$R_c = \frac{\rho}{2r_c}, \tag{2}$$

where ρ is the resistivity, r_c is the contact radius [15]. While two different materials are in contact, the resistivity is estimated as the average of the two. The contact radius can be obtained using an asperity deformation model [14]:

$$r_c = \sqrt{\frac{F}{\xi \pi H}}\,, \qquad (3)$$

where F is the applied force, H is the hardness of the material, and ξ is the coefficient of the material deformation mode. Different modes are given as: $\xi < 0.3$, elastic deformation; $0.3 < \xi < 0.75$, elastoplastic deformation; and $0.75 < \xi < 1$, plastic deformation.

For the contact between different materials, which is the case in our experiments, the averaged electrical resistivity and hardness value are used for the calculation. Plastic deformation is also assumed ($\xi = 1$) based on the relatively large contact force.

The measured electrical resistivity, micro-hardness, and contact resistance, along with the calculated contact resistance between upper pure gold micro-contacts and either the pure gold or gold nickel bottom contacts are shown in table 1. For the pure gold, the experimental data fits the calculated contact resistance data well. However, for the gold nickel case, the measured contact resistance is higher than the calculated value. It should be noted that the roughness of the Au-Ni alloy as measured by AFM is greater than that of the Au. Roughness is not taken into account in the above simple model, but should increase the contact resistance by decreasing the contact area. These results point to the need for a more sophisticated model for the relationship between contact material properties and the contact resistance. The effect of topography on contact resistance will be discussed in a separate paper [17], and a more complete multiscale model has been developed [18].

Table 1: Properties of Au and Au-Ni samples

Nickel Composition (at. %)	Electrical Resistivity (μΩ.cm)	Micro-Hardness (GPa)	Calculated Resistance (Ω)	Measured Resistance (Ω)
0	3.8	2.7	0.14	0.16 ~ 0.2
20.0	20.5	6.1	0.6	0.9 ~ 1

4.5 A unique electrical failure (contact degradation) detection mechanism

In order to evaluate contact performance of candidate materials in our test system, we chose the "cycle number to electrical failure" as the indicator of the degree of micro-contact damage. Since the damage is accelerated by a relatively large contact force under hot switching conditions, and the wear to failure is very small (determined by the wear required to produce contact only between the bottom electrode and the cantilever tip), such tests can be termed an "accelerated lifetime test". During the test, the open circuit voltage is fixed at ~ 1 V, measurement current is 1 mA, and total contact force is ~ 300 μN. Figure 6 shows switching tests for sputtered pure gold bottom electrodes against the upper gold micro-contacts. Figure 6(a) shows accelerated test data for the switch in this test facility under hot switching, in comparison with resistance data for a similar switch in the actual MEMS switch product configuration (figure 6(b)) subjected to purely cold switching [11]. In both cases the usual three resistance regimes can be observed. The initial contact resistance falls during the 'burn-in' period, which may be as short as a few cycles. The switch then appears to operate in steady state, prior to onset of instability and resistance increase that corresponds to contact degradation.

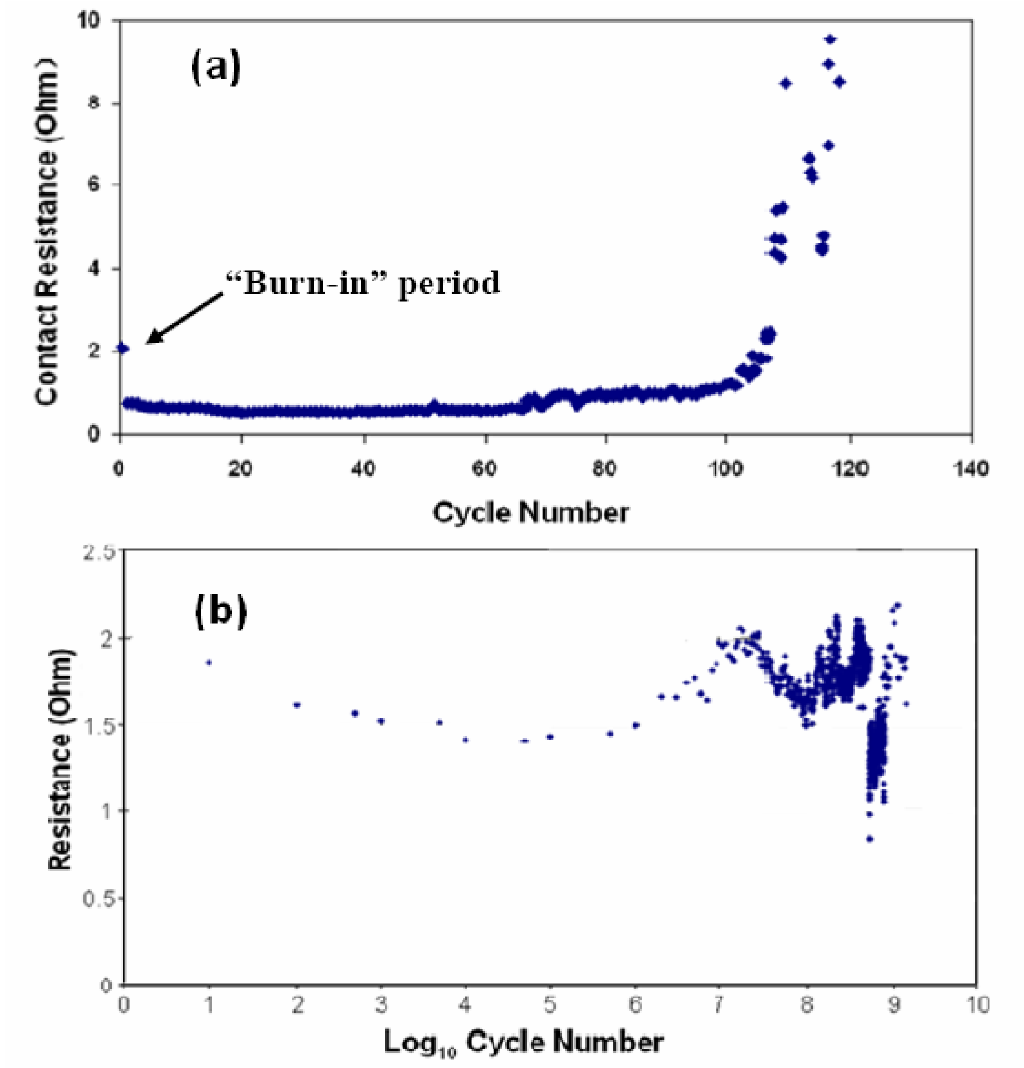

FIG. 6: *(a)* Contact resistance evolution for sputtered gold against gold micro-contacts in the present test facility under accelerated conditions. *(b)* Lifetime test of a similar switch under (moderate) normal service conditions (number of switch cycles plotted on a log scale) [11].

The marked reduction in the number of cycles to failure can be observed in the accelerated test in the new test facility. After only ~ 100 cycles, the closed contact resistance started to rise and reached an open-circuit condition. The same test was repeated using different pure gold samples with new MEMS cantilevers. The results are reproducible, with the variation of the number of cycles to failure being less than ~ 50 %.

The AFM analysis of the corresponding failed upper micro-contact is shown in figure 7. The sliding tracks visible in the images existed prior to testing. The switching wear damage is visible at the front edge of the micro-contact (near the top of images (a) and (b)), which corresponds to the region of contact or impact between the micro-contact on the cantilever and the lower electrode. Particularly revealing are the two line profiles taken across the micro-contact. Figure 7(c) shows the height profile of the ‘X’ scan taken across the contact along the cantilever width, showing no wear. In comparison, the ‘Y’ line scan of figure 7(d) runs parallel to the cantilever direction and includes the impact area. It can clearly be seen that the contact is eroded in the impact region nearest the cantilever tip, with material having been transported away from the impact region.

The corresponding AFM images of the pure gold bottom contact area after the failure test are shown in figure 8. A small crater or depression approximately 30 nm in depth and ~2 μm in diameter was formed during the switch cycling. Furthermore, there is a buildup of material around this crater.

As is mentioned in the experimental section, the upper cantilever remains bent with almost unchanged curvature during switching to exert constant contact force. The vibration of the bottom electrode by the piezoelectric actuator alternates the cantilever contact spots between the insulating lip and bottom electrode (open), and the micro-contacts and bottom electrode (closed).

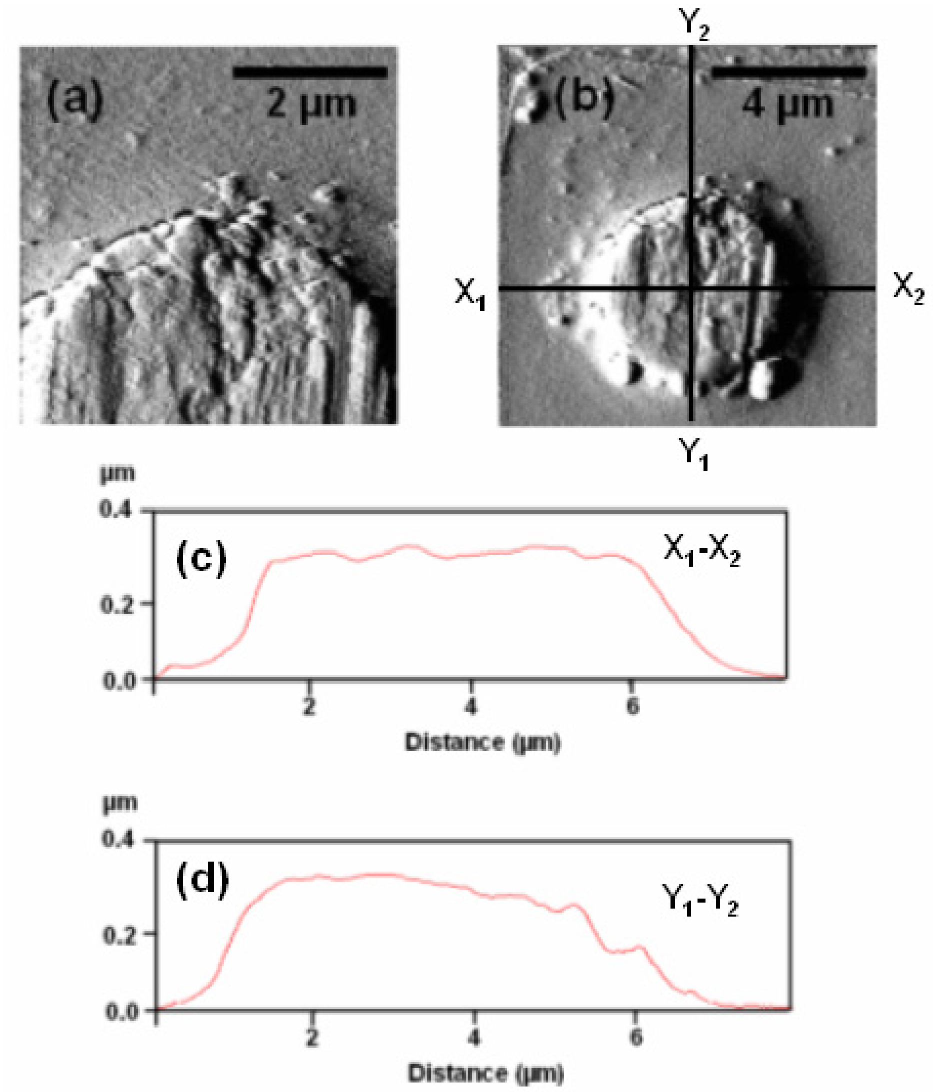

FIG. 7: AFM analysis of upper gold micro-contacts after switching failure (the bottom electrode was pure gold). *(a)* The damaged area of a micro-contact. *(b)* The whole micro-contact. *(c)*, *(d)* Height profiles corresponding to X_1-X_2 and Y_1-Y_2.

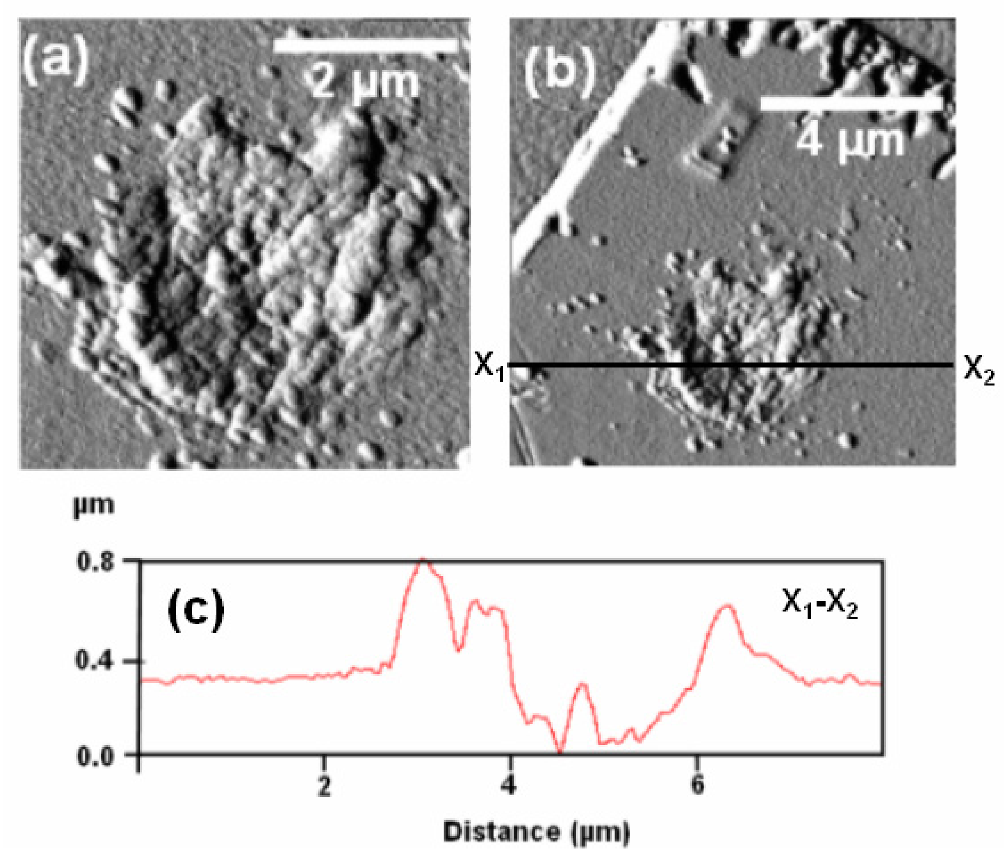

FIG. 8: Atomic Force Microscope images of the pure Au bottom electrode after failure (1mA). *(a), (b)* The damaged bottom contact area. *(c)* The height profile corresponding to X_1-X_2.

As a result of the slightly tilted micro-contacts (~2.5°), the contact area (or damaged area) is always located at the front edge of the micro-contacts. Upon closure, all the contact force is exerted on that small area. Possible transient current heating or arc energy dissipation may also occur at the same area under certain hot switching conditions. Thus during cycling, this part of the micro-contact is more susceptible to potential damage (as is shown in figure 7). After an amount of material volume change occurs on the front edge of the micro-contacts, the small vertical lift of the bottom electrode during switching (~ 1.8 μm) will not be sufficient to allow touching between the worn bottom electrode and worn micro-contacts. Consequently, no electrical contact is made between the upper micro-contacts and the bottom sample, leading to an open circuit situation.

It must be emphasized that this electrical failure is not an absolute indicator of the lifetime of the MEMS switches. Instead, it serves as an indicator that a certain amount of surface modification occurred on the micro-contacts and the bottom contacts during a switching test (enough that the preset piezoelectric actuator displacement distance is no longer sufficient to produce physical contact of the micro-contacts and bottom electrode; only the insulating tip touches the bottom contact area). Thus it allows a direct comparison of material wear rates of different contact materials. These same lifetime limiting factors such as mechanical wear, transient current heating and arc energy dissipation are expected in the operation process of real MEMS switches. The difference for real MEMS switches is that the tilt angle is normally less than 1°, the cantilever is not pre-bent, and the insulating tip does not touch the bottom electrode. Thus in actual MEMS devices it takes a substantially larger number of cycles to accumulate damage over the whole micro-contact to reach an electrical failure. We are not presently able to absolutely correlate this accelerated lifetime to an actual device lifetime; however, the relative difference between measured lifetimes in this test facility should be proportional to differences in actual device lifetime under similar operation conditions. Thus, our unique electrical failure mechanism may be used as an efficient tool to more quickly evaluate switching performance of different materials under a variety of different test conditions.

4.6 Effect of open circuit voltage (hot switching) on material transfer

The (accelerated) switching lifetime tests reported here are typically undertaken under aggressive test conditions, including hot switching, ambient air and greater contact force (up to 2-3 times the contact force of the commercial device). Under such hot switching conditions, the open-circuit voltage (V_{oc}) may produce arc discharges and substantially high transient currents (decays to 1mA within a few μs) during closing, and these are expected to accelerate the failure process. In order to assess the effect of V_{oc}, both hot switching and cold switching test conditions were investigated in the switching test for pure gold. In the test, each MEMS cantilever was cycled upon a pure gold bottom electrode for a certain number of cycles. A stable contact resistance of 0.6 – 0.7 Ohms was achieved during all the tests. After characterization, the AFM data of each micro-contact and bottom electrode were analyzed using Gwyddion software. The sum of the material volume change of the two micro-contacts for each sample is listed in table 2. The material transfer is observed to increase with cycle number under both hot switching and cold switching conditions, although the measured material transfer is much less in the case of cold switching. These results reveal the capability of this test facility to effectively evaluate material wear under various test conditions.

Differentiating electrically-induced wear effects (such as the open circuit voltage effect) from the purely mechanical wear effects in this new test system is an important step toward our research into novel alternative contact materials. Since arc energy dissipation, transient current heating and mechanical wear are typical lifetime limiting factors for hot switching MEMS switches, it is valuable to test different contact materials under various conditions to distinguish the effects of these factors.

Table 2: Effect of V_{oc} on Material Transfer (Pure Gold)

Sample	V_{oc} (DC) (Volt)	Cycle Number	Transferred Material Volume (μm^3)
1	6	1000	0.046
2	6	2000	0.116
3	6	3600	0.430
4	0	3600	0.007
5	0	40,000	0.090

4.7 Effect of contact material on MEMS switch lifetime

Au-Ni alloys were investigated as an alternative contact material for MEMS switches. The enhanced hardness is expected to improve the lifetime by reducing material wear during the switching operation. The closed contact resistance evolution for gold micro-contacts against either Au or Au-Ni (20 at. % Ni) bottom electrodes is shown in figure 9. The number of cycles to electrical failure is about 1200 for the Au-Ni bottom electrode. Compared to the pure gold electrode, the "life time" is dramatically improved. Figure 10 shows the SEM and AFM analysis of upper gold contacts after failure. The damaged area is again located on the front edge of the micro-contact, where impact occurs. Also similar to the previous case, material loss in the contact area is confirmed by the height profile image comparison. Material built-up surrounding the impact area on the micro-contact occurs in drop-like shapes that are reminiscent of local melting. The melt-like gold droplets are also observed at the foot of the micro-contact on the upper electrode of the cantilever.

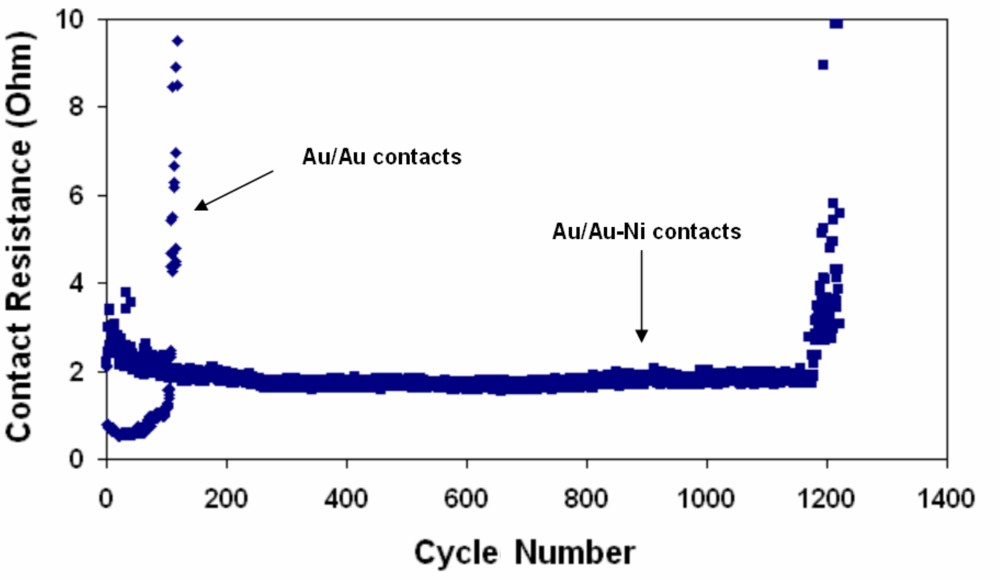

FIG. 9: Contact resistance evolution for Au contacts against Au-Ni (20%) alloy contacts. The gold against gold test result is also shown as a comparison.

AFM and SEM analysis of Au-Ni (20%) bottom electrodes after failure are shown in figure 11. Material built-up on the bottom electrode is apparent. A few small indented holes can also be identified. The diameter of the holes is typically less than 0.5 µm and the depth is less than ~20 nm. Thus the damage volume is greatly reduced in comparison with that of the pure gold bottom electrode, even though the number of cycles before failure is more than 10 times higher. Compared to the pure gold against pure gold test, the gold against gold-nickel test shows a much longer "life time" under the same test conditions (1mA, V_{oc} = ~ 1V, a total of 300 µN on two contacts). Also, the SEM and AFM failure analysis show that the damage is less severe, even though the total number of cycles is much larger for Au-Ni contacts. It is shown that material transfer on the upper micro-contacts changes the topography and the shape of the micro-contacts. The damage accumulates until the contact geometry is changed.

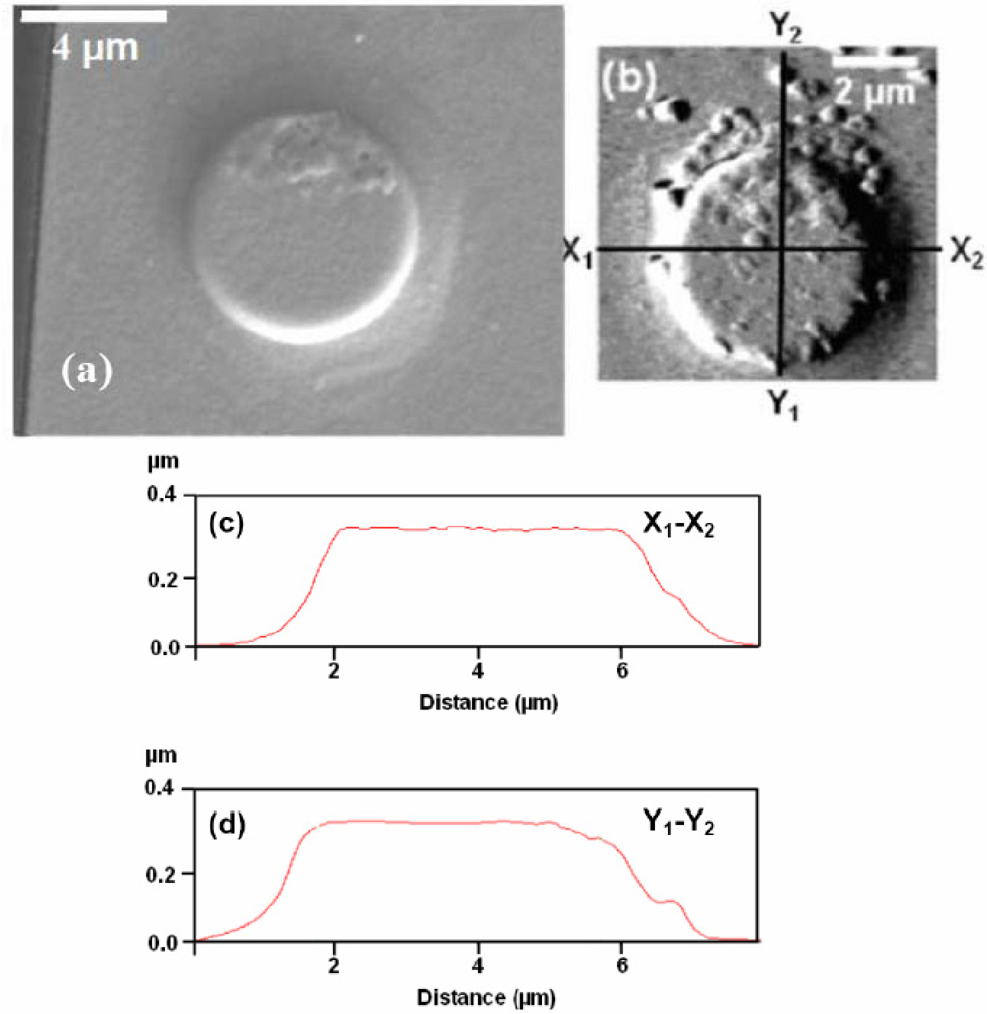

FIG. 10: Analysis of failed upper gold contacts (against Au-Ni 20 at. %) after the failure. *(a), (b)* SEM image and AFM image of the micro-contact; *(c), (d)* Height profiles corresponding to X_1-X_2 and Y_1-Y_2.

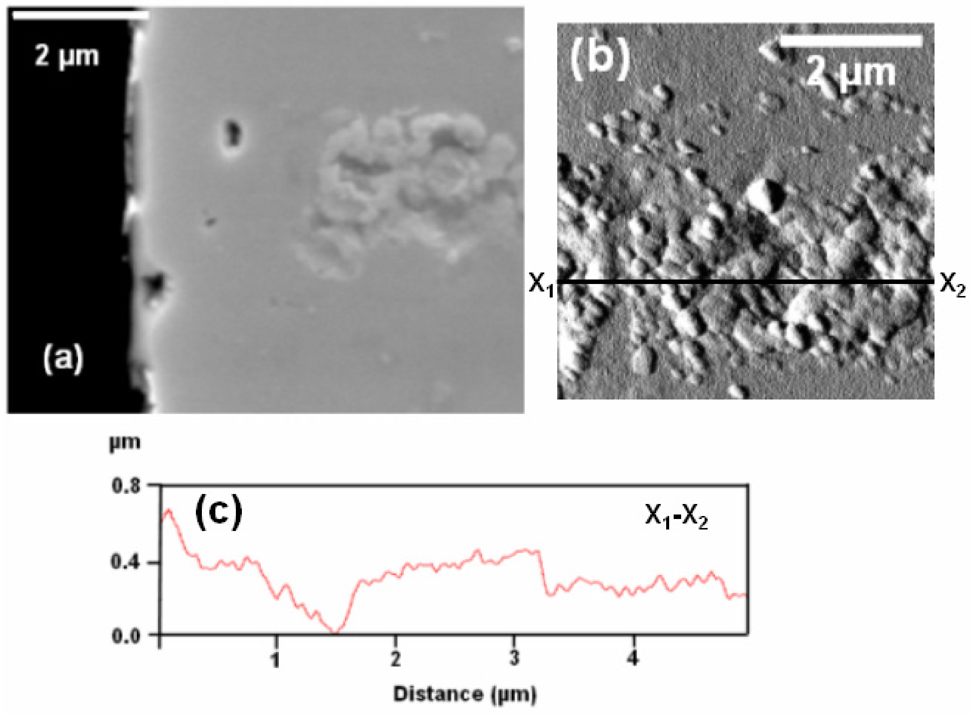

FIG. 11: Gold nickel bottom electrode after failure (1mA). *(a)* The SEM image and *(b)* the AFM image of the micro-contact. *(c)* The height profile along X_1-X_2.

In this way, an open-circuit situation is then formed because the insulating lip of the cantilever touches the bottom electrode instead of the micro-contacts. The pure gold against pure gold contact seems more susceptible to hot switching degradation and mechanical wear, leading to much more rapid failure while achieving lower contact resistance (~0.2 Ω /contact). Detailed discussion of material properties effect on hot switching energy dissipation is beyond the scope of this facility paper and will be presented elsewhere.

The micro-hardness of the gold-nickel bottom electrode is much greater (~6.1 GPa) compared to that of pure gold bottom electrode (~2.7 GPa). The adhesion between gold and gold nickel surfaces is also expected to be lower. All of these will make the contacts more resistant to force-induced damage. Pure gold deformation upon gold nickel bottom contacts allows stable electrical contact with low contact force (~150 μN/ contact). It is shown that both the upper and lower electrodes are less damaged despite a much larger total cycled number. Failure appears to arise from material transfer from the contact area of the upper contacts to the surrounding area and the bottom electrode. The harder Au-Ni shows more resistance to deformation, but also leads to a slightly higher contact resistance (~1 Ω/ contact). The AFM and SEM observations suggest that local melting may occur during the cycling test.

4.8 Conclusions

In this paper, a new test facility for MEMS contacts is described. The test utilizes cantilevers from commercial switches, and mimics the operation of real RF MEMS contact switches. It allows efficient tests of different candidate contact materials as bottom contacts against upper pure gold micro-contacts. Using this facility, candidate materials for MEMS contacts can be efficiently examined and characterized in an accelerated manner. To demonstrate the facility, we have run standard Au-Au tests under different conditions (hot switching vs. cold switching) followed by a volume analysis of material transfer. It has been verified that hot switching conditions accelerate the material transfer process. Standard Au-to-Au contacts were compared with Au-to-Au-Ni (20 at. % Ni) contacts under accelerated test conditions. We have observed that the harder gold nickel alloy displays almost one order of magnitude improved "lifetime" or wear resistance compared to a pure gold bottom contact.

4.9 References

[1] L. E. Larson *et al*, “Micromachined microwave actuator (MIMAC) technology-a new tuning approach for microwave integrated circuits,” *Microwave and Millimeter-Wave Monolithic Circuits Symposium Digest*. (*Boston, MA*) pp 27-30, 1991

[2] A. S. Morris, S. Cunningham, D. Dereus and G. Schopfer, “High-performance integrated RF-MEMS: Part 1 – the process,” *Proceedings of 33rd European Microwave Conference*, 2003, pp. 21-24

[3] G. Rebeiz, *RF MEMS Theory, Design, and Technology*, (NJ: Wiley), 2003

[4] J. Schimkat, “Contact materials for microrelays,” in 11th Proc. MEMS’ 98 Workshop, 1998, pp. 190-194

[5] K. Hiltmann *et al.* “New micromachined membrane switches in silicon technology,” *47th IEEE Holm Conference on Electrical Contacts*. pp 117-121, 2001

[6] K. Hiltmann *et al*., “Micromachined switches for low electric loads,” *Sensors and Actuators A* 74, pp. 203-206, 1999

[7] R. A. Coutu, Ph.D. Dissertation: *Electrostatic radio frequency (RF) microelectromechanical systems (MEMS) switches with metal alloy electric contacts*, Air Force Institute of Technology, September 2004

[8] L. Chen, “Contact evolution in micromechanical switches,” in *World Tribology Congress,* Washington D. C., U.S.A. 2005

[9] D. Hyman and M. Mehregany "Contact physics of gold microncontacts for MEMS switches", IEEE transactions on components and packaging technology, 22 p. 357, 1999

[10] S. Majumder, J. Lampen, R. Morrison and J. Maciel, "MEMS switches," *IEEE Instrumentation & Measurement Magazine,* pp. 12-15 (March 2003)

[11] A. Morris, *Technical data on RF MEMS switches, wiSpry Inc. (Irvine, CA),* 2006

[12] S. Senturia, *Microsystem Design* (Netherlands: Kluwer Academic Publisher), 2001

[13] B. D. Jensen *et al*., "Force dependence of RF MEMS switch contact heating," *17th IEEE International Conference on. (MEMS)* pp 137-140, 2004

[14] S. C. Bromley and B. J. Nelson, Electrical Contacts, "Performance of microcontacts tested with a novel MEMS device," Proceedings of the Annual Holm Conference on Electrical Contacts, 2001, p 122-127.

[15] R. S. Timsit, *Electrical Contacts: Principles and Applications* (New York: Marcel Dekker), 1999.

[16] D. S. Perloff, "Four-point sheet resistance correction factors for thin rectangular samples," *Solid-State Electronics* **20** 681-687, 1977

[17] Z. Yang, D. Lichtenwalner, A. I. Kingon, unpublished.

[18] D. Brenner, M. Zikry et al, unpublished.

CHAPTER 5

Comparison of Au and Au-Ni Alloys as Contact Materials for MEMS Switches

(This chapter has been submitted to Journal of Microelectromechanical Systems)

5.1 Abstract

This paper reports on a comparison of gold and gold-nickel alloys as contact materials for microelectromechanical system (MEMS) switches. Pure gold is commonly used as the contact material in low-force metal contact MEMS switches. The top two failure mechanisms of these switches are wear and stiction, which may be related to the material softness and the relatively high surface adhesion respectively. Alloying gold with another metal introduces new processing options to strengthen the material against wear and reduce surface adhesion. In this paper the properties of Au-Ni alloys investigated as the lower contact electrode were controlled by adjusting the nickel content and thermal processing coditions. A unique, efficient switching degradation test was conducted on the alloy samples, using pure gold upper micro-contacts. Solid-solution Au-Ni samples showed reduced wear rate but increased contact resistance, while two-phase Au-Ni (20 at. % Ni) showed a substantial improvement of switching reliability with only a small increase of contact resistance. Discussion of the effects of phase separation, surface topography, hardness, and electrical resistivity on contact resistance and switch degradation is also included.

5.2 Introduction

Radio Frequency (RF) MicroElectroMechanical System (MEMS) switches demonstrate great potential for a spectrum of microwave applications. Compared to conventional field effect transistors (FET) and PIN diodes, RF MEMS switches offer much lower power consumption, much better isolation and lower insertion loss. One major obstacle for large-volume commercial application of RF MEMS switches is reliability. A recent industrial survey has shown that stiction and wear are the top two failure modes for MEMS actuators [1]. For metal contact-type MEMS switches, pure gold is widely used as a contact material to achieve low contact resistance. Stiction and wear are prone to occur between two soft, adhesive contact surfaces while switching. Wear may be described as contact deformation and/or material re-distribution, ultimately causing contact surface roughening and affecting local contact force and contact resistance. Contact contamination has also been discussed as a degradation and failure mechanism. [2, 3].

There have been some efforts in the device design field to address this problem of Au to Au contact reliability [4-5]. Notably, Oberhammer introduced a mechanically bi-stable electro-static switching mechanism to achieve a small passive closing force and a large active opening force for soft metal contacts [6]. On the materials side, a few alternative metals and alloys have also been investigated as contact materials for metal contact MEMS switches. McGruer showed that ruthenium (Ru), platinum (Pt), and rhodium (Rh) were susceptible to contamination and the contact resistance increased after a characteristic number of cycles, while gold alloys with high gold percentage showed no contact resistance degradation under the same test conditions [7]. Coutu showed that alloying gold with a small amount of palladium (Pd) or Pt extended the microswitch lifetimes, with a small increase in contact resistance [8-9]. However, up to now, comprehensive investigations of the effects of surface topography, alloy composition and material microstructure on contact resistance and lifetime performance are lacking. In order to build a solid material knowledge base for microswitch designers, correlations among material properties, contacting performance (such as contact resistance, lifetime) and failure modes (such as stiction, wear/material transfer) need to be built based on systematic experimental data for different materials.

The research in this area has been slowed by the long time requirement for fabricating a microswitch with a particular new contact material. Typically, these microswitches are fabricated in Si foundries, and only a limited range of materials may enter the fabrication facility. Secondly, the fabrication process must be optimized for each material, and it may take many months to fabricate a set of switches to test a candidate contact material. Materials compatibility and process integration issues must be addressed in advance for every material to be tested.

Some convenient contact wear test facilities have been used to research the characteristics of microswitches. Notably, Hyman used a modified X-Y-Z micrometer station to investigate the contact physics and test current carrying capability of MEMS switches [10]. Schimkat used an accurate loading system to survey materials for micro-relay actuators [11]. A modified nano-indentor was also used to study hot-switching degradation of MEMS contacts [12]. One concern about these tests is that they do not closely mimic real microswitches. In particular, the tests have difficulty duplicating the switch geometry (mechanical moving parts are typically micro-scale cantilever structures with metal films being patterned on the surfaces) and the contact geometry (micro-contacts); these are important issues because the contact geometry has a strong influence on the stress and heat distribution across the contacts, and thus on the switch performance and failure mechanism [13, 14].

In our work, these issues were addressed by: comprehensively testing an alloy series of Au-Ni (with varied nickel composition); and utilizing a newly developed switching degradation test facility closely mimicking actual MEMS switch operation [15].

Besides the alloys mentioned in the above paragraphs, Au-Ni has materials characteristics showing it to be a potentially promising alternative to gold. It has been reported that Au-Ni alloy contacts yield much lower adhesion than pure gold contacts [9]. Low force (as low as 0.6 mN) stable contact and reliable re-opening were also achieved in the previous research report. However, in the previous study, only samples with one composition (5 % Ni) were investigated, using bulky samples (rivets) as test components instead of a MEMS test structure. Therefore we have undertaken a study of a wider range of alloy compositions, tested under a configuration typical of MEMS switches. The Au-Ni phase diagram is shown in Fig. 1 [16]. Note that both metals are FCC structures, and exist as a two phase mixture at relatively low temperature under equilibrium conditions. However, a metastable single phase alloy may also be produced under the low processing temperatures utilized for the film deposition. Thus, a comparison of the metastable solid-solutions and the two-phase mixtures of the same overall composition can be undertaken, so that both microstructure effects and composition effects can be examined.

The switching degradation test facility used for this study utilizes the upper cantilevers from commercial RF MEMS switches and tests these against alternative bottom contact materials, using a modified atomic force microscope (AFM) as described below. The emphasis is placed on a comparison of the alloys and correlations between material properties, contact resistance and contact degradation.

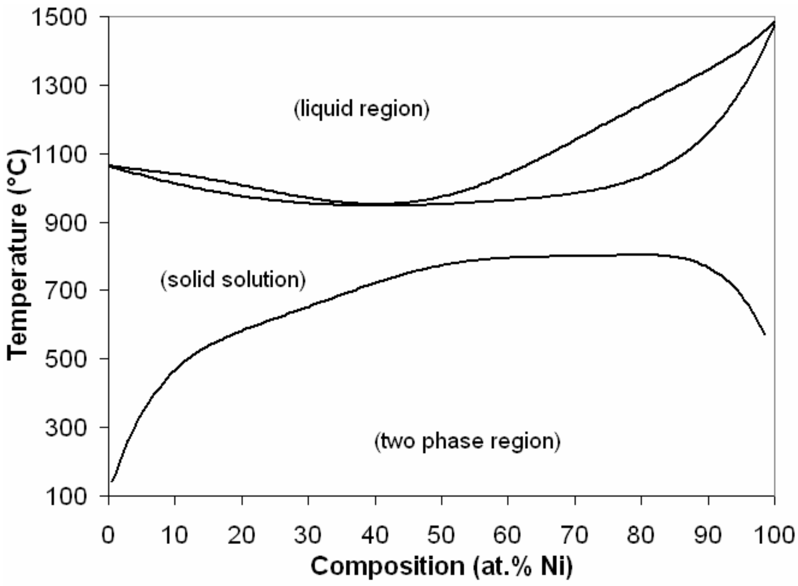

FIG. 1: Au-Ni phase diagram, after Okamoto and Massalski [16].

5.3 Experiment

We have designed a unique setup for monitoring MEMS switching behavior by integrating a real MEMS cantilever (from commercial wiSpry switches [17]) and separate thin film bottom contact materials under test into an atomic force microscope (AFM) [15]. The test configuration is shown schematically in Fig. 2. The contact is made between upper pure gold micro-contacts and bottom candidate contact materials. The contact resistance evolution and the switching motion are both monitored *in-situ*. The test switch is cycled on/off using a piezoelectric actuator. The switching mechanics is designed in such a way that contact resistance failure is highly sensitive to the contact surface degradation. During test, the MEMS cantilever is intentionally flexed in both "on" and "off" states to ensure a calibrated contact force. This pre-bent geometry also ensures a nearly vertical contact motion (less than 2.5° tilting) for the upper micro-contacts with respect to bottom contact pads. Contact area then is always located near the front edge of the micro-contacts due to this slight tilting. Vertical oscillation of the bottom contact pads alternates the contact points between the cantilever edge (insulating) and the micro-contacts, with these two states corresponding to the electrical "open" and "closed" states. We are aware that in the commercial wiSpry switches with which we are making comparison, the ultimate rise in resistance appears to correlate with substantial deformation of the switch contacts, consistent also with other reports [7, 13]. We have therefore made this test more sensitive to contact deformation by limiting the vertical travel of the piezoelectric actuator. As deformation occurs, the on-state contact is affected, and resistance rises markedly. As shown later in the Results section, this will occur after dramatically fewer cycles than in service, primarily because the limited travel will result in an "out-of-contact" condition after substantially less contact deformation than in the case of the commercial switch. Thus we can accelerate our investigation of contact degradation as a function of contact material, while using the commercial cantilever in a test that is strongly representative of the actual operation.

Further conditions are briefly summarized below.

a. The test is typically undertaken under 'hot-switching' conditions. This term is used by the electrical switch community for the condition where a field is present when switch opening and closing takes place. The open circuit voltage (V_{oc}) is set at 1 volt. The measurement current is 1 mA, a value reached after a higher current transient. Our results suggest that the transient does accelerate switch degradation, and the transient was therefore kept constant for all the comparative tests.

b. The contact force is calibrated as ~150 μN / contact, which is up to twice the contact force of the wiSpy's micro-switches under service conditions. This increased contact force was adopted to the increase deformation and wear rate, but was also carefully controlled for the comparative evaluations of the contact materials. Since the tests were conducted in ambient air, a relatively large contact force also helps to penetrate any surface contamination film that may be present and ensure a metal-metal contact.

Therefore, under the test conditions utilized in this investigation, the effective lifetimes are substantially shortened [15], which enables differences between contact materials to be more readily distinguished.

Pure Au and Au-Ni alloy (with up to 20 at. % Ni) bottom contacts samples were prepared using ion-beam sputter-deposition. Xenon gas was used in the ion source due to its relatively large mass, reducing energetic bombardment of the growing film. The base pressure was $< 3 \times 10^{-7}$ torr and the deposition pressure was 2×10^{-4} torr. The accelerating voltage for the beam is 600 V and beam current is 20 mA. The substrate is a silicon wafer coated with a 1000 Å thick thermal oxide. A 5 nm Chromium (Cr) layer and a 10 nm molybdenum (Mo) layer were deposited as an adhesion layer and a diffusion barrier layer, respectively. A 250 nm film of pure Au or Au-Ni (with various nickel composition) was then deposited.

The Au-Ni alloy was prepared by co-sputtering from a rotating gold target partially covered with a piece of the alloying metal (Ni). The atomic percentage then was determined by the fractional target area the nickel occupies (in percent area, or equivalently, the angle θ in comparison to 360^o) and its sputtering yield (Y) compared to that of gold. The required angle θ was calculated as follows:

$$At.\%\ A = \frac{Y_A \cdot \theta_A}{Y_A \cdot \theta_A + Y_B \cdot \theta_B} \tag{1}$$

$$\Rightarrow \quad \theta = \frac{360^\circ}{1 + \frac{1 - at.\%\,A}{at.\%\,A} \cdot \frac{Y_A}{Y_B}} \tag{2}$$

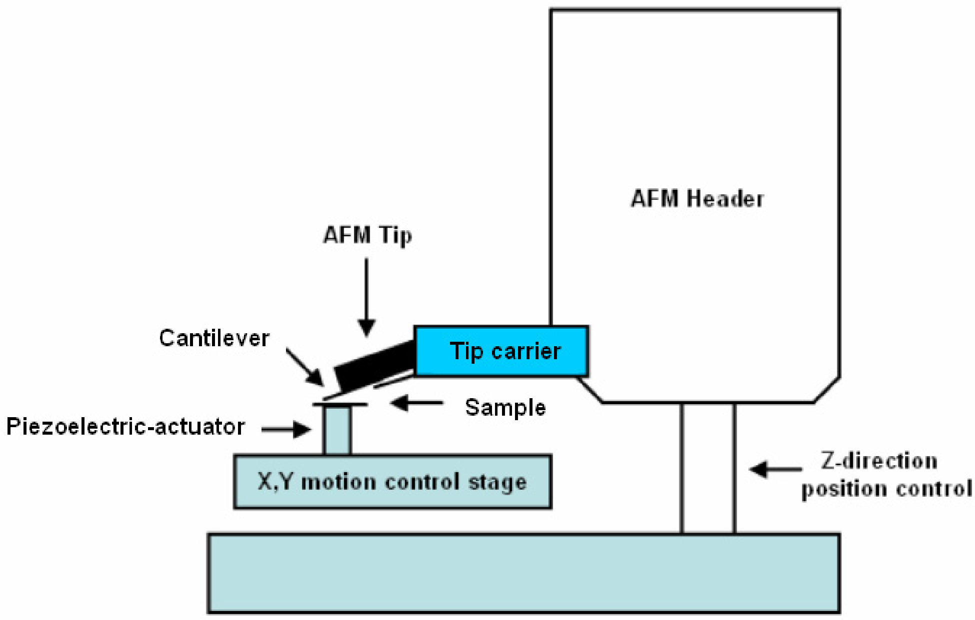

FIG. 2: Configuration for the switching tests.

where A and B are the different materials. The sputtering yields of Au and Ni under Xe ion bombardment were taken from Ohring [18]. The *in-situ* rotation of the target ensures the uniformity of the film composition. The films were patterned using standard photolithography, to facilitate the four point probe measurement of the contact resistance during the switching lifetime tests. Ion beam etching thereafter was used to remove metal films off the uncovered area. N-methyl pyrrolidinone (NMP) solution and de-ionized water was used in sequence to dissolve the photo-resist layer and clean the sample, respectively. Electrical resistivity data was obtained on as-deposited thin films (before patterning) using the four point probe technique (MAGNE-TRON Model-700). A four-point sheet resistance correction [19] was applied. Micro-hardness data was obtained using a Hysitron Triboscope nano-indentor (Berkovich indenter tip-142.5° included angle). Surface topographic images were taken on the as-deposited thin films using a CPR Atomic Force Microscope. Related software was used to obtain roughness statistics and height-profile analysis. A BRUKER AXS X-ray diffractometer was used to identify the sample structure. RIBER LAS-3000 X-ray Photoelectron Spectroscopy (XPS) was used to detect the surface chemical composition (< 10 nm). The take off angle was ~ 75° from the sample surface. A MAC-2 analyzer and Mg Kα (1253.6 eV) source were used in the experiment.

5.4 Results and Discussion

Gold alloy lattice parameters obtained by X-ray diffraction (XRD) are shown in Fig. 3, for films of various Ni content. In the figure, the lattice parameter (measured in the direction normal to the wafer surface) is plotted versus the expected Ni at. %, compared to values for bulk solid-solution alloys (represented by diamonds, along the trend line)[20]. The room temperature deposited thin films (Fig. 3, triangles) show a larger than expected lattice parameter, consistent with the effects of compressive stress. A series of Au-Ni samples were deposited with 200 °C *in-situ* heating. For these heated samples (Fig. 3, squares), the lattice parameter fits the bulk literature data quite well, indicating the compressive stress can be minimized by moderate *in-situ* heating. More importantly, we can conclude from the XRD data that all as-deposited samples yield the metastable solid solution phase (no nickel peaks are observed), and our Ni content calculation is correct as well.

In order to obtain the stable two-phase mixture, rapid thermal annealing (RTA) was conducted on some samples. Samples were heated at 600 °C for 30 seconds in flowing N_2 gas. An X-ray diffraction spectrum after RTA is shown in Fig. 4. In the spectrum, Au (111), Au (200), Ni (111) and Ni (200) peaks can be clearly identified. The precipitation of a nickel–rich phase is confirmed (not present before the RTA). Therefore, the effects of solid-solution hardening versus precipitation hardening can be compared. Note that, however, if nickel precipitates are present at the surface, they are susceptible to oxidization in air.

The properties of the Au and Au-Ni alloys are summarized in Table 1. It can be seen that the measured electrical resistivity and micro-hardness increase with increasing Ni-content in the single phase metastable alloys. Annealing the Au-Ni alloy (20 at.% Ni) to form the two-phase mixture significantly lowers the resistivity and hardness compared to the pre-annealed values.

The bulk resistivity is not the key parameter for the MEMS switches – rather it is the contact resistance. We would like to gain some insight into the factors controlling this contact resistance. The relationship between force and contact resistance for gold-contact MEMS switches has been investigated by previous researchers [10, 21, 22]. For a contact radius greater than the electron mean free path, the Maxwell spreading resistance model can be used to calculate the contact resistance. In our test, the nominal contact radius is much larger than the mean free path in gold (~ 36nm), so the model should be valid. The contact resistance R_c is described by:

$$R_c = \frac{\rho}{2r_c} \tag{3}$$

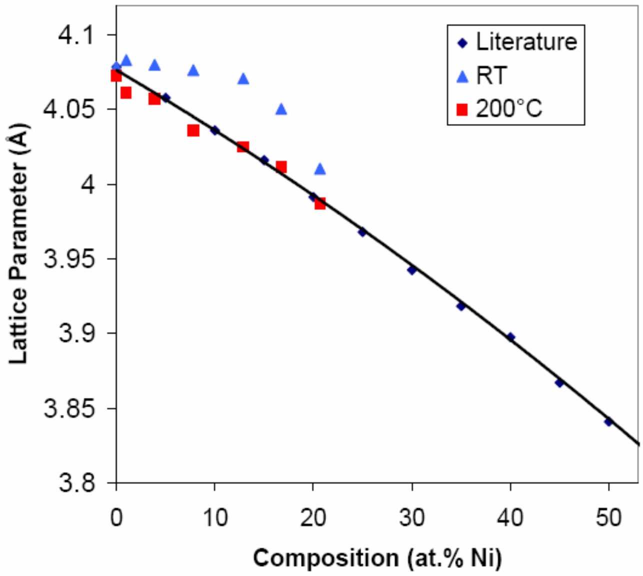

FIG. 3: Lattice parameter vs. nickel composition for films deposited at room temperature, and 200 °C, compared to bulk solid solution alloys [from ref 20].

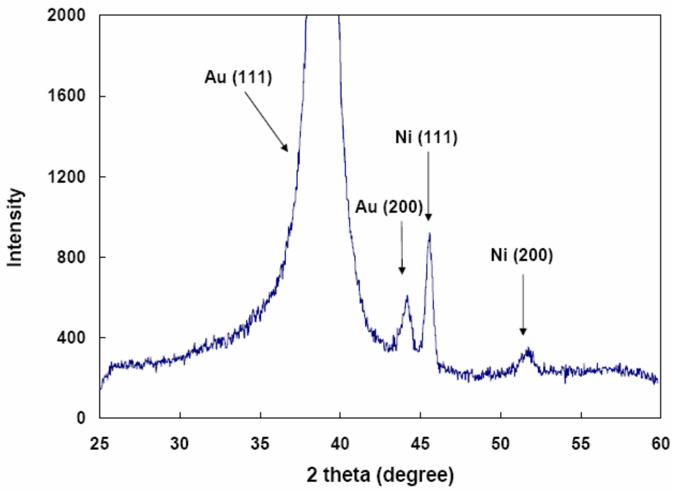

FIG: 4. XRD spectrum of the Au-Ni (20 at.% Ni) after rapid thermal annealing where ρ is the resistivity, r_c is the contact radius [23]. While two different materials are in contact, the resistivity is estimated as the average of the two. The contact radius can be obtained using an asperity deformation model [22]:

$$r_c = \sqrt{\frac{F}{\xi \pi H}} \tag{4}$$

where F is the applied force, H is the hardness of the material and ξ is the coefficient of the material deformation mode. Different modes are given as: $\xi < 0.3$, elastic deformation; $0.3 < \xi < 0.75$, elastoplastic deformation; and $0.75 < \xi < 1$, plastic deformation.

As described elsewhere, the contact force in our test is about 150 μN/microcontact [15]. Plastic deformation is assumed based on this force over the hundred-nanometer-scale contact area. For the contact between different materials, which is the case in our experiments, the averaged hardness is used for the calculation. The electrical resistivity, micro-hardness, measured and calculated contact resistance data (against upper pure Au micro-contacts) for the pure Au and Au-Ni samples are shown in Table I. The calculated and measured contact resistances are also plotted in Fig. 5. As the electrical resistivity and micro-hardness increase with Ni percentage, the model (calculated values) shows an increase of contact resistance. The experimental contact resistance data roughly follow this trend. For pure Au samples, the experimental data fits the calculated contact resistance data quite well. However, for the Au-Ni metastable solid solution series, the measured contact resistance is much higher than the calculated value. Two-phase Au-Ni samples (20 at.% Ni) showed a much lower contact resistance compared to the solid solution alloy at the same composition. Furthermore, the model in this case again correctly predicted the measured contact resistance based on the physical properties of the films and the contact force.

Based on the above analysis, it might be reasonable to suggest that, for the Au-Ni solid solution series, the mismatch between the calculated and measured contact resistance is due to the fact that the roughness effect is not included in the model. To gain insight into this issue, a detailed topographic analysis was performed using AFM.

TABLE I. MATERIAL PROPERTIES OF Au-Ni FILMS

Nickel Composition (at. %)	Electrical Resistivity (μΩ·cm)	Micro-hardness (GPa)	Calculated Contact Resistance (Ω) (Eq. 3, 4)	Measured Contact Resistance (Ω) (± 5%)
0	3.8	2.7	0.14	0.16
3.9	6.9	3.0	0.25	0.35
7.8	10.5	4.3	0.30	0.62
12.9	13.2	4.8	0.41	0.75
16.7	19.2	5.7	0.51	0.88
20	20.5	6.1	0.63	0.95
20 (two phase)	15.5	4.1	0.37	0.4

A series of AFM Au-Ni topographic images with grain height analysis and RMS surface roughness data are provided in Fig. 6 – Fig. 10. Topographic and error images of a pure gold sample, a solid solution Au-Ni (20 at.% Ni) sample and a two-phase Au-Ni (20 at.% Ni) sample are shown respectively in Fig. 6, Fig. 7 and Fig 8.

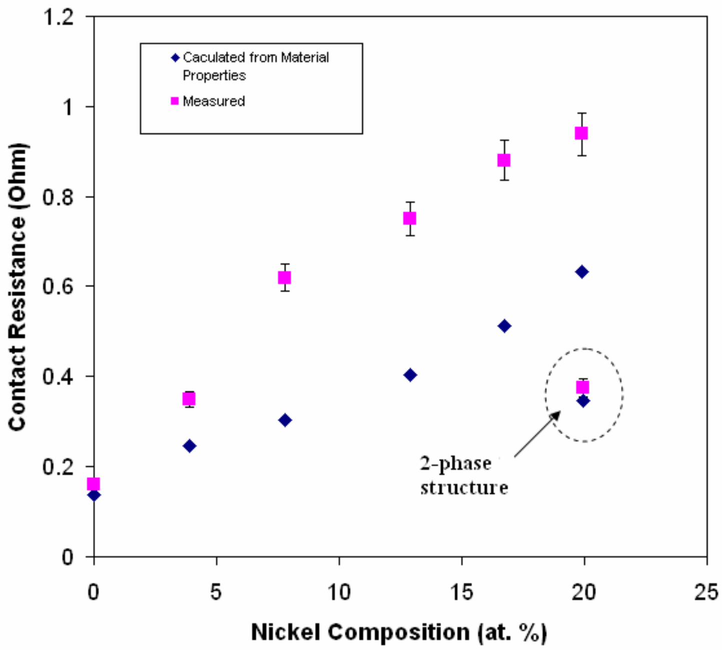

FIG. 5: Calculated and measured contact resistance vs. nickel composition.

Height profile line-scans across the sample surfaces are also included in each figure (note that the height scale bar in Fig. 6 is different from those in Fig. 7 and Fig. 8.) Maximum height difference in the line-scans, and RMS surface roughness data are charted in Fig. 9 and Fig. 10. The topographic analysis can be summarized as:

a. The metastable single phase Au-Ni alloys show a marked trend of increasing roughness with increasing Ni content.

b. The rapid thermally annealed, two-phase Au-Ni alloy (20 at.% Ni) shows an entirely different microstructure with a surprisingly reduced roughness compared to the pre-annealed state. The mechanism for the surface smoothing is not yet determined.

c. The Au and the two-phase Au-Ni alloy (20 at.% Ni) samples show comparable values of roughness despite very different microstructures and grain size. The similar values of contact resistance should also be noted

Generally, it is assumed that rough surfaces yield lower contact areas than smooth surfaces. As a result, measured contact resistances for Au and two-phase Au-Ni samples fit quite well with calculated values while solid solution Au-Ni samples show higher contact resistance than expected. This study calls for more advanced contact resistance modeling, in which the topology effect of the contact surfaces needs to be addressed. Recently, some progress has been made in this area [24].

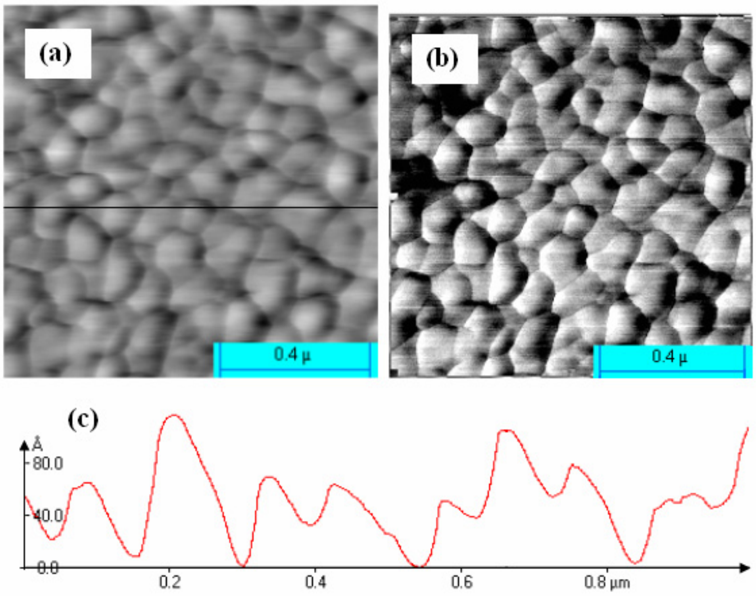

FIG. 6: AFM images of pure Au sample (a) topographic (b) error (c) random line height profile

It is an initially surprising result that rapid annealing of a metastable solid solution Au-Ni (20 at.%) sample resulted in a much smoother surface for the two phase structure. Nevertheless, in the application of metal contacts for MEMS switches, this material processing method enables us to achieve a good combination of low surface roughness, low contact resistance, and increased material hardness.

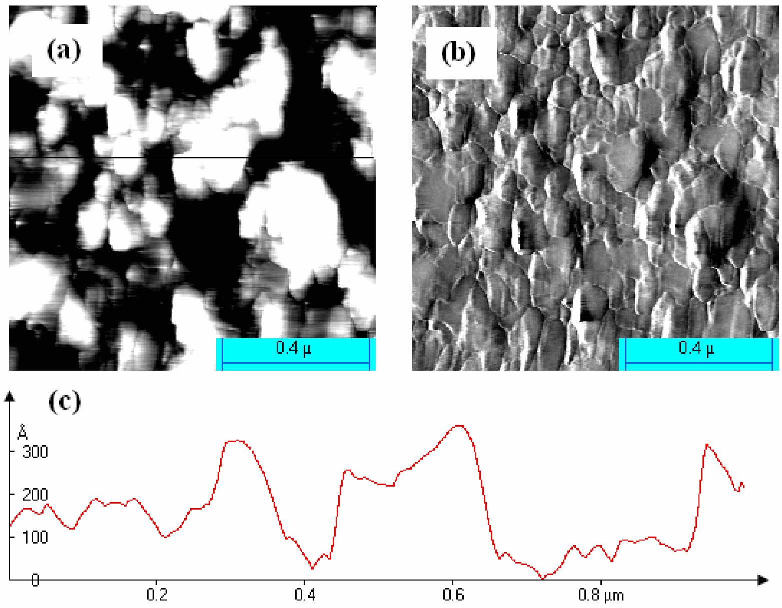

FIG. 7: AFM images of Au-Ni (20 at. % Ni, solid solution, as-deposited) sample (a) topographic (b) error (c) random line height profile.

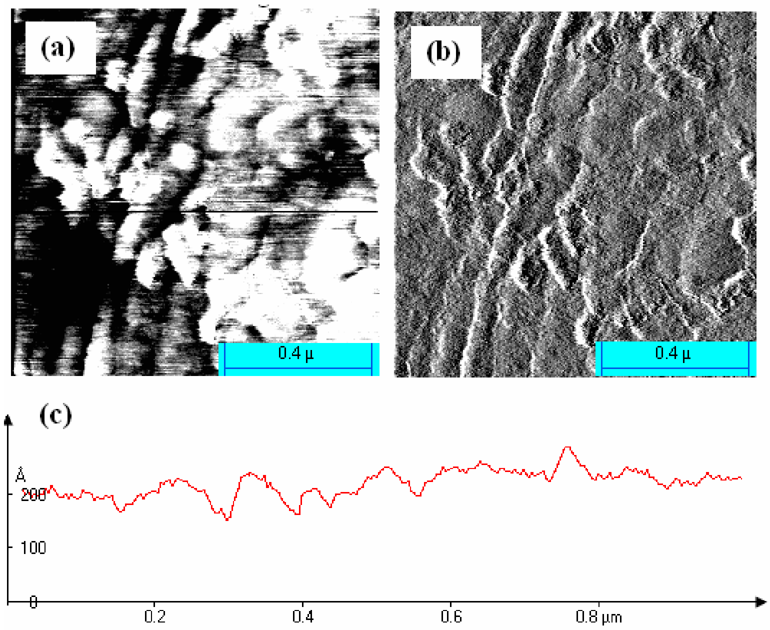

FIG. 8: AFM images of Au-Ni (20 at.% Ni, two phase, after RTA) sample (a) topographic (b) error (c) random line height profile.

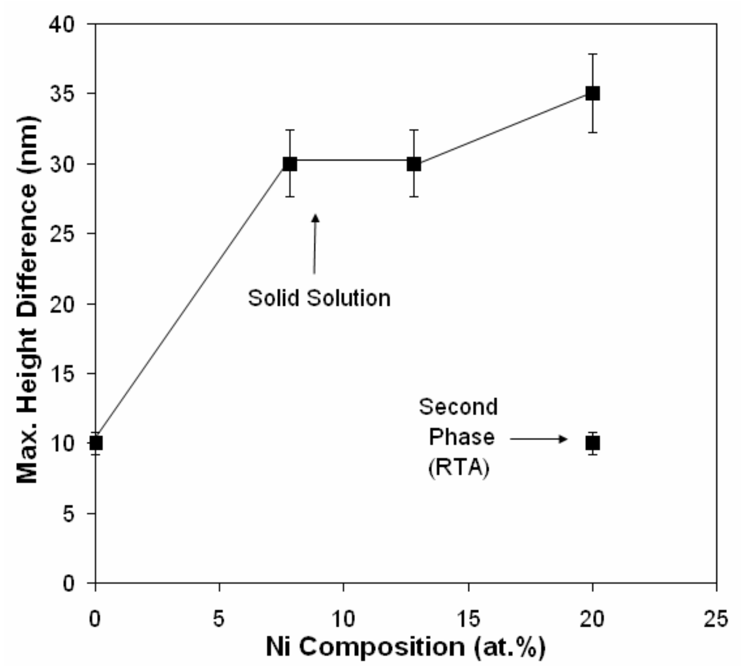

FIG. 9: Max. height difference in the random line-scan vs. Ni composition.

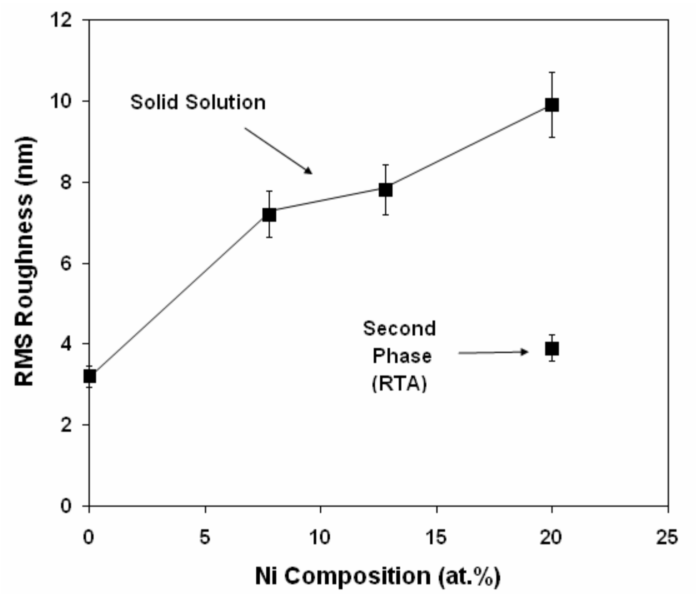

FIG. 10: RMS roughness vs. nickel composition.

Pure Au and Au-Ni thin film test structures were subjected to the switching degradation tests. Hot switching conditions were selected for the comparisons. The test conditions and unique electrical failure detection mechanism are as described in the experimental section. The test results are shown in Fig. 11, showing the closed state resistance as a function of switching cycle (note that a test cantilever has two micro-contacts; thus the resistance in Fig. 11 is roughly twice the contact resistance values in Fig. 5). Failure is indicated by the contact resistance increasing towards the open circuit value. It is clear that the number of cycles before failure increases as %Ni in the alloy increases.

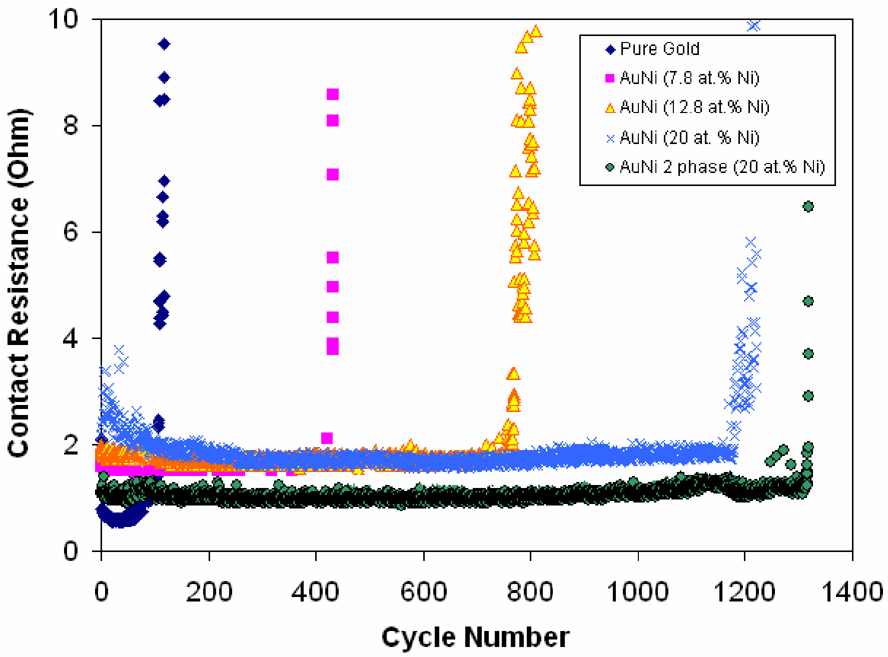

FIG. 11: Micro-contacting tests on pure gold and Au-Ni alloys.

Typical worn microcontacts on the Au cantilever, and corresponding bottom electrodes in the degradation tests of Au against Au, and Au against solid solution Au-Ni (20 at.% Ni), are shown in Fig. 12. As indicated by the AFM pictures, the top electrode wear occurs predominantly on one edge, due to a small angle between top and bottom contacts. Although the accumulated number of cycles of the Au against Au-Ni (20 at.% Ni) test is ~ 3000, more than twice that of the Au against Au test (~ 1300 cycles), Au-Ni (20 at.% Ni) shows less indentation on the bottom electrode. Information revealed by the test can be summarized as:

a. Low initial contact resistance was achieved for all the tests. A slight decrease of the initial contact resistance can be observed after a number of cycles. Notably, the contact resistance of solid solution Au-Ni (20 at.% Ni) drops from the initial value of ~3.5 Ω to the stable value of ~1.8 Ω after a couple hundred switching cycles. This "burn-in" period is less obvious for all the other samples. The low initial contact resistance suggests that any surface contamination film is insignificant. The relatively large contact force (150 μN /microcontact) utilized in the tests, and possible arc energy dissipation and transient current heating may remove surface contamination. In the case of low-force cold switching of RF MEMS switches in ambient air, typically a higher initial contact resistance is observed [2, 25]. Contamination accumulated on the contact surface during cold switching might easily degrade the contact resistance by orders of magnitude.

b. Pure gold yields the lowest cycle number before electrical failure. Solid solution Au-Ni alloys showed increased cycle number with increased nickel composition. Adding nickel to gold increases hardness, electric resistivity and roughness. As a result, there is reduced effective contact area and less surface adhesion in the on-state. The tradeoff for the extended lifetimes is a relatively higher contact resistance (~ 1.8 Ω). In the MEMS community, hot switching failure is thought to be primarily caused by arc-induced material transfer or transient current heating. Mechanical wear is therefore thought to be a minor factor in the hot switching failure process. However, our data indicates that strengthening the gold alloy substantially retards the contact failure process under hot switch conditions. This might be an indicator that arc/ current-heating induced material transfer could be affected by the mechanical properties of the contact materials. A more detailed investigation of the field induced material transfer mechanisms are being reported elsewhere.

c. Two-phase Au-Ni yields the largest cycle number while providing a stable, acceptable contact resistance (~ 1 Ω). Compared to the solid-solution Au-Ni alloys, two-phase Au-Ni (20 at.% Ni) films have an intermediate hardness (4.1 GPa) while yielding a much larger contact area due to the film smoothness. However, the intermediate hardness of this material does not fit our original expectation that the switching reliability should increase with hardness. Furthermore, the large contact area is expected to enhance the material adhesion on the contact surfaces, thus, impacting the reliablity. The excellent performance of the two-phase alloy, and the contrast to the trends displayed by the single phase alloys, caused us to suspect surface-related effects. In order to investigate the chemical differences between solid-solution and two-phase sample surfaces, the chemical composition of the sample surfaces was examined using XPS, comparing Au-Ni (20 at.% Ni) solid-solution and Au-Ni (20 at.% Ni) second phase precipitation samples.

Fig. 13(a) shows the XPS spectrum of the solid solution Au-Ni (20 at. %) alloy. The nickel composition is calibrated according to the Ni 2p peak. The nickel atomic percentage is ~ 11.7 % (this value is only representative of the surface composition). Fig. 13(b) is the XPS spectrum for two-phase Au-Ni (20 at. %). The calibrated nickel composition on the surface is ~ 30.8 at. % in this case. The high resolution XPS spectra on two-phase Au-Ni (20 at. %) is shown in Fig. 13(c).

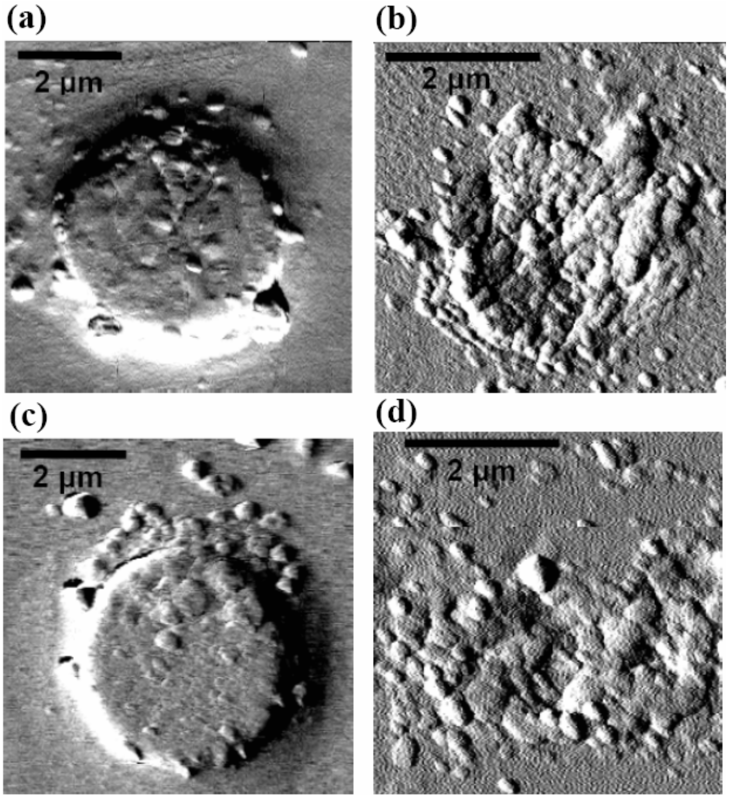

FIG. 12: AFM images of the worn microcontacts on the Au cantilever, and the corresponding bottom electrodes in the lifetime tests of Au against Au and Au against solid solution Au-Ni (20 at.% Ni). (a) A worn pure Au microcontact on the MEMS cantilever in Au against Au test (b) The worn area on the pure Au bottom electrode corresponding to the microcontact shown in (a). (c) A worn Au microcontact in Au against Au-Ni (20 at.% Ni) test. (d) The worn area on the Au-Ni (20 at.% Ni) bottom electrode corresponding to the microcontact shown in (c).

The dominant nickel species on the surface is identified as Ni_2O_3 from the Ni 2p 3/2 position [28, 29]. Therefore, precipitation of nickel from solid solution Au-Ni (20 at.%) alloys might be described as below: upon RTA, nickel starts to precipitate from the gold-rich matrix. Also, nickel near the surface precipitates preferentially at the surface (as well as at grain boundaries), and is oxidized upon air exposure.

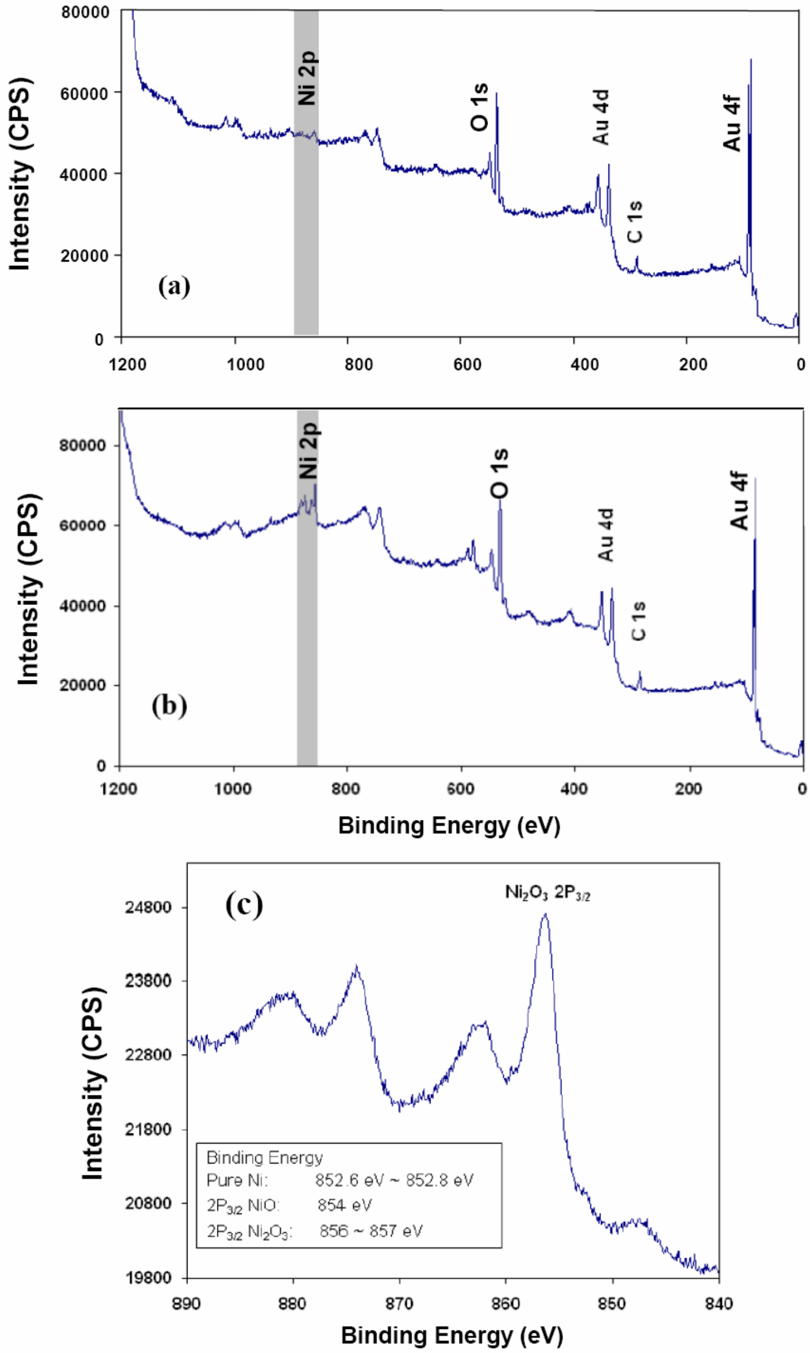

FIG. 13: (a) XPS spectrum on Au-Ni (20 at.% Ni) solid solution sample. (b) XPS spectrum on two-phase Au-Ni alloy sample (20 at.% Ni, after RTA). (c) High resolution XPS spectrum on Au-Ni (20 at.% Ni, after RTA) two-phase sample. The listed binding energy is taken from references [26-29].

The results of the XRD and XPS analyses, taken together with the Au-Ni phase diagram, indicate that after the RTA processing: some nickel atoms should remain as solid-solution hardening additions to the Au; some Ni exists as Ni-rich precipitates at the nano-scale; and some Ni migrates and forms nano-scale oxidized Ni_2O_3 islands on the surface. This engineered microstructure, having unique surface and volume compositions and properties, showed the best contacting performance among all the Au-Ni samples. These results point towards the need to understand and control both a) material composition and microstructure, and b) surface structure and properties, when selecting materials for MEMS contact switch applications.

5.5 Conclusion:

In this paper, a newly-developed switching degradation test facility is used to evaluate Au-Ni alloys as contact materials for MEMS switches under hot switching conditions. The experimental data shown in this paper provide a correlation between material properties (such as micro-hardness, electrical resistivity, surface topology, surface microstructure) and micro-contacting performance. In general, increasing material hardness increases the switching reliability, compared to pure Au. However, surface roughness needs to be maintained below a certain level in order to avoid detrimental effects on contact resistance. It also has been shown that post-deposition RTA treatment results in a two-phase Au-Ni alloy, which significantly improves micro-contact performance based on its unique material properties. The presence of some Ni_2O_3 oxide at the surface appears to correlate with a longer switching lifetime. These results suggest that both material volume and material surface properties must be considered for optimizing the properties of alloy thin films for MEMS switching applications.

5.6 References:

[1] C. Fung, "Industry study on issues of MEMS reliability and acccelerated lifetime testing", *2005 IEEE Int. Reliability Phys. Symp. Proc. 43rd Annu.*, pp 312-16.

[2] B. D. Jensen, L, L.-W. Chow, K. Huang, K. Saitou, J. L. Volakis and K. Kurabayashi, "Effect of nanoscale heating on electrical transport in RF MEMS switch contacts," *J. Microelectromechanical System,* 14 (5): pp.435-946, 2005.

[3] C. Brown, A. Morris, A. Kingon and J. Krim, "Cryogenic performance of RF MEMS switch contacts," Submitted to *J. Microelectromechanical System*

[4] A. Granaldi and P. Decuzzi, "The dynamic response of resistive microswitches: switching time and bouncing," *J. Micromech. Microeng.,* 16, pp. 1108-1115, 2006.

[5] P. Decuzzi, G. P. Demelio, G. Pascasio and V. Zaza, "Bouncing dynamics of resistive microswitches with an adhesive tip," *J. Appl. Phys.,*100, p. 24313, 2006.

[6] J. Oberhammer and G. Stemme, " Active opening force and passive contact force electrostatic switches for soft contact materials," *J. Microelectromech. Syst.,* 15, pp 1235-1242, 2006.

[7] N. E. McGruer, G. G. Adams, L. Chen, Z. J. Guo and Y. Du, " Mechanical, thermal, and material influences on ohmic-contact-type MEMS switch operation," in *19th Proc. MEMS '*06 Istanbul, Turkey, 2006, pp. 230-233.

[8] R. A. Coutu, P. E. Kladitis, K. D. Leedy and R. L. Crane, " Selecting metal alloy electric contact materials for MEMS switches," *J. Micromech. Microeng.* vol.14, pp. 1157-1164, 2004.

[9] R. A Coutu, J.R. Reid, R.Cortez, R. E. Strawser and P. E. Kladitis,

"Microswitches with sputtered Au, AuPd, Au-on-AuPt, and AuPtCu alloy electric contacts," *IEEE Trans. Comp. Packag. Tech.,* 29, pp. 341-349, 2006.

[10] D. Hyman and M. Mehregany, " Contact physics of gold microcontacts for MEMS switches," *IEEE Trans. Comp. Packag. Tech.,* 22, pp. 357-364, 1999.

[11] J. Schimkat, " Contact materials for microrelays," in *11th Proc. MEMS' 98 Workshop,* 1998, pp. 190-194.

[12] D. J. Dickel and M. T. Dugger, "The effect of surface contamination on resistance degradation of hot-switched low-force MEMS electrical contacts," in *Proc. 51st IEEE Holm Conf. Electric Contacts,* 2005, pp 255-258.

[13] L. Chen, "Contact evolution in micromechanical switches," in *World Tribology Congress,* Washington D. C., U.S.A. 2005.

[14] X. Yan, N. E. McGruer, G. G. Adams and S. Majumder, " Finite element analysis of the thermal characteristics of MEMS switches," in *12th Int. Conf. Transducers, Solid-State Sensors, Actuator and Microsystems,* 2003, 1, pp 412-415.

[15] Z. Yang, D. Lichtenwalner, A. Morris, S. Menzel, C. Nauenheim, A. Gruverman, J. Krim and A. I. Kingon, "A new test facility for efficient evaluation of MEMS contact materials," accepted July 2007 for publication in *J. Micromech. Microeng.*

[16] H. Okamoto and T. B. Massalski, *Phase diagrams of binary gold alloys,* Ohio: ASM international,, 1987, p. 196.

[17] A. S. Morris, S. Cunningham, D. Dereus and G. Schropfer, "High performance integrated RF MEMS: part 1- the process," *Proc. 33rd European Microwave Conf.* pp 21–4

[18] M. Ohring, *Material sciences of thin films*, Academic Press, 2002, p. 176.

[19] D. S. Perloff, "Four-point sheet resistance correction factors for thin rectangular samples," *Solid-State Electronics,* 20, pp. 681-687, 1977.

[20] A. F. Crawley and D. J. Fabian, " A redetermination of the lattice Spacings and Densities of Gold-Nickel Solutions," *J. Inst. Met.*, 94, pp 39-40, 1966.

[21] B. D. Jensen, L. W. Chow, R. F. Webbink, K. Saitou, J. L. Volakis, K. Kurabayashi, "Force dependence of RF MEMS switch contact Heating," in *17th. IEEE Int. Conf. MEMS*. 2004, pp.137-140.

[22] S. C. Bromley and B. J. Nelson, "Performance of microcontacts tested with a novel MEMS device," in *47th. IEEE Holm Conf. Electrical Contacts*. 2001, pp. 122-127.

[23] R. S. Timsit, *Electrical Contacts: Principles and Applications.* Newyork: Marcel Dekker, 1999, Ch.1, pp3-6.

[24] O. Rezvanian, M. Zikry, C. Brown and J. Krim, submitted to *J. Microelectromechanical System*.

[25] C. Brown, unpublished work in the Physics Department in North Carolina State University, NC, USA. ,

[26] V. I. Nefedov, M. N. Firsov, I. S. Shaplygin, "Electronic structures of $MRhO_2$, MRh_2O_4, $RhMO_4$ and Rh_2MO_6 on the basis of X-ray spectroscopy and ESCA data," *J. Electron Spectrosc. Relat. Phenom.* 26, p. 65, 1982.

[27] K. S. Kim and N. Winograd, "X-ray photoelectron spectroscopic studies of nickel-oxygen surfaces using oxygen and argon ion-bombardment," *Surf. Sci*, 43, p. 625, 1974.

[28] P. Lorenz, J. Finster, G. Wendit, J. V. Salyn, E. K. Zumadilov and V. I. Nefedov, "ESCA investigations of some NiO/SiO_2 and $NiO—Al_2\ O_3\ /SiO_2$ catalysts," *J. Electron Spectrosc. Relat. Phenom.* 16, p. 267, 1979.

[29] K. Kishi, "Adsorption of ethylenediamine on clean and oxygen covered Fe/Ni(100) surfaces studied by XPS," *J. Electron Spectrosc. Relat. Phenom.* 46, p. 237, 1988.

CHAPTER 6

Field-Induced, Directional, Nano-scale Material Transfer in MEMS Switching Tests

(This chapter is to be submitted to Journal of Micromechanics and Microengineering)

6.1 Abstract:

Research of metal-contact microelectromechanical MEMS switch failure under hot switching conditions is of great importance to its commercial applications in RF instruments. In this paper, we investigated the gold micro-contact degradation under such switching test conditions, and for the first time, we observed a nano-scale, directional material transfer phenomenon during the tests.With the open circuit voltage and current load both being well below the minimum arc voltage and minimum arc current (non-arc condition), gold contact material was found to transfer in the direction of the electrical field. And during our tests, no arc is detected by our *in-situ* high-resolution time traces. Reversing the field direction reverses the material transfer directionality. And this directionality can be eliminated using AC field. *In-situ* monitored contact resistance indicates that the contact surfaces are meta-stable during the switching operation. Our results suggest that, instead of metal phase arc, a new field-induced material transfer is responsible for the micro-contact degradation and cautions need to be taken to avoid thus degradation in MEMS switch design.

6.2 Introduction

Metal contact MEMS switches have a number of advantages over traditional relays and switches. Smaller sizes, low power consumption (electrostactic switches), lower cost and good compatibility with integrate circuit (IC) are some of the unique attractive features of this technology. Another major driving force for this technology is from the high frequency applications. The cut-off frequency of metal contact MEMS switches is much higher than semiconductor switching devices (etc. PINs and MOSFETs). MEMS switches can be operated under either cold switching conditions or hot switching conditions. ‘Cold switching’ refers to the operation condition under which no voltage is present across the two metal contacts during switch open and closure. ‘Hot switching’ refers to the operation condition that there is a voltage difference between the two metal contacts during switch open and closure. Metal contact MEMS switches has been demonstrated with high reliability under low-power cold switching conditions. [1, 2, 3] Starting from the year of 2006, cold switched MEMS switches have begun to replace traditional relays and switches in some automatic test equipment systems (ATEs). However, in order to expand to the area of RF instrumentation applications (etc. spectrum analyzers, oscilloscopes), hot-switching with high reliability and higher power handling ability needs to be realized [4]. As the first step toward this goal, understanding hot-switching failures in MEMS switches have become an important subject, but right now, still far from being accomplished. Up to now, as far as we know, no comprehensive investigation of hot switching MEMS contact failure can be found in literature. It is probably due to the fact that, the contact degradation under hot-switching is a result complicated by multiple contributing factors such as high electrical field, transient current, static current and mechanical wear. Our work focuses on investigation of contact degradation under hot switching conditions in metal contact MEMS switches.

Except stiction failure, contact degradation is always a result of material transfer (wear is also a type of material transfer). Material transfer on metal micro-contacts can be defined as a material re-distribution which occurs either between the contact area and its surroundings or between the two contact surfaces during switch operation. The resulted contact surface damage or material loss from the contact area eventually leads to an un-qualified contact resistance, causing a device failure. One of the major failure mechanisms that have been investigated is arcing in hot switching MEMS switches. Field induced metal phase arc has been proposed based on the dramatic failure features observed in MEMS switches [5, 6]. However, the non-arc test conditions contradict with this material transfer mechanism. And additionally, no arc characteristics were observed by high resolution time traces. Therefore more work needs to be done to understand the micro-/ nano-scale material transfer under the non-arc, but high electrical field MEMS switch operation conditions.

Research of field induced material transfer can be traced back to the development of electric relays and switches in the early 20th century. Most commonly, it relates to an 'electric arc' between the electrical contacts in the devices. In medium- and high- power electrical circuits, contact metal can be vaporized by an arc at high current (thousands of amperes). In addition to the vaporization, the violently produced vapor 'blows' out drops of liquid metal from the contact. Material transfer, in this case, is typically dominated by excessive field-induced current heating, and thus does not have significant directionality. At lower power level, directional arc transfer normally can be observed. The arc process can be divided into two phases, termed metal phase arc and gas phase arc, due to the difference in material transfer mechanism. Contact material typically transfers from anode to cathode in the early stage of a metal phase arc while reverses the direction in a gas phase arc [7,8]. For the case of MEMS switches, only low-power, metal phase arc is possible due to the small device size and micron-scale metal contact separation.

Low-power, directional material transfer has been investigated at low DC electric power level with seperation length (gap between two electrode planes) down to 0.1 um [9]; current down to mA range [10] and voltage down to the ionization energies [11-13]. Much of these macro-contact work shows that there is no detectable directional material transfer when the open circuit voltage is lowered below the ionization voltage (non-inductive circuit) or the current is lowered below certain threshold value. Metal phase arc theory has been developed based on these experiments. According to this theory, the material transfer process in the early stage of contact separation is as following: the contact area is decreased as the contacts separates. Consequently, the constriction resistance, contact voltage and temperature in the constriction area increase rapidly up to boiling point (the contact voltage and boiling temperature of gold are 0.97 V and 3080.15K [29]). Part of the molten bridge material gets evaporated. Across the hot and dense metal vapor, there is a strong electrical field within the small separation gap. It causes field emission of electrons from the cathode. These electrons excite and stepwise ionize the metal atoms (evidences of high excited metal ions have been reported [14-17]). Thereafter these metals are transferred following the field toward the cathode. This arc process is sustained by cathodic electron emission. It is commonly believed that below the ionization voltage, electrons can not have enough energy to ionize the metal ions and below certain threshold current, this process can not be sustained. Up to now, the reported minimum arc voltage and minimum arc current for gold are 12.42 volt and 0.35 A respectively.

Material transfer below the threshold voltage and threshold current first was named "fine transfer" (bridge transfer) by Holm in 1950s. This kind of material transfer was claimed to be caused by asymmetric rupture of the bridge of molten contact material appearing between opening contacts. And the asymmetric rupture was ascribed to the shift of the hottest point from the middle due to DC current heating. However, this theory seems to be contradictory with the experimental facts [14-17, 18, 19] and received rare acceptance.

As discussed above, current knowledge of contact physics barely extends to the MEMS/ NEMS regime because material transfer occurred below ionization voltage or certain critical current hasn't been well addressed and micro-contact hot switching failure has rarely been studied. In order to benefit the arising MEMS industry and the research community, field induced material transfer ought to be investigated in micro-/ nanometer scale at a much lower power level. In our study, field induced material transfer in a MEMS switching-simulator facility was investigated. The growth of transferred material with cycles was characterized by AFM. Electrical contact resistance was *in situ* monitored during switching thus the effect from material transfer on MEMS device performance can be evaluated. Combined effects from current induced melting, mechanical wear in the micro-contacting process were clearly identified using varied test conditions. The authors believe that the outcome of this series of experiments should be beneficial to the design and processing of future MEMS/ NEMS devices as well as the research of basic nano-science.

6.3 Experiment

We have designed a unique setup for monitoring MEMS switching behavior by integrating a MEMS cantilever and separate thin film bottom contact materials into an atomic force microscope (AFM) [20]. The test configuration is shown in Fig. 1. The contact is made between upper pure gold micro-contacts and bottom pure gold contact material. A piezoelectric actuator (Physik Instrumente, P-802.00) is used to vibrate the patterned bottom contacts vertically by an amplitude of 1.8 μm, which is sufficient to bring the upper micro-contacts and bottom contact pads into and out of contact. The contact resistance evolution and the switching motion are both *in-situ* monitored.

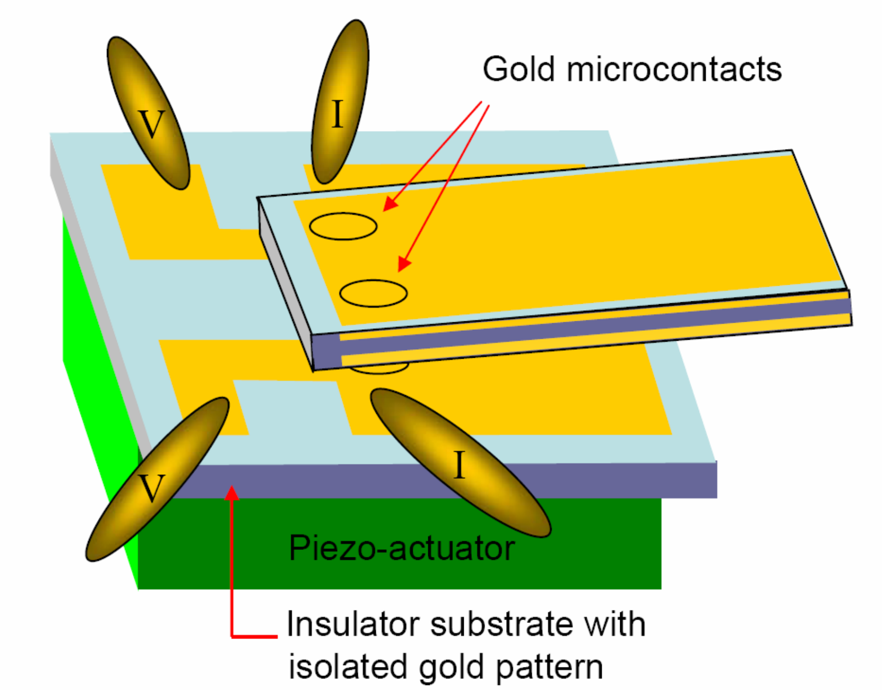

FIG. 1: Configuration for the switching tests.

As is shown in figure 1, the cantilever is composed of three layers: a 2 μm SiO_2 layer with 0.5 μm gold layers on both sides. The width of the cantilever is 75 μm. The effective length of the cantilever can be adjusted while attaching it to the cantilever carrier. For the tests reported here, the effective length was fixed at 150 μm. There are two electrically connected micro-contact bumps on each cantilever (top contacts). The diameter of each contact is 5μm. The bottom contact is patterned gold film (~ 250 nm thick) sputter-deposited on oxidized Si (0 0 1). While the upper micro-contacts make electric contact with the bottom sample contact pad area, the contact resistance is measured by a four-point probe setup. From the figure, the two probes on the right side supply current and the two on the left side sense voltage. The open circuit voltage (V_{oc}) across of the two pairs of micro-contacts can be adjusted from 0 – 6 V using different test system parallel resistors.

In our study, both 'hot switching' and 'cold switching' tests were conducted. Typical test current is limited to ~1 mA. Pure mechanical wear test was also carried without current. The contact force is exerted by the deflected MEMS cantilever, and is calibrated to be ~ 150 μN /micro-contact. After cycling test, both the top micro-contacts and the bottom contact pads were characterized by AFM (Park Scientific, M5). Quantitative volume analysis (using Gwyddion software) was conducted to evaluate the transferred material volume.

6.4 Results and Discussion

Three switching experiments were conducted with V_{oc} = DC 6 V, I = 1mA on three individual sample sets (a sample set is composed of one MEMS cantilever and one bottom contact electrode). During the test, 1 mA current flows through right bottom contact pad, right micro-contact, left micro-contact and right bottom contact pad in sequence while the switch is closed. An electrical field is built in the gap between the upper microcontacts and the bottom contact pads due to the 6 V open circuit voltage while the contacts are broken. The total traveling distance of the micro-contacts with respected to the bottom contact pads is estimated to be less than 100 nm. The switching time is ~1 ms. Transient current was completely suppressed using a 5 KΩ serial resistance. The current spectrum at the moment of contact closure is shown in figure 2. AFM images of the upper micro-contacts and bottom contact pads after 1000 cycles, 2000 cycles and 3600 cycles are shown in Figure 3, figure 4 and figure 5.

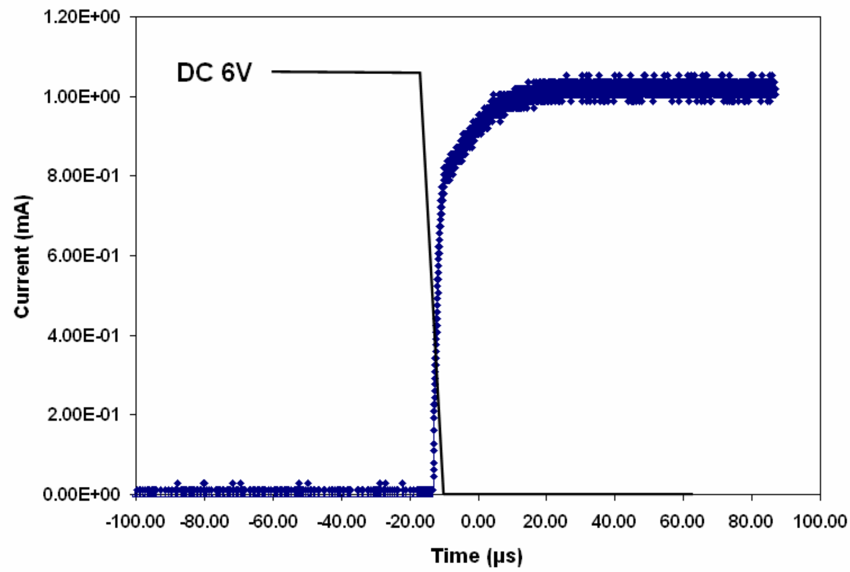

FIG. 2: The current spectrum at the moment of contact closure shows a complete transient suppression

For the contact on the right, the net material transfer is from the bottom contact pad to the upper micro-contacts. And for the contact on the left, the net material transfer is from the upper micro-contact to the bottom contact pad. Thus, a directional transfer of gold following the electrical field/ current can be clearly identified based on this observation. The growth of transferred gold on the right micro-contact also showed different micro-structure evolution. For the 1000 cycles sample set, the built-up is a gathering of many small grains. For the 2000 cycles sample set, transferred gold coalesced to only a couple of large grains. For the 3600 cycles sample set, a cone was formed on the contact surface in the coalescence process.

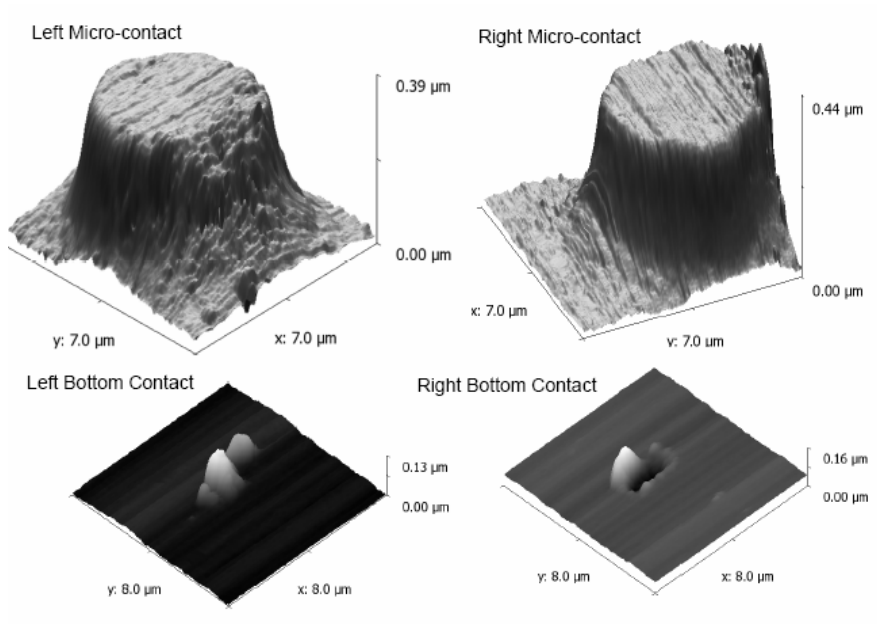

FIG. 3: AFM images of the upper micro-contacts and bottom contact pads after 1000 cycles with DC 6V and 1mA.

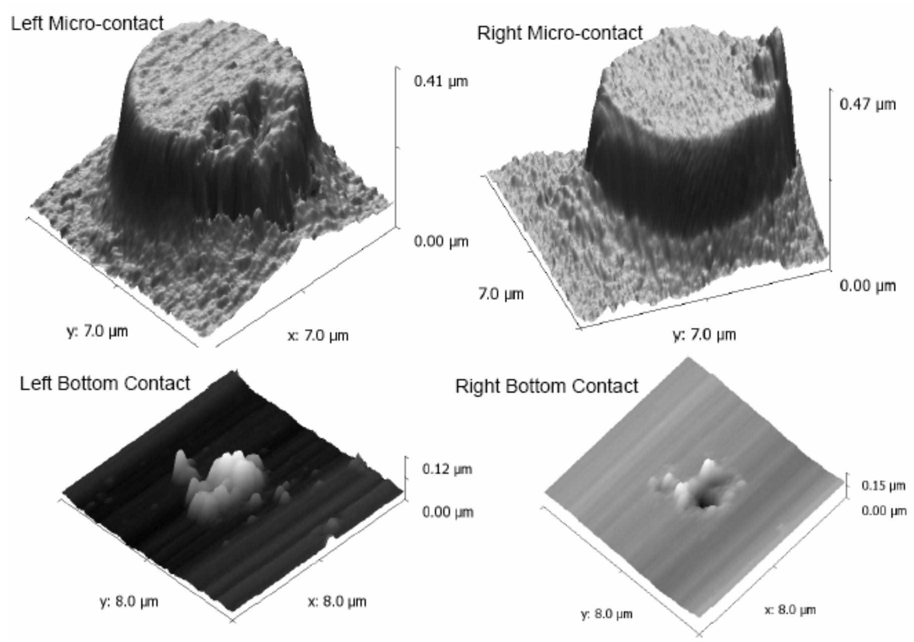

FIG. 4: AFM images of the upper micro-contacts and bottom contact pads after 2000 cycles with DC 6V and 1mA.

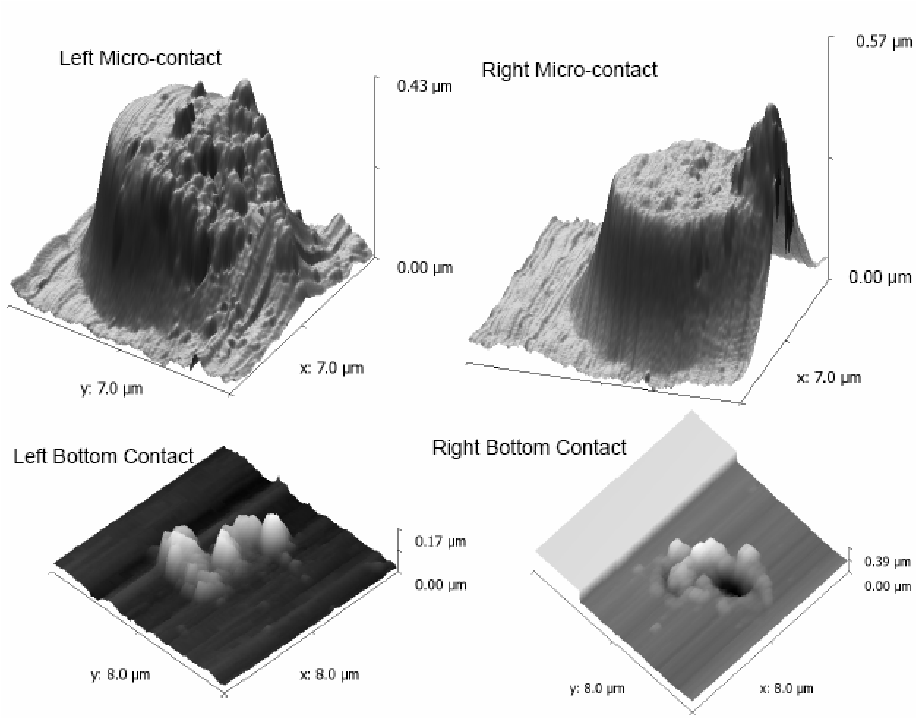

FIG. 5: AFM images of the upper micro-contacts and bottom contact pads after 3600 cycles with DC 6V and 1mA.

The volume gain on the right micro-contacts and on the left bottom contact pad is analyzed using Gwyddion software. The results are shown in figure 6. As we can see in the figure, the material transfer is accelerated with the increase of cycle number (also the increase of involved surface area). The material gain on bottom left pad is always larger than that on the upper right micro-contact (notice that there is material build-up surrounding the hole on the bottom right pad). This phenomenon suggests a superposition of top-down transfer directionality on the field-oriented transfer directionality (more discussion is presented in chapter 7).

The *in-situ* monitored contact resistance evolution for the case of DC 6V, 1mA and 3600 cycles is shown in figure 7. The close-state contact resistance (~0.65 Ω) remains stable despite of a noise associated un-stable contact surface or possible trace amount of contamination. Assuming a constant material transfer rate before 1000 cycles, the average transfer volume/ cycle on the right micro-contact is on the order of 1E-5 μm^3.

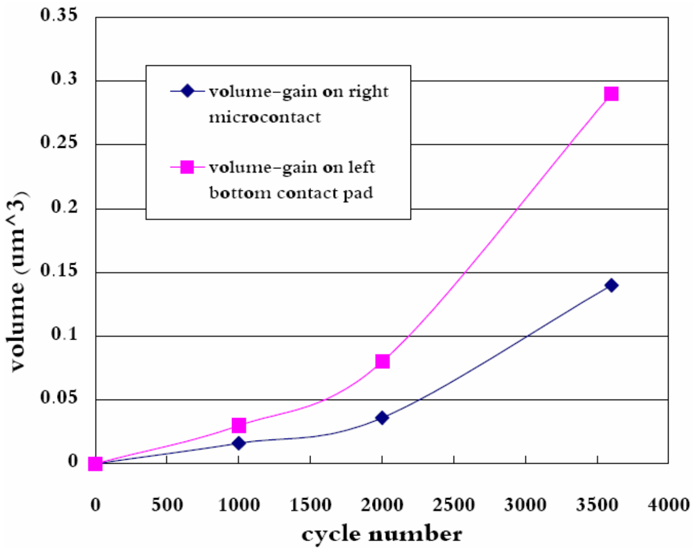

FIG. 6: Volume gain evolution with cycle number

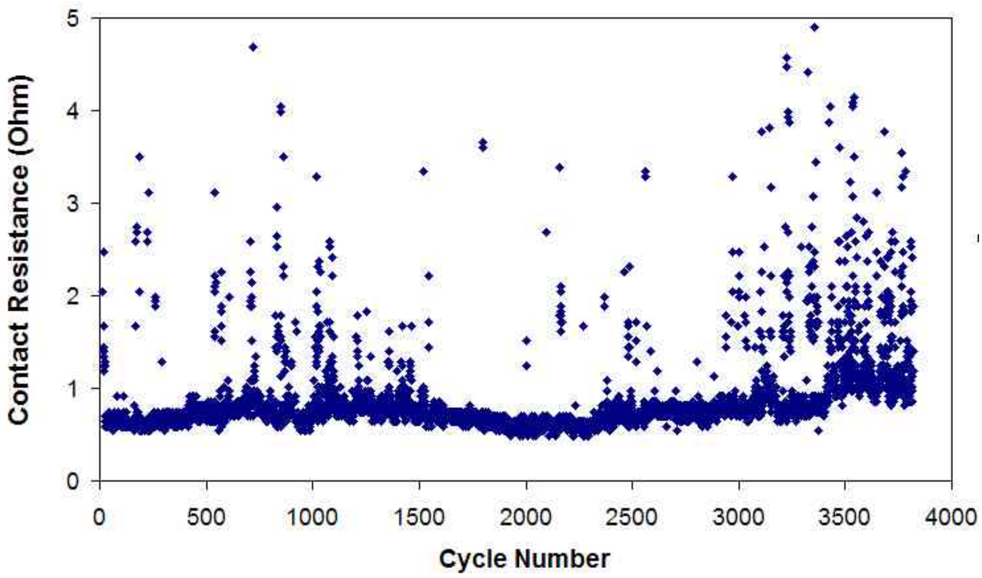

FIG. 7: Contact resistance evolution for the test with open circuit voltage of DC 6V and current limit of 1 mA.

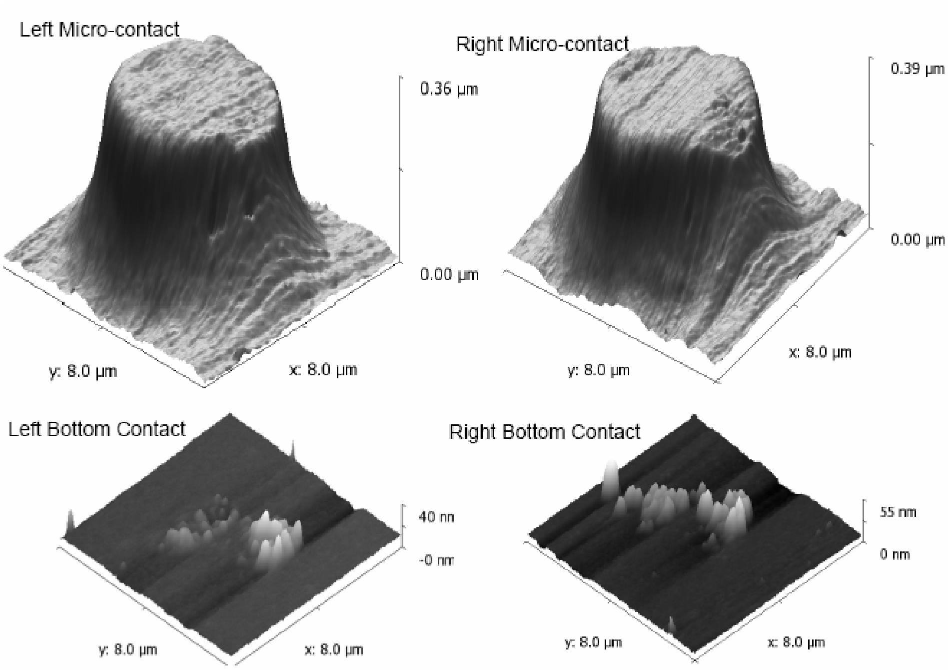

FIG. 8: AFM images of the upper micro-contacts and bottom contact pads after 3600 cycles with AC 6V and 1mA

To confirm the directionality, experiments with reversed DC 6 V were conducted. The results agreed with the previous ones. Furthermore, the experiment with V_{oc} = AC 6V, I = 1mA was conducted. During all the above tests, no arc characteristics (etc. voltage & current overshooting) have ever been detected by the high-resolution transient triggers. The AFM images of the upper micro-contacts and bottom contact pads after 3600 cycles are shown in figure 8. It is clear that the material transfer in this case does not follow the electrical field/ current but from the upper micro-contacts to the bottom electrode pads for both pairs of contacts; the transferred volume is also substantially reduced.

A comparison of the total transferred volume occurred after 3600 cycles under different test conditions is shown in table I. For all the tests, 1mA steady current is supplied except the test for sample set 4, where no current is supplied so that the effect from pure mechanical wear can be evaluated. In the test of sample 2, directional material transfer was canceled in an AC mode and resulted in a much smaller transferred volume. Sample set 3 and 4 yielded similar transferred volume regardless the 1 mA steady current applied in test 3. The transfer directionality in these two cases again is from the upper contacts to the bottom pads.

Table 1: Comparison of Transferred Material with Different V_{oc}

Sample	V_{oc}	Cycle number	Total Transferred Material (μm^3)
1	DC, 6 V	~ 3600	0.430
2	AC, 6 V	~ 3600	0.042
3	DC, 0.02V	~ 3600	0.007
4	DC, 0 V	~ 3600	0.007

Based on the above characterization of the sample sets tested under different test conditions, some characteristics about the material transfer phenomenon could be summarized as following:

1. Volume analysis for the two pairs of contacts suggests a superposition of top-down transfer directionality on the field-oriented transfer directionality, indicating a combinational effect in the process.
2. Field-oriented transfer occurs below the gold ionization voltage (9.42 V) and the minimum arc current (~ 0.35 A)

3. The directional transfer rate increases with number of cycles, indicating that as more surface area involved in the contact, more material can be transferred.
4. Pure mechanical wear, steady current heating is insignificant compared to the field induced material transfer and transient current heating.

As has been discussed in the introduction part, directional material transfer can be induced by arc discharge. Material transfer in metal phase arc does follow the direction of electrical field/ current (from anode to cathode). However, for an arc (even an un-stable, short arc) to able to exist, the voltage across the gap needs to be above the metal ionization energy (for gold, it is 9.42 V) and the minimum arc current should be above 0.35 A. Under our low current (1 mA) and voltage (6 V, DC) condition, not a single un-stable short arc was detected. Therefore, traditional arc theory is not applicable for our case.

Fine transfer theory proposed and developed by Holm *et al.* is intended to explain material transfer occurred below minimum arc voltage [18, 19]. However, this 'current-induced based' model contradicts with previous experimental facts: it predicts a wrong transfer direction for a number of metals such as platinum. In our particular case, this model fails to explain the transfer rate increase as more contact surface is involved. And obviously, electro-migration can't be the mechanism behind the phenomenon due to the opposite material transfer directionality (for electro-migration, material transfer follows the flow of electrons).

Nanometer scale tip-atom-sample interaction (field evaporation) has been investigated for the application of nano-dots patterning. Tsong claimed that when the tip to sample distance is small, the atom-tip and atom sample interactions start to overlap. The sum exhibits a double-well structure having a small activation barrier. The atom can either be transferred from the tip to the sample or from the sample to the tip depending on the electrical field polarity [21]. I.-W. Lyo and P. Avouris experimentally showed that as the tip-sample distance decreases, the effective tunneling barrier is substantially reduced [22].

Referring back to our experiment facts, conditions do favor the field evaporation: the edge of the slightly tilted micro-contacts (slight tilting is common in MEMS actuators while making contact) acts like the tip; the bottom contact pads act like the bottom flat sample; It has been reported that field evaporation of gold could occur within 10 ns with little change in transfer volume (reported by Mamin et al. [23], 5 volts DC pulse is used in his experiment). In our case, the switching time is on the order of milli-second and the maximum switching gap is on the order of ~ 100 nm. It seems that these test conditions do satisfy the requirement for field evaporation. We also have found that the material transfer volume per cycle in our experiment is comparable to those reported for STM /AFM gold nano-dot deposition experiments (diameters of transferred gold nano-dots ranges from 5 nm-100 nm and the height ranges from sub-nanometer to above 10 nm [23-27] in their cases). From the above analysis, we conclude that field evaporation, instead of metallic-arcing should be responsible for the nano-scale, field-oriented material transfer observed in our MEMS switching simulator tests.

Identification of this field-induced contact material transfer phenomenon in a MEMS testing facility renders a clear insight into the failure mechanism of hot-switched MEMS switches. And this could help to improve the MEMS switch hot-switching reliability from the design and device operation perspective. Below are a few suggestions the authors believe to help eliminating field induced contact degradation.

1. To avoid this type of contact degradation, it might be necessary to lower the open circuit voltage to below 3 volts (a widely reported threshold voltage value for field evaporation of gold) so that the field strength during switching may not exceed the critical field for field evaporation.
2. Since field evaporation is a thermally-activated transfer process (transfer rate is exponentially dependent on temperature), it is beneficial to keep device operation at a relatively low temperature. So on-chip heat-sink or cooling method should be able to improve the hot-switching reliability
3. As indicated by our experiments, more involved surface area (in our experiment, the involved surface area grows as the surface area of the cone increases) increases the transfer rate. It is probably due to the increased number of field evaporation sites. Thus, minimizing the involved surface area should also minimize the transfer rate.
4. Materials with higher critical field evaporation field could be the good alternatives to be used as contact materials for hot-switch MEMS devices. The theoretical room-temperature critical field for different materials can be found in Tsong's paper [21].

6.5 Conclusion

In this study, nano-scale, directional gold contact material transfer was observed in a MEMS switch test simulator. Characteristics revealed from the AFM characterization provide clear evidence to identify the field-oriented material transfer as field evaporation. This mechanism identification is essential for avoiding thus material transfer in hot-switched MEMS actuators.

6.6 References

[1] A. S. Morris, S. Cunningham, D. Dereus and G. Schopfer, "High-performance integrated RF-MEMS: Part 1 – the process," *Proceedings of 33rd European Microwave Conference*, 2003, pp. 21-24

[2] S. Majumder *et. al.,* "Study of contacts in an electrostatically actuated microswitch," *Sens. Act. A.,* 93 (1): pp. 19-26, 2001

[3] G. Rebeiz, *RF MEMS Theory, Design, and Technology* (NJ: Wiley), 2003

[4] J. Bouchaud and B. Knoblich, "RF MEMS switches deliver on early promise," *MEMS Investor Journal,* (October, 2007)*,*website at: http://www.memsinvestorjournal.com/2007/10/rf-mems-switche.html#more

[5] E. J. J. Kruglick and K. S. J. Pister, "Lateral MEMS microcontact consideration,", *J. Microelectromechanical Syst.* vol. 8, pp. 264-271, 1999

[6] E.J.J. Kruglick, Ph.D. dissertation, University of California,. Berkeley, 1999

[7] Z.-K. Chen and K. Sawa, "Effect of arc behavior on materials transfer: a review," *IEEE Trans. Comp., Packag., Manufact. Technol. A*, vol. 21, pp. 310–322, 1998.

[8] Z. Chen and G. Witter, "Electrical erosion comparison of materials for automotive loads," in *Proc. 19th ICEC, Addendum (Paper 14)*, p.7, 1998

[9] L. Morin, N. Ben Jemaa, D. Jeannot and H. Sone, "Transition from the anodic arc phase to the cathodic metallic arc phase in vacuum at low DC electrical level," *IEEE Transactions on Components and Packaging Technologies*, vol. 25, no. 4 p. 651, 2002

[10] H. Mizukoshi, K. Sawa, M. Hasegawa, and K. Niizuma, “An experimental study on material transfer and arc erosion characteristic of Ag contacts under switching lower currents,” *IEICE Trans. Electron.* Vo. E77-C, pp. 1655-1661, 1994

[11] I. Dietrich, “Untersuchungen zum kurzen AbreisBbogen an schwach belasteten elektrischen Kontakten,” *Ann. Phys.*, vol. 7, no. 4, pp. 167-177, 1959

[12] L. H. Germer and W. S. Boyle, “Two distinct types of short arcs,” *J. Appl. Phys.,* vol. 27, pp. 32-39, 1956

[13] J. A. Riddlestone, “Short duration discharges between separating contacts in a 6V circuit,” *Bri. J. Appl. Phys.,* vol. 8, pp. 105-108, 1957

[14] F. Lewellyn-Jones and M. C. Cowburn, “Time-resolved spectroscopy ofcontact micro-plasma,” in *Proc. 8th ICECP,* 1976, pp. 263-268

[15] A. Kleinle, “Der Mechanismus de kurzen Lichtogen in elektrischen Kontakten,” Ph.D. Dissertation, Univ. Frankfurt/ Main, Frankfut, Germany, 1963

[16] M. C. Cowburn and F. Lewellyn-Jones, “Spectroscopic investigation of the radiation emitted from contact micro-arcs,” in *Proc. 5th ICECP, 1970,* pp. 281-284.

[17] J. A. Augis and L. L. Hines, “Arc duration in the anodic case,” *IEEE Trans. Parts, Hybrids, Packag.* Vol. PHP-11, pp. 11-14, 1975

[18] R. Holm, Electric Contacts Handbook, Springer-Verlag: Berlin/Gottingen/Heidelberg, 1958, p. 379

[19] W. F. Rieder, “Low current arc modes of short length and time: A Review”, *IEEE Trans. Comp. Packag. Technol.,* vol. 23, no. 2, 2000, pp. 286-292

[20] Z. Yang, D. Lichtenwalner, A. Morris, S. Menzel, C. Nauenheim, A. Gruverman, J. Krim and A. I. Kingon, "A new test facility for efficient evaluation of MEMS contact materials," *J. Micromech. Microeng.*, vol.17, pp. 1788-1795, 2007

[21] T. T. Tsong, "Effects of an electric field in atomic manipulations", *Phys. Rev. B*, vol. 44, pp. 13703-13710, 1991

[22] I.-W. Lyo and P. Avouris, " Field-induced Nanometer to Atomic-Scale Manipulation of Silicon Surfaces with STM", *Science* 253,173 (1991)

[23] H. J. Mamin, P. H. Guethner, D. Rugar, "Atomic emission from a gold scanning tunneling microscope tip," *Phys. Rev. Lett.* 65,2418 (1990).

[24] J. Y. Park and R. J. Phaneuf, "Polarity dependence in pulsed scanning tunneling microscopy fabrication and modification of metal nanodots on silicon," *J. Appl. Phys.*, vol. 92, pp. 2139-2142, 2002

[25] M. E. Pumarol, Y. Miyahara, R. Gagnon and P. Grutter, "Controlled deposition of gold nanodots using non-contact atomic force microscopy," *Nanotechnology,* vol. 16, pp. 1083-1088, 2005

[26] H. Koyanagi, S. Hosaka and R. Imura, " Field evaporation of gold atoms onto a silicon dioxide film by using an atomic force microscope," *Appl. Phys. Lett.*, vol. 67, pp.2609-2611, 1995

[27] W. F. Rieder, "Low current arc modes of short length and time: a review," *IEEE Trans. Comp. Packg. Techno*., vol. 23, p. 286, 2000

[28] N. M. Miskovsky and T. T. Tsong, "Field evaporation of gold in single-electrode and double electrode system," *Phys. Rev. B,* 46 (4): pp. 2640-2643, 1992

[29] P. G. Slade, *Electrical contacts: principles and applications,* New York: Marcel and Dekka, 1st edition, 1999

CHAPTER 7 Resolving Transfer Directionality for Field Evaporation of Gold

(This chapter is to be submitted to Applied Physics Letters)

7.1 Abstract

Identification of transfer direction for field evaporation of gold is important to the development of high-reliable nano-scale surface modification techniques. Previous gold nano-dots transfer works using scanning tunneling microscope (STM) or atomic force microscope (AFM) raised a large controversial debate on this subject. This work resolves the transfer directionality for gold field evaporation by successfully excluding the effects from topographic and geometric differences between the 'tip' and 'sample'. It was found that gold nano-dots transferred in the direction of electrical field indicating only positive ions are created in the transfer process. Contact-transfer was also characterized. Possibility of metal phase arc is excluded after a careful examination.

7.2 Text Body

Since early 90s, nano-scale field-induced material transfer has become an active research field due to its potential applications in high-density memories and quantum devices [1-4]. High-reliable gold nano-dot deposition using STM /AFM has been demonstrated by different research groups [3-8]. However, it is surprised that the transfer direction varies in these reports. Mamin reported reliable mound-formation on gold substrate when single negative voltage pulses were applied to the gold STM tip [5]. In contrast, he also pointed out that gold atoms were removed from the substrate step-wisely when multiple negative pulses were applied to the gold tip over one location [6]. And the direction of gold field evaporation was thought to be opposite to the electric filed based on his single-pulse results. Topographic effect was suspected to be responsible for the directionality mismatach in his multiple-pulse experiments. Later, more conflicts rose from Chang's observation that gold nano-dots transferred either following the electric field or in the opposite direction when single negative pulses were applied to the gold tip. The probability of these two types of transfer is nearly equal. It seemed that, in thise case, both positive and negative ions were created [9]. In a dissimilar Pt-Ir tip/Au substrate system, Bessho *et al.* found that gold atoms be removed from the substrate by applying single positive pulses to the gold substrate. [3]. This observation supports the suggestion that only positive ions were created during the field-induced transfer process.

It has been showed that physical contact between the 'tip' and 'sample' would occur during the nano-dot transfer process in a STM [10, 11]. Therefore, the transfer process could be a combined effect of field induced transfer, thermal-migration and contact-transfer. In normal STM /AFM experiments, it is difficult to individually evaluate these effects due to the topographic and geometric differences between the tip and sample [6, 12]. As a result, nano-scale field-induced material transfer has not been well understood even with more than two decades of research.

In our tests, double pairs of identical micro-contacts were used in our study to investigate field-induced material transfer. A conductive micro-cantilever with two identical gold micro-contacts served as the 'tip'. Each micro-contact has a radius of ~ 2.5 µm and height of ~ 350nm. Two electrically-isolated identical gold thin film contact pads (thickness of 250 nm) served as the 'sample'. Both the 'tip' and 'sample' were incorporated into an AFM (Park Scientific, M5). To assess the effect of physical contact, upper cantilever is cycled upon the bottom contacts with a relative z-direction magnitude of ~ 100 nm by a pize-actuator (PI-

802.00). The switching time is ~1 ms. A large number of cycles allow accumulated transfer volume to be quantitatively measured by AFM and its data processing software (Gwyddion). The contact force is calibrated to be ~ 150 μN/ contact. A maximum total open circuit voltage of 6 V (well below the minimum arc voltage of gold at 12.42 V [13]) is applied across the two contact pairs through a non-inductive circuit. A steady current of 1 mA (well below the minimum arc current of gold at 350 mA [13]) is feed through them in sequence. Therefore, two identical pairs of micro-contacts should undergo exactly the same test conditions except the opposite electrical field direction. Differences between the material transfer features for the two contact pair then should be due to the field directionality. Electric arc is intentionally avoided by the test condition-setting. Voltage across the two contact pairs and circuit current were *in-situ* monitored during the test.

Figure 1 shows the AFM images of the upper gold micro-contacts and bottom gold contact pads after 2000 cycles with DC 6V and 1 mA. During the test, 1 mA current flows through right bottom contact pad, right micro-contact, left micro-contact and right bottom contact pad in sequence when the switch is closed. Electrical field is developed between the upper micro-contacts and the bottom contact pads when the contacts break.

For the contact on the right, gold atoms transfer from the bottom contact pad to the upper micro-contacts. And for the contact on the left, gold atoms transfer from the upper micro-contact to the bottom contact pad. Thus, a transfer directionality following the electrical field/ current can be clearly identified. This test was repeated on new sample-sets using a negative DC voltage source (maximum open circuit voltage = - 6 V). The transfer direction still follows the electric field. Therefore, negative gold ions created should not have been created during the transfer process. During all the above tests, no arc characteristics (etc. voltage & current overshooting) have ever been detected by the high-resolution transient triggers.

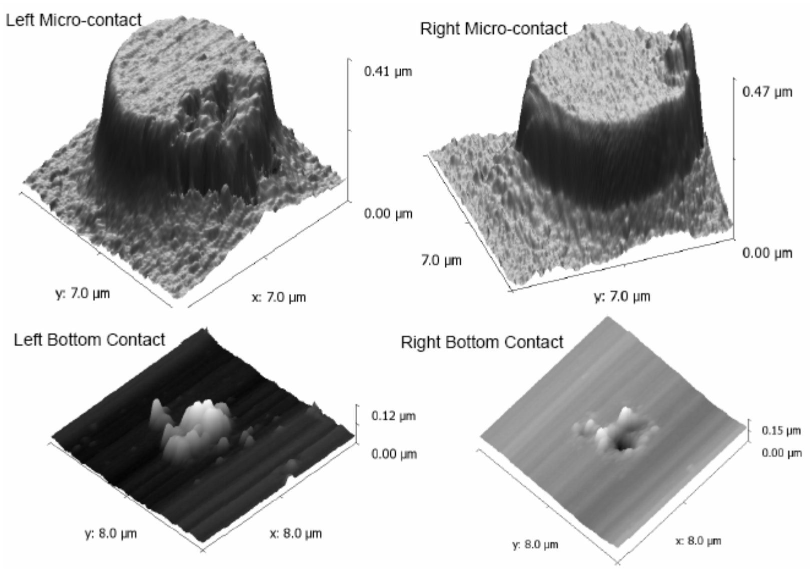

FIG. 1: AFM images of the upper micro-contacts and bottom contact pads after 2000 cycles with DC 6V and 1mA

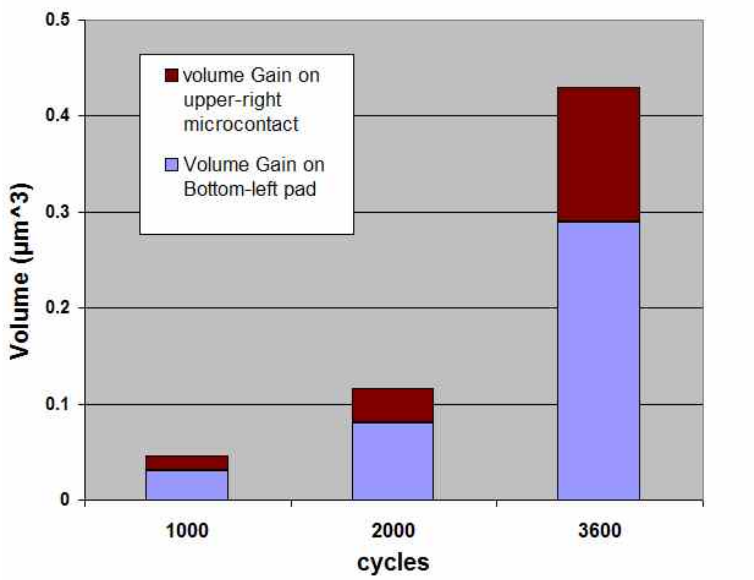

FIG. 2: Volume gain evolution with cycle number

The chart of transfer volume vs. number of cycles is shown in figure 2. The volume-gain on the up-right micro-contact is larger than the volume-gain on the left bottom contact pad. There is always some material build-up around the hole on right bottom contact pads. These results suggest a super-position of a top-to-bottom transfer on the electric-field-oriented transfer. Assuming a linear transfer rate before 1,000 cycles, the average transferred volume/ cycle is similar to those from the previous gold field evaporation experiments using AFM [4, 8].

Results of using an AC voltage source is shown in figure 3. The material transfer in this case did not follow the electrical field/ current. Only the top-to-bottom transfer was observed for both contact pairs. The total transferred volume was also greatly reduced because the transient energy of the strong electric field was used to transfer gold atoms back and forth without causing much net-transfer volume. With a cold cycling test (open circuit voltage equals zero; steady current equals zero), still only the top-to-bottom transfer was observed for both contact pair. But the total transfer volume was further significantly reduced without transient heating. These results suggest that the top-to-bottom transfer is due to contact-transfer during cycling with its direction determined by the topographic and geometric differences or material differences between the two contact surfaces

Traditional single tip-sample configuration tests were also performed in an AFM (CPR) to assist our material transfer evaluation. A silicon substrate with 20 nm of gold deposited on the top was used as substrate. Pt-Ti coated and Au coated AFM tips ($k = 0.15$ N/m) were lift up from the contact point under a bias of +/- 6V.

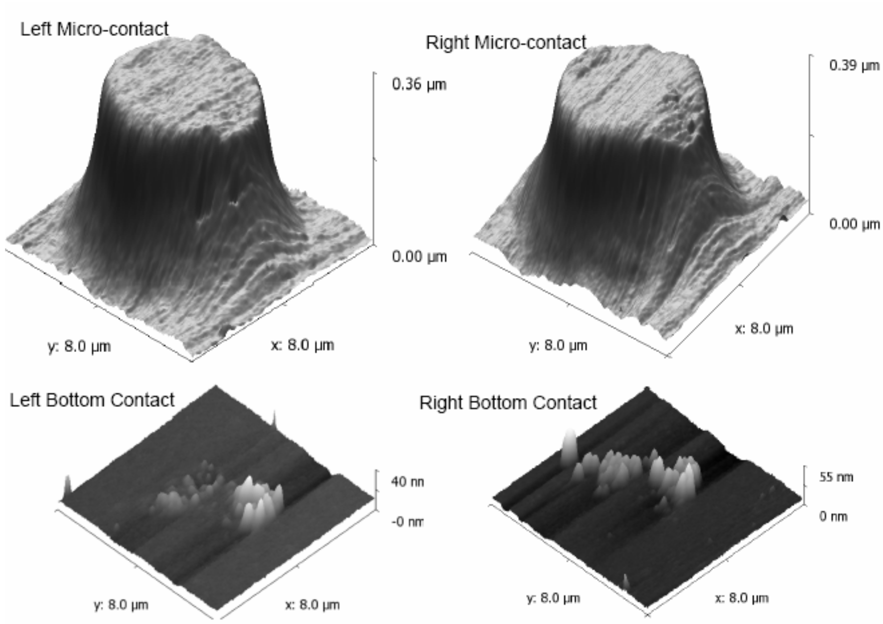

FIG. 3: AFM images of the upper micro-contacts and bottom contact pads after 3600 cycles with AC 6V and 1mA

The force was set to the order of a few nano-Newton to avoid mechanical wear and the current was set to nearly tunneling current range (~ 100 nA) by a serial resistance of 50 MΩ. Thus both the contact force and current were lowered 10,000 times compared to our double-contact cantilever test. Material transfer on the substrate was imaged by the AFM immediately after each lift-up.

In the case of Pt-Ti tip/ Au substrate, the electric-field-oriented transfer was observed. The AFM characterization is shown in figure 4. The transferred volume is close to that of the double-micro-contact DC tests (per cycle) although both the current limit and contact force is lowered by 10,000 times. Therefore, neither the current nor the force should cause this transfer. In the case of gold tip/ Au substrate, most initial lift-ups (with 6V bias) generated mound-like features on the substrates. Hole-mound combined structures were also occasionally observed. Similar previous observations were reported [5, 9]. However, according to our confirmed directionality of gold field evaporation, we believe the mound-like features should be formed by pulling material from the substrate instead of transferring material from the tip. The pulled material was not successfully transferred to the tip because of a simultaneous contact transfer process which prefers the bottom substrate in this particular Au tip/ Au substrate system. This agrees with Mamin's data of multiple pulses [6]. And similar step-wise field induced nano-transfer was also reported for silicon [14].

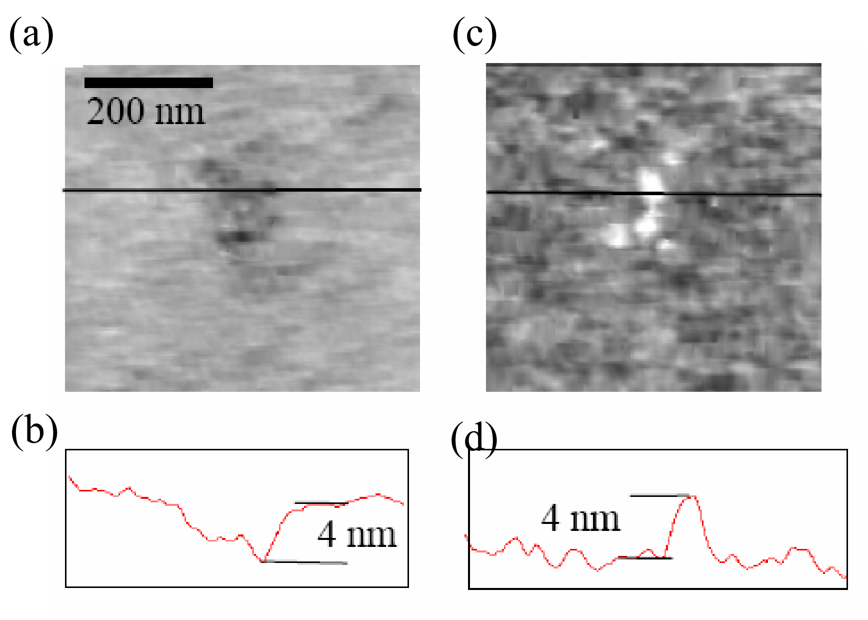

FIG. 4: Pt-Ti tip /Au substrate system: (a) AFM image of the contact area after the tip retracted with bias of -6 V; (b) a height profile along the line in (a); (c) AFM image of the contact area after the tip retracted with bias of +6 V retracted; (d) a height profile along the line in (c).

Modeling of field evaporation for nano- and atomic scale surface modification is based on the classic field evaporation theory [15, 16]. The atom transfer rate can be expressed by the following equation:

$$\kappa = \nu \cdot \exp(-\frac{Q_0}{kT}) \tag{1}$$

where, k is the transfer rate, v is the atom vibration frequency (~10^{13} s^{-1}), Q_0 is the ionization energy barrier. Tsong calculated a threshold field of 3.23 V/Å for Au^+ at room temperature [17], which does not agree with the experimental values of 0.4-0.6 V/Å [5, 9].

However, it is important to notice that high-temperature has to be involved in the contact transfer process. A contact voltage of 0.43 V can be obtained before contact-break in Pascual's nano-transfer experiments [11]. This corresponds to the melting-temperature of gold. Therefore transfer threshold field is expected to be greatly reduced at the elevated temperature. Advanced high-temperature field evaporation simulation is in needed for improved modeling of gold field evaporation in STM /AFM configurations.

In summary, we have resolved the transfer directionality for field evaporation of gold in STM/ AFM configurations. Only positive gold ions are created in the transfer process. The characteristics of the simultaneous contact transfer are determined by the differences between the 'tip' and 'sample'. Further research on material-dependent contact transfer and transient-temperature distribution may help to develop reversible transfer process with high reliability.

7.3 References

[1] J. A. Stroscio and D. M. Eigler, "Atomic and molecular manipulation with the scanning tunneling microscope," *Science* 254, pp. 1319-1326 1991

[2] P. Ball and L. Garwin, "Science at atomic scale," *Nature* 355 (27), pp. 761-766, 1992

[3] K. Bessho and S. Hashimoto, "Fabricating nanoscale structures on Au surface with scanning tunneling microscope," *Appl. Phys. Lett.* 65, p. 2142, 1994

[4] H. Koyanagi, S. Hosaka and R. Imura, "Field evaporation of gold atoms onto a silicon dioxide film by using an atomic force microscope," *Appl. Phys. Lett.*, 67, pp.2609-2611, 1995

[5] H. J. Mamin, P. H. Guethner, D. Rugar, "Atomic emission from a gold scanning tunneling microscope tip," *Phys. Rev. Lett.* 65, p. 2418, 1990

[6] H. J. Mamin, S. Chiang, H. Birk, P. H. Guethner and D. Rugar, "Gold deposition from a scanning tunneling microscope tip," *J. Vac. Sci. Tech. B,* 9 pp. 1398-1402, 1991

[7] J. Y. Park and R. J. Phaneu, "Polarity dependence in pulsed scanning tunneling microscopy fabrication and modification of metal nanodots on silicon," *J. Appl. Phys.* 92, pp. 2139-2143, 2002

[8] M. E. Pumarol, Y. Miyahara and R. Gagnon, "Controlled deposition of gold nanodots using non-contact atomic force microscopy," *Nanotechnology* 16, pp. 1083-1088, 2005

[9] C. S. Chang, W. B. Su and T. T. Tsong, "Field evaporation between a gold tip and a gold surface in the scanning tunneling microscope configuration," *Phys. Rev. Lett.* 72, pp. 574-577, 1994

[10] K. J. Strozewski, S. E. McBride and G. C. Wetsel, “Correlation of photon emission with electric-field-initiated nanometer-scale surface modification,” *J. Appl. Phys.* 79 (11), p. 8638, 1996

[11] J. I. Pascual *et al.*, “Quantum contact in gold nanostructures by scanning tunneling-microscopy,” *Phys. Rev. Lett.* 71 (12): p. 1852, 1993

[12] J. Y. Park and R. J. Phaneuf, “Polarity dependence in pulsed scanning tunneling microscopy fabrication and modification of metal nanodots on silicon,” J. Appl. Phys. 92 (4): p. 2139, 2002

[13] P. G. Slade, *Electrical contacts: principles and applications,* New York: Marcel and Dekka, 1st edition, 1999

[14] I.-W. Lyo and P. Avouris, “ Field-induced Nanometer to Atomic-Scale Manipulation of Silicon Surfaces with STM”, ***Science* 253,** p. 173 1991.

[15] E. W. Muller, “Field ion microscopy,” *Science,* 149 (3684): pp. 591-601, 1965

[16] D. Blavette, A. Bostel, J. M. Sarrau, B. Deconihout and A. Menand, “An atom probe for three-dimensional tomography,” *Nature* 363, pp. 432-435, 1993

[17] T. T. Tsong, “Effects of an electric field in atomic manipulations”, *Phys. Rev. B* 44, pp. 13703-13710, 1991

CHAPTER 8

Brief Summary of Failure Modes for Gold-contact MEMS Switching Tests

In this chapter, failure modes of our gold-contact MEMS switching tests are briefly summarized based on varied operational conditions. These test conditions include high-field hot switching (with an open-circuit voltage of AC or DC 6 volts), low-field hot switching (with an open-circuit voltage of DC 1 volt and DC 0.02 volt), cold switching with a steady test current of 1 mA, cold switching without current. In these tests, the steady current were all kept at 1 mA expect the one test condition of cold switching without current. The contact force was calibrated to be ~ 150 μN /micro-contacts (300 μN in total). Additionally, switching test and characterization data from a cold-switched MEMS switch is included so that the case of low contact force (~ 50 μN /micro-contact, 100 μN in total), low test current (100 μA) can be reviewed.

Finally, contribution of this work is summarized and opportunities of future research are discussed.

8.1 High-field hot switching tests (DC and AC)

The failure characterization and analysis of high-field hot-switching are presented in detailed in Chapter 6. Field-induced material transfer seems to be the dominant in determining the degradation rate (material transfer rate). The material transfer is clearly not an electric arc process. Instead, our experimental results provide evidence that the material transfer in this case could be induced by field evaporation at elevated temperature. It has shown that negative gold ions should not be presented in the transfer process. Therefore, the transfer directionality for gold field evaporation is also confirmed. When applying to real MEMS switch design, it should be noted that, effect of field induced material transfer could be magnified in our particular test configuration due to the small relative actuation range (~ 100 nm) and relatively large switching time (~ ms). Also, our single field evaporation experiments on Au tip/ Au substrate and Pt-Ti tip/ Au substrate systems verified that voltage is the determinant factor instead of current and force in this type of contact degradation.

8.2 Low-field hot-switching tests

Figure 1 shows the contact degradations after 3,600 low-field hot-switching cycles with a total open circuit voltage of 1 V and a steady current of 1 mA. A big un-balanced material transfer between the two pairs of micro-contacts was observed. Repeated tests resulted in the same results. It could be due to the slightly un-balanced alignment. However, the same test facility still worked fine for high-field switching tests and cold switching tests. It might be explained in this way: in the switching test, one pair of micro-contacts is always opened slight ahead of the other because of the non-perfect cantilever alignment. For high-field hot-switching, the two electrical fields between the two slightly-different contact gaps are always nearly equal according to the basic capacitance theory. And these two electrical fields are both strong enough to induce field evaporation of gold atoms. For cold switching, only the mechanical wear and steady-current heating are responsible for the contact-degradation, thus the scenario that one contact opens slightly earlier would not make a difference on the degradation features. The case of low-field hot switching tests is different in the sense that the electric field is not strong enough to induce field evaporation. And energy has to be dissipated by transient heating. Transient current only occurs for the first-open contact because there is no significant potential difference between the two separating parts when the second contact pair opens. As a result, for low-field switching, no electric-field-oriented material transfer can be observed and the energy dissipation occurs only on one contact pair. The energy is dissipated in the form of thermal wear which may involve material softening, melting, even boiling.

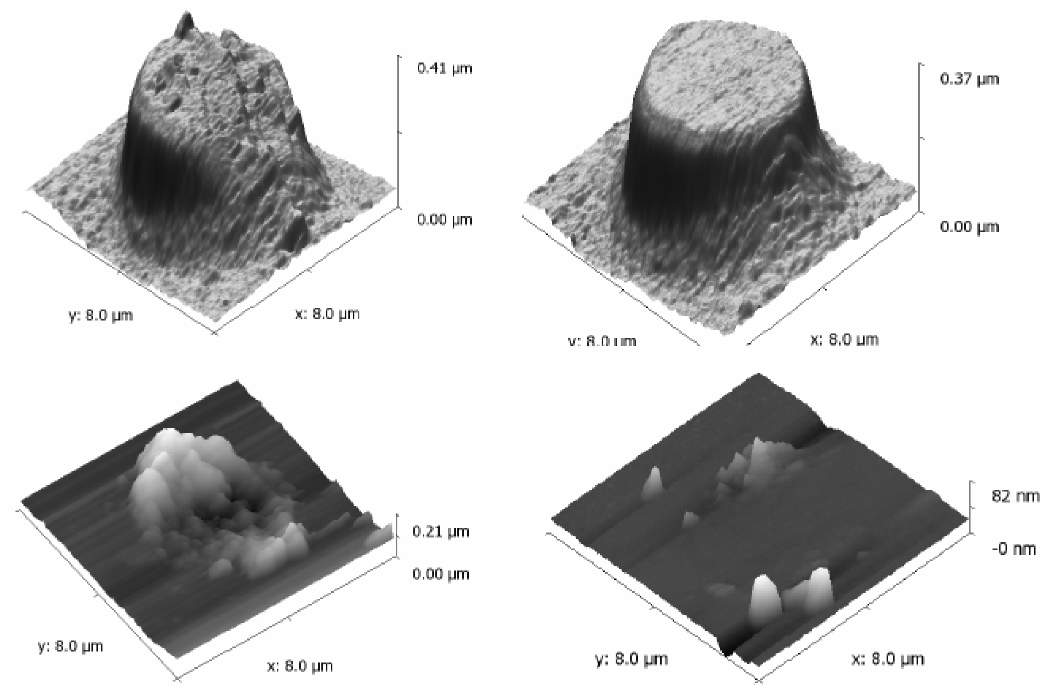

FIG. 1: AFM images of the upper micro-contacts and bottom contact pads after 3600 cycles with DC 1 V and 1mA

8.3 Cold Switching Tests

Figure 2 shows the contact degradations after ~ 50,000 cold-switching cycles with a total open a steady current of 1 mA. Mechanical wear can be identified on both micro-contacts. Gold contact material was worn off from the upper contacts to the bottom pads. The total-transferred-volume is only ~ 0.066 μm^3. The transfer rate is estimated to be nearly two orders of magnitude less than that of high-field DC-6 volt hot switching (~ 0.43 μm^3 after 3,600 cycles).

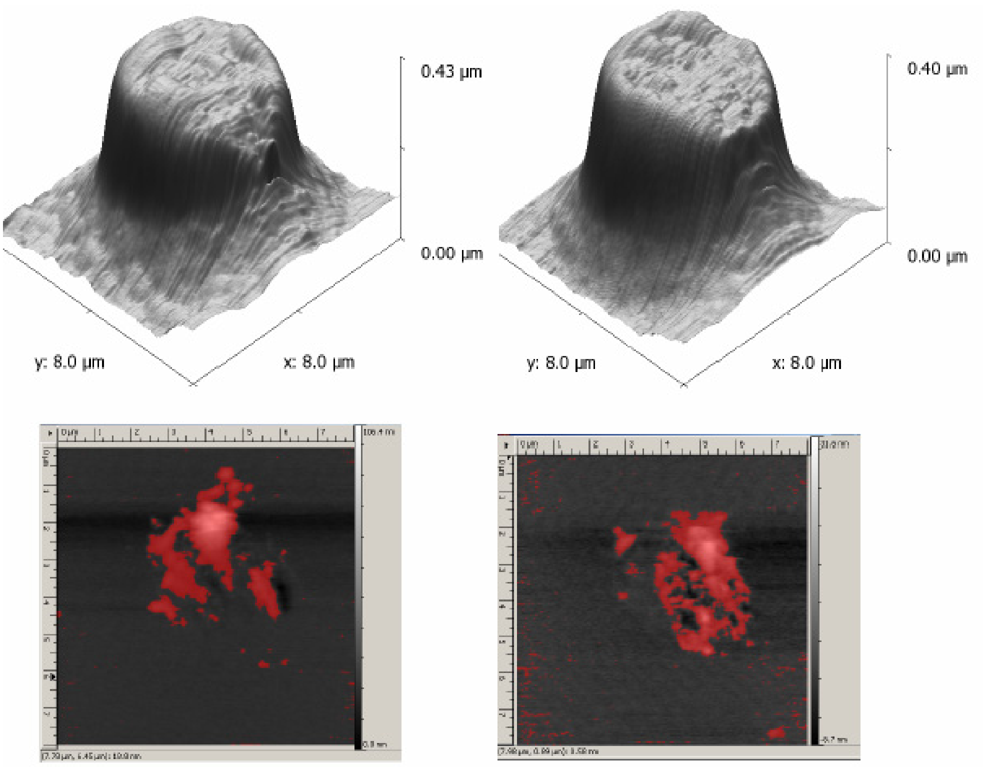

FIG. 2: AFM images of the upper micro-contacts and bottom contact pads after 3600 cold switching cycles with 1mA. The material build-up on the bottom contact is labeled red for quantitative transfer-volume measurement using Gwyddion software.

The whole spectrum of contact resistance evolution is shown in figure 3. Contact resistance became un-stable due to roughened surface after only ~ 7,000 cycles. When contact wear was accumulated to a certain point, the electrical detection mechanism (discussed in chapter 6) was triggered and contact resistance shot up to the open-circuit value. The zoomed-in spectrum of first 8,000 cycles is shown in figure 4. It took ~ 500 initial cycles to achieve a low, stable contact resistance. Similar phenomenon was observed in the tests of wiSpry's switches [1]. For these low-force MEMS switches (~ 50 μN/ micro-contact), more than 1,000 cycles is required to achieve the stable contact resistance.

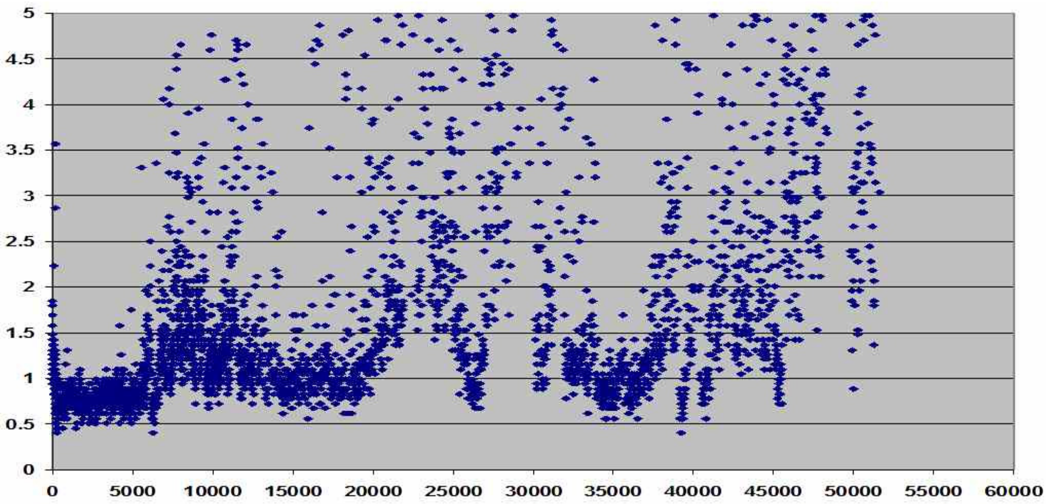

FIG. 3: Contact resistance revolution of cold switching with steady current of 1 mA.

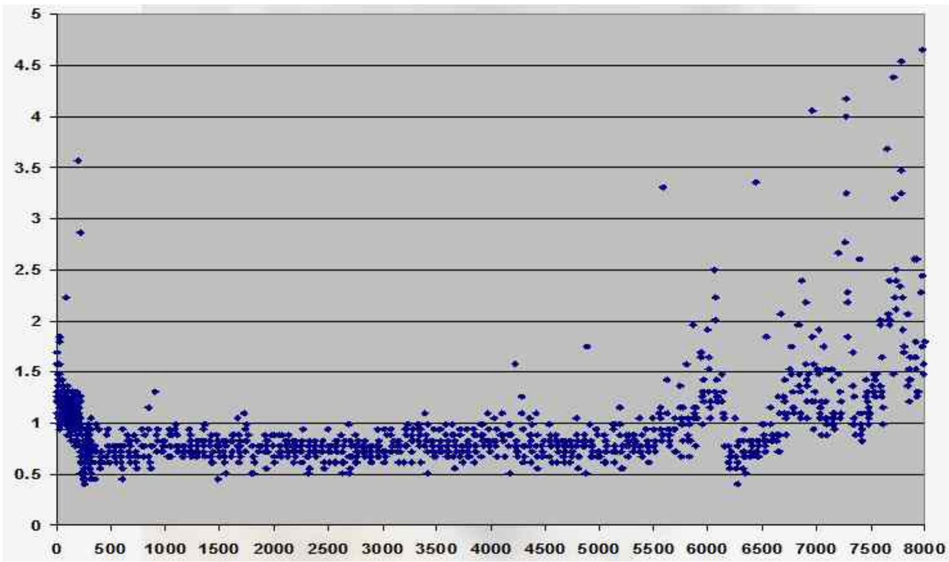

FIG. 4: Zoomed-in spectrum of contact resistance revolution of cold switching with steady current of 1 mA (first 8,000 cycles).

The initial 'burn-in' period could be related to penetration of adsorbed film and asperity deformation. Tests were also run with no steady current. In these tests, very similar wear features and transfer volumes were obtained. Some of the quantitative analysis of transfer volumes is shown in Table I.

Table 1: Total transfer volume under different test conditions

Sample	V_{oc}	Cycle number	Total Transferred Material (μm^3)
1	DC, 6 V	~ 3600	0.430
2	AC, 6 V	~ 3600	0.042
3	DC, 0.02V	~ 3600	0.007
4	DC, 0 V	~ 3600	0.007

From this table, we can see field induced material transfer yields the largest transfer volume. By running the test in AC mode, this directional material transfer is canceled and the resulted total transfer volume is substantially reduced. Thermal wear of a steady current of 1 mA and mechanical wear are insignificant in the cold switching tests.

8.4 Operation of Low Contact Force MEMS Switches in Air

Low contact force MEMS switches from wiSpry Inc. have been tested in air to investigate its performance degradation mechanisms. These switches are actuated using an electro-static force. The actual contact force is calibrated to be ~ 50 μN/ micro-contact. Cold switching tests were run with the steady current being set at 0.1 mA [2]. After the tests, no physical micro-contact damages were detected by AFM for both micro-contacts. Figure 5 shows a switch's contact resistance evolution of 1,700,000 cycles. The contact resistance increase could be due to the increase of absorbed films from ambient air. Accumulation of these films slowly reduced the real metal-metal contact area [3]. And mechanical impact of the micro-contacts occasionally breaks the films causing a sudden, small drop of resistance. When adsorbed films eventually covered the whole contact area, contact resistance shot up rapidly to the Kilo-Ohm range. Therefore, surface contamination issue should be taken into consideration when low-force, low-current cold switching operation is conducted in ambient air.

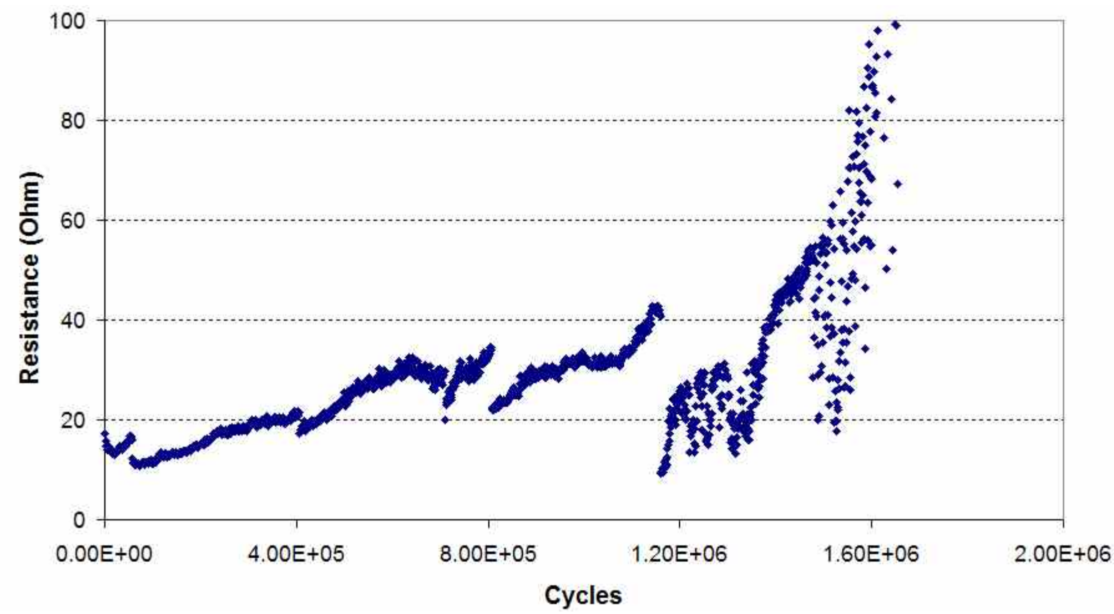

FIG. 5: Contact resistance evolution of a cold switching wiSpry MEMS switch.

8.5 Contributions of This Work

The contributions of this work can be summarized as following:

1. Designed and constructed the micro-contacting test facility that closely mimic the typical MEMS operation and utilized this facility to efficiently evaluate different candidate contact materials for MEMS switches.
2. Systematically studied the Au-Ni material system as contact materials for MEMS switches
3. Evaluated the effects from different film micro-structures (solid solution structure vs. second-phase precipitation structure) on contact degradation performance.
4. Investigated surface topology effect of the films on device contact resistance
5. Utilized rapid thermal annealing (RTA) to fabricate nano-scale graded Au-Ni films and demonstrated its potential use as the contact material in MEMS switches
6. Comprehensively investigated the failure mechanisms for different MEMS operation conditions. Quantitatively analyzed each failure modes.
7. Proposed a new failure mechanism for hot-switched MEMS switches
8. Firstly resolved the directionality of gold field evaporation and suggested the transfer mechanisms.

8.6 Publications from This Work

1. Z Yang, D Lichtenwalner, A Morris, S Menzel, C Nauenheim, A Gruverman, J Krim and A I Kingon, "A new test facility for efficient evaluation of MEMS contact materials," *J. Micro. Mech. Eng.* 17 No 9 (September 2007) 1788-1795

2. Z Yang, D Lichtenwalner, A Morris, J Krim and A I Kingon, "Optimization of Au-Ni alloys as contact materials for MEMS switches." Under review at *IEEE Journal of Microelectromechanical Systems, 2007*
3. Z Yang, D Lichtenwalner and A I Kingon, "Field-Induced Nano-scale Material Transfer between Microcontacts in MEMS Devices," to be submitted to *J. Micro. Mech. Eng.*
4. Z Yang, D Lichtenwalner and A I Kingon, "Resolving transfer directionality for field evaporation of gold," to be submitted to *APL*.

8.7 Future Work

Based on our current results on contact material optimization of Au-Ni binary alloy system and contact physics investigation for metal-contact MEMS switches, more practical work can be done from the material side to achieve better-performed devices. The following ideas for future research are provided.

1. Other binary systems, or even ternary alloy systems can be explored in similar way as Au-Ni alloy system. For example, the phase-diagram of gold-platinum has a similar structure as Au-Ni [4]. Adding platinum could enhance the material toughness without sacrificing the corrosion-resistance. Coutu *et. al* demonstrated that Au-Pt-Cu alloy demonstrated the exceptionally-low contact resistance with a extended switch lifetime showing ternary system might be a interesting research field as well [5]. Au-Ir system might also be interesting because IrO_2 [6] is a conductive metal oxide.
2. Currently we have demonstrated DC-6V open-circuit voltage combined with our particular switching conditions is enough to generate field evaporation of gold atoms

while applying DC-1V only yields thermal wear. However, no detailed threshold field has been obtained. Current theory of gold field evaporation in STM is deficient because only room temperature condition is considered [7]. In order to achieve a proper simulation, transient temperature evolution and distribution during contact-open and close needs to be obtained. It would be reasonable to state that the threshold field should be material-dependent. Therefore, contact materials with high threshold voltage need to be implemented for the high-field hot-switching applications.

3. There is still a range of test conditions hasn't been applied in our previous tests. For example, cold-switching has not been applied to alloy systems. Force-dependent investigation has not bee carried. With small modifications of the test facility or material processing procedures, these tests could be realized in a short time frame. Widening the spectrum of test conditions should enable us to better understand the failure mechanisms of the devices.

8.8 References

[1] Z Yang, D Lichtenwalner, A Morris, S Menzel, C Nauenheim, A Gruverman, J Krim and A I Kingon, "A new test facility for efficient evaluation of MEMS contact materials," *J. Micro. Mech. Eng.* 17 No 9 (September 2007) 1788-1795

[2] C. Brown, *Un-pulished Thesis Work,* at North Carolina State University

[3] B. D. Jensen, L, L.-W. Chow, K. Huang, K. Saitou, J. L. Volakis and K. Kurabayashi, "Effect of nanoscale heating on electrical transport in RF MEMS switch contacts," *J. Microelectromechanical System,* vol 14, n. 5, pp.435-946, 2005.

[4] H. Okamoto and T. B. Massalski, *Phase diagrams of binary gold alloys,* Ohio: ASM international, p. 196, 1987

[5] R. A Coutu, J.R. Reid, R.Cortez, R. E. Strawser and P. E. Kladitis, "Microswitches with sputtered Au, AuPd, Au-on-AuPt, and AuPtCu alloy electric contacts," *IEEE Trans. Comp. Packag. Tech.,* vol. 29, pp. 341-349, 2006

[6] S. H. Brewer, D. W. Wicaksana, J. P. Maria, A. I. Kingon and S. Franzen, "Investigation of the electrical and optical properties of iridium oxide by reflectance FTIR spectroscopy and density function theory calculations," Chemical Physics 313, p. 25, 2005

[7] T. T. Tsong, "Effects of an electric field in atomic manipulations", *Phys. Rev. B* 44, pp. 13703-13710, 1991